

University of Tennessee, Knoxville
Trace: Tennessee Research and Creative Exchange

Doctoral Dissertations | Graduate School

12-2013

Shape Optimization of Turbomachinery Blades Using an Adjoint Harmonic Balance Method

Huang Huang
hhuang9@utk.edu

This Dissertation is brought to you for free and open access by the Graduate School at Trace: Tennessee Research and Creative Exchange. It has been accepted for inclusion in Doctoral Dissertations by an authorized administrator of Trace: Tennessee Research and Creative Exchange. For more information, please contact trace@utk.edu.

To the Graduate Council:

I am submitting herewith a dissertation written by Huang Huang entitled "Shape Optimization of Turbomachinery Blades Using an Adjoint Harmonic Balance Method." I have examined the final electronic copy of this dissertation for form and content and recommend that it be accepted in partial fulfillment of the requirements for the degree of Doctor of Philosophy, with a major in Aerospace Engineering.

Kivanc Ekici, Major Professor

We have read this dissertation and recommend its acceptance:

Rao V. Armilli, Jay I. Frankel, Vasilios Alexiades

Accepted for the Council:
Carolyn R. Hodges

Vice Provost and Dean of the Graduate School

(Original signatures are on file with official student records.)

Shape Optimization of Turbomachinery Blades Using an Adjoint Harmonic Balance Method

A Dissertation

Presented for the

Doctor of Philosophy

Degree

The University of Tennessee, Knoxville

Huang Huang

December 2013

© by Huang Huang, 2013

All Rights Reserved.

Acknowledgements

First, I would like to thank my advisor Dr. Kivanc Ekici for his continuous academic guiding and financial assistance during the research work at the University of Tennessee, Knoxville. He was always available to answer questions and encouraged me when I had difficulties in my research. I also would like to acknowledge my committee members, Dr. Alexiades, Dr. Arimilli and Dr. Frankel, for their feedback and suggestions on my dissertation as well as teaching me some of the most interesting classes during my graduate education. In addition, my thanks go to Dr. Baker and Dr. Wong in the CFD lab for your their help with course studies and code programming.

This research was supported by a grant from the National Science Foundation (grant number: NSF-CBET-1150332) and by the MABE department.

I would like to thank my parents, Huang Chengwang and Huang Guifang, for their diligent education. This dissertation could not be accomplished without their encouragement and support.

Abstract

The high-dimensional harmonic balance (HDHB) method has recently become popular in the field of periodic unsteady flow prediction due to its accuracy and high efficiency. In the present dissertation research, two and three-dimensional parallelized computational fluid dynamic (CFD) codes based on the HDHB method are developed and validated for unsteady turbulent flows. It is found that the stability condition for an explicit solver is highly dependent on the reduced grid frequency, a non-dimensional parameter that depends on the grid size, characteristic wave speed, and the highest frequency retained in the harmonic balance solver. Furthermore, for certain moderately and highly nonlinear problems, the pseudo-spectral operator used in the HDHB method is found to introduce aliasing errors, which may lead to nonlinear instabilites or non-physical solutions. As a remedy, a temporal spectral viscosity operator is proposed for de-aliasing purpose so as to stabilize HDHB solver. The proposed method is validated for a simple nonlinear Duffing oscillator case and laminar vortex shedding over an oscillating circular cylinder at $Re = 500$. Another focus of this research is the design optimization of the turbomachinery blades for

unsteady flows. The "steady state" nature of the HDHB technique makes it very-well suited for an adjoint sensitivity analysis mainly due to the fact that the storage requirements are greatly reduced. To date, the investigators have used the adjoint technique mainly for steady shape optimization. To the author's best knowledge, the technique has not been applied for unsteady design optimization of turbomachinery blades. In this dissertation, a discrete adjoint HDHB method is employed for unsteady turbomachinery shape optimization. With the help of the automatic differentiation (AD) tool, TAPENADE, the development time for an optimization solver can be reduced substantially. Both inverse design and optimization problems are considered to validate the optimization solver.

Table of Contents

1 Introduction **1**

1.1 Time-Dependent CFD Algorithms 2

1.2 Gradient Based Optimization 7

1.3 Discrete Adjoint Method and Automatic Differentiation 9

1.4 Motivation and Objective 15

2 Governing Equations and Numerical Discretisation **17**

2.1 Governing Equations 18

2.2 Spatial Discretisation 21

2.3 High-Dimensional Harmonic Balance 25

2.4 Boundary Conditions 28

2.5 Temporal Spectral Viscosity 32

2.6 Another Point of View of The Pseudospectral Operator 35

2.7 Parallelization with OpenMP 37

3 Discrete Adjoint Method Using an Automatic Differentiation Tool **38**

4 Aerodynamic Shape Optimization Framework **46**

5 Results and Discussion **53**

5.1 HDHB Solutions 53

5.1.1 Tenth Standard Configuration 54

5.1.2 Eleventh Standard Configuration 66

5.1.3 Unsteady Laminar Flow Around a Stationary Circular Cylinder 77

5.1.4 Three-Dimensional Steady Flow through the NASA Rotor 67 Fan 84

5.1.5 Inviscid Analysis of Three-Dimensional Tenth Standard Configuration 87

5.1.6 Transonic Three-Dimensional Fourth Standard Configuration . 92

5.2 Stabilized HDHB Solutions with Temporal Spectral Viscosity 98

5.2.1 Stabilized HDHB for the Duffing Equation 98

5.2.2 Stabilized HDHB Solutions of Unsteady Flow Around an Oscillating Circular Cylinder 110

5.2.3 Effect of Temporal Spectral Viscosity on the Accuracy of Stable Unsteady Solutions 118

5.3 Aerodynamic Shape Optimization 121

5.3.1 Inverse Design for a Steady Quasi-One-Dimensional Nozzle . . 121

5.3.2 Inverse Design for Steady Tenth Standard Configuration . . . 127

5.3.3 Optimization for Unsteady Tenth Standard Configuration . . . 139

6 Conclusions and Future Work **156**

Bibliography **158**

Vita **177**

List of Tables

5.1 Inflow conditions for the 3-D Tenth Standard Configuration. 87

5.2 Inflow conditions for the 3-D Fourth Standard Configuration Case 628. 93

5.3 Comparison of the force coefficients. 113

5.4 Comparison of HDHB computational time. 117

List of Figures

3.1 Flow chart of a CFD solver. 43

3.2 Flow chart of an original adjoint solver. 44

3.3 Flow chart of a modified adjoint solver. 45

4.1 Flow chart for optimization process. 47

5.1 Computational grid for the Tenth Standard Configuration. 55

5.2 Pressure coefficient distribution for the Tenth Standard Configuration. Subsonic case. 56

5.3 Imaginary unsteady pressure coefficient distribution for the Tenth Standard Configuration. Subsonic case, σ=0 deg, ω^*=0.5. 57

5.4 Aerodynamic damping coefficient versus IBPA σ for the Tenth Standard Configuration. Subsonic case, ω^*=0.5. 58

5.5 Static pressure contours for the mean flow of the Tenth Standard Configuration. Transonic case. 61

5.6 Pressure coefficient distribution for the Tenth Standard Configuration steady state. Transonic case. 62

5.7 Imaginary unsteady pressure coefficient distribution for the Tenth Standard Configuration. Transonic case, σ=0 deg, ω^*=0.5. 63

5.8 Aerodynamic damping coefficient versus IBPA σ for the Tenth Standard Configuration. Transonic case, ω^*=0.5. 64

5.9 Convergence history for the Tenth Standard Configuration. Subsonic case. 65

5.10 Left: Computational grid for the Eleventh Standard Configuration. Right:Close-up of the grid near the trailing edge. 67

5.11 Streamline near the leading edge for the Eleventh Standard Configuration. 68

5.12 Steady state Mach number contour for the Eleventh Standard Configuration. 69

5.13 Isentropic Mach number surface distribution for the Eleventh Standard Configuration. 70

5.14 First Harmonic of unsteady pressure coefficient distribution for the Eleventh Standard Configuration, ω^*=0.309, σ=180 deg. 71

5.15 Aerodynamic damping coefficient versus IBPA σ for the Eleventh Standard Configuration, ω^*=0.309. 72

5.16 Pressure coefficient distribution for the Eleventh Standard Configuration with 10% motion, ω^*=0.309, σ=180 deg. 74

5.17 Pressure coefficient distribution for the Eleventh Standard Configuration, ω^*=0.309, σ=180 deg. 75

5.18 Second harmonic of unsteady pressure distribution on the blade surface for 1, 5 and 10% plunging, $\omega^* = 0.309$, $\sigma = 180$ deg. 76

5.19 Third harmonic of unsteady pressure distribution on the blade surface for 1, 5 and 10% plunging, $\omega^* = 0.309$, $\sigma = 180$ deg. 76

5.20 Computational grid for the circular cylinder. 78

5.21 Instantaneous velocity contours computed using the HB solver. 79

5.22 Convergence history for the HB solver. 80

5.23 Instantaneous velocity contours for a circular cylinder in cross flow. $Re = 176$. 81

5.24 Lift and Drag Coefficient for a Circular Cylinder 82

5.25 Strouhal Number Versus Reynolds Number 83

5.26 Hub and blade surface computational grid for the NASA Rotor 67 fan. 85

5.27 Experimental(o) and numerical solution (-) for NASA Rotor 67 fan: total pressure, static pressure, total temperature and flow angle distribution along radial direction at the exit (circumferentially averaged, near peak efficiency). 86

5.28 Isentropic Mach number distribution. 89

5.29 Imaginary part of unsteady pressure distribution, ω^*=0.5, σ=0 deg. . 90

5.30 Aerodynamic damping versus interblade phase angle, ω^*=0.5. 91

5.31 Left: computational grid for the Fourth Standard Configuration. Right: close-up of the grid near the tip clearance region. 94

5.32 Steady state Mach number contours for the Fourth Standard Configuration at 50% span location. 96
5.33 Steady state pressure coefficient for the Fourth Standard Configuration. 97
5.34 First harmonic of unsteady pressure coefficients, ω^*=0.1558, σ=180 deg. 97
5.35 Comparison of time-accurate and HDHB1 solutions of the first harmonic amplitude for the Duffing equation. 103
5.36 Comparison of harmonic amplitude of HDHB2 with and without TSV. 104
5.37 Multiple non-physical solutions of HDHB3 without TSV. 105
5.38 Harmonic amplitude of HDHB3 with temporal spectral viscosity. . . . 105
5.39 HDHB3 solution using different temporal spectral viscosity coefficients. 106
5.40 Physical correct solutions of HDHB8 without TSV. 107
5.41 Comparison of unstable solutions. 109
5.42 solutions using BDF and CDF operators 109
5.43 Computational grid for a circular cylinder. 114
5.44 Force coefficients over one vibration cycle with different harmonics. $Re = 500$, $Ma = 0.1$. 115
5.45 Instantaneous vortex contours over half a vibration cycle, Left: HDHB7+TSV, Middle Left: HDHB11+TSV, Middle Right: Time-accurate, Right: Blackburn and Henderson. (reproduced with permission). $Re = 500$, $Ma = 0.1$. 116
5.46 Convergence history for HDHB solver with different number of harmonics. 117

5.47 Mean pressure coefficient distribution for the Eleventh Standard Configuration, ω^*=0.309, σ=180 deg. 119
5.48 Imaginary part of the first harmonic (left) and the second harmonic (right) of surface pressure coefficient for the Eleventh Standard Configuration, ω^*=0.309, σ=180 deg. 120
5.49 Initial and target nozzle shape. 122
5.50 Initial and target nozzle pressure distribution. 123
5.51 A series of Hicks-Henne function. 124
5.52 Convergence history for inverse design of nozzle. 125
5.53 Optimized and target nozzle shape. 125
5.54 Optimized and target nozzle pressure distribution. 126
5.55 Comparison of the blade shapes for the Tenth Standard Configuration. 128
5.56 Convergence history for inverse design of the Ten Standard Configuration. 129
5.57 Comparison between the optimized and the target geometry and pressure. 130
5.58 Inverse design for the Tenth Standard Configuration, Case 2. 131
5.59 Computational grid for the NACA2408 airfoil. 133
5.60 Comparison of sensitivities of the new smoothed and unsmoothed method at the first optimization step for the NACA2408 airfoil geometry. 134
5.61 Comparison of sensitivities of the new smoothed and unsmoothed method in vector at the first optimization step for the NACA2408 airfoil geometry 135
5.62 Convergence history of for the Tenth Standard Configuration, Case 3. 136

5.63 Inverse design for the Tenth Standard Configuration, Case 3. 136
5.64 Mach number contours for inverse design the Tenth Standard Configuration, Case 3. 137
5.65 Pressure contours for inverse design the Tenth Standard Configuration, Case 3. 137
5.66 Convergence history for the steady adjoint solver and the steady CFD solver. 138
5.67 Convergence history for LCO reduced frequency of the Ten Standard Configuration. 140
5.68 Comparison aerodynamic damping versus IBPA for the Ten Standard Configuration, 1 harmonic. 141
5.69 Comparison of aerodynamic damping coefficient versus IBPA σ, ω^*=0.2, 1 harmonic. 143
5.70 Convergence history of unsteady shape optimization for the Tenth Standard Configuration. 144
5.71 Comparison of original Tenth Standard Configuration and optimized configuration geometry. 145
5.72 Comparison of the instantaneous Mach number contours, ω^*=0.2, σ=60 deg, 1 harmonic. 146
5.73 Comparison of the instantaneous static pressure contours, ω^*=0.2, σ=60 deg, 1 harmonic. 147

5.74 Comparison of the unsteady Mach number contours, ω^*=0.2, σ=60 deg, 1 harmonic. 148
5.75 Comparison of the unsteady pressure contours, ω^*=0.2, σ=60 deg, 1 harmonic. 149
5.76 Comparison of imaginary unsteady pressure coefficient distribution, ω^*=0.2, σ=60 deg, 1 harmonic. 150
5.77 Convergence history for the adjoint solver and unsteady CFD solver, 1 harmonic. 150
5.78 Solutions for nonlinear unsteady flow of the Tenth Standard Configuration, ω^*=0.2, σ=60 deg, 3 harmonics. 151
5.79 Comparison of the instantaneous Mach number contours, ω^*=0.2, σ=60 deg, 3 harmonics. 152
5.80 Comparison of the instantaneous static pressure contours, ω^*=0.2, σ=60 deg, 3 harmonics. 153
5.81 Comparison of the unsteady Mach number contours, ω^*=0.2, σ=60 deg, 3 harmonics. 154
5.82 Comparison of the unsteady pressure contours, ω^*=0.2, σ=60 deg, 3 harmonics. 155

Nomenclature

$\mathcal{A}$	surface of a control cell
$\boldsymbol{A}_n, \boldsymbol{B}_n$	the nth temporal Fourier coefficients
B	Hessian matrix
b_c	blade span length
c	chord length
C_p	mean or steady pressure coefficient
$C_{p(1)}$, $C_{p(2)}$, $C_{p(3)}$	first, second and third harmonic of unsteady pressure coefficient
$\boldsymbol{D}$	pseudo-spectral operator
$\boldsymbol{D}_2$	second-order temporal spectral operator
D_ϵ^2	second order difference operator
D_ϵ^4	fourth order difference operator
$\boldsymbol{E}, \boldsymbol{E}^{-1}$	discrete inverse Fourier and Fourier transformation matrices

e	total energy
$\dot{f}, \dot{g}, \dot{h}$	grid velocity
$\boldsymbol{F}, \boldsymbol{G}, \boldsymbol{H}$	conservation flux vectors
$\tilde{G}$	blade to blade gap
H	inverse of Hessian matrix
$\boldsymbol{I}$	objective function
I	rothalpy
$Ma = \frac{\sqrt{u^2+v^2+w^2}}{\sqrt{\gamma \frac{p}{\rho}}}$	Mach number
Ma_{ise}	isentropic Mach number
N	number of harmonics
$\boldsymbol{n}$	norm vector of control surface
p	pressure
Pr_l	laminar Prandtl number
Pr_t	turbulence Prandtl number
Q_c	convective flux terms
Q_d	artificial dissipative terms

Q_v	viscous flux terms
R	radius
R_{gas}	gas constant
$\boldsymbol{R}$	residual vector
$\boldsymbol{R}^*$	residual vector at all sub-time levels
Re	Reynolds number
$\boldsymbol{S}$	source vector
S_t	turbulence source term
St	Strouhal number
T	period
t	time
$\boldsymbol{U}$	conservation variables vector
$\boldsymbol{U}^*$	conservation variables vector at all sub-time levels
u, v, w	Cartesian velocities
$\mathcal{V}$	volume of a control cell
$\boldsymbol{x}$	design variable

x, y, z	Cartesian coordinates
Ω	rotational speed of the cascade
Ξ	aerodynamic damping coefficient
α	flow angle
ϵ_N	temporal viscosity coefficient
γ	specific heat ratio
λ	spectral radius of flux Jacobian
μ_l	laminar viscosity
μ_t	turbulence viscosity
ω	excitation frequency
$\omega^* = \frac{\omega c}{u_{ref}}$	full chord reduced frequency, $u_{ref} = u_{inlet}$ for a compressor, $u_{ref} = u_{outlet}$ for a turbine
ψ	adjoint variable
ρ	density
ρ_n	Fourier cut-off function
σ	interblade phase angle
τ	pseudo-time

τ_{xx},τ_{xy}, etc.	shear stress
$\tilde{\nu}$	turbulence working variable

Chapter 1

Introduction

Computational fluid dynamic tools play an important role in modern aircraft and turbomachinery design process. The high-fidelity numerical methods provide reliable aerodynamic predictions at a substantially lower cost compared to the traditional wind tunnel design, especially at an early design stage. With the advancement of computing technology, it is now feasible to perform unsteady design and shape optimization with the aim of improving aerodynamic performance and reliability of aircraft and turbomachinery. The main objective of the research is to develop an efficient discrete adjoint technique with the aim of turbomachinery blade shape optimization.

1.1 Time-Dependent CFD Algorithms

The flow fields in turbomachinery are fundamentally unsteady because of wake interactions or self-excited flutter vibration of blades. An accurate and efficient prediction of unsteady flows in turbomachinery is the first and most critical step in an optimization design process.

Since early 1980s, the development of time-dependent CFD algorithms attracted a great amount of research attention. Earlier approaches for time-dependent CFD computations were based on time-accurate methods, such as the Lax-Wendroff scheme[1]. However, physical time step selection in such an explicit scheme is heavily restricted by the CFL condition. Thus, the computational cost becomes prohibitive.

A practical time-dependent CFD computation became a reality when Jameson [2] introduced the so called dual-time stepping method in 1991. In the dual-time stepping method, the temporal derivative term in the Euler or Navier-Stokes equations is approximated by a second-order backward difference operator. In order to solve the discretised equations, a pseudo-time derivative term is added to the equations. In this approach, convergence acceleration techniques designed for steady state computation, such as local time stepping, implicit residual smoothing[3] and multigrid[4], can be used to speed up the time-dependent computations. The solution is marched from one time level to the next one. When each time level solution converges, the pseudo-time derivative term vanishes and so the original equations are recovered. In practice, the solution is said to be "converged" if the residual of inner iterations drops three or four

orders of magnitude. Since there are no assumptions made within the time-domain method, it can model the nonlinear effects of the turbomachinery flows accurately in a straightforward way[5–7]. However, the computational cost can easily become very high for large scale problems, such as unsteady turbomachinery computations with multistage coupling. Furthermore, the time-accurate method is not suitable for the adjoint optimization, which may require storage of all intermediate flow solutions, making it extremely expensive.

Considering most of the unsteady problems of interest in turbomachinery are periodic in time, the frequency domain techniques provide good alternatives to the time-accurate methods mentioned above. In the time-linearised method [8, 9], the unsteadiness is assumed to be small compared to the mean flow and to be harmonic in time. Therefore, the nonlinear unsteady governing equations are decoupled into nonlinear steady equations and linear unsteady equations, which are solved in sequence. The total computational cost is approximately three times the steady computation. However, using this technique, nonlinear effects cannot be modeled because of the fundamental small perturbation assumption.

To model nonlinear effects, Hall et al.[10] applied the classical harmonic balance technique, which is a nonlinear frequency-domain method, to model the Euler equations. They represented the flow by a Fourier series in time, where the dependent variables were Fourier coefficients of the conservation variables. These Fourier series were inserted into the Euler equations and then resulting expressions were "balanced" according to the order of harmonics. The harmonic balance can model both linear

and nonlinear unsteady problems. For linear unsteady problems, the harmonic balance method should yield identical solutions to the time-linearised method. In addition, it has the ability to model the nonlinear effects accurately for nonlinear flows of interest. Although the classical harmonic balance is rather straightforward for the Euler equations, the algebraic balancing does not work well for the Reynolds-averaged Navier-Stokes equations with complex turbulence models. To overcome this problem, Hall et al.[10] proposed a high-dimensional harmonic balance method in which the conservation variables were stored and computed at several sub-time levels that are equally spaced over one periodic cycle. Those sub-time level solutions are coupled through a pseudo-spectral operator, which approximates the physical time derivative in the Euler or Navier-Stokes equations. Also, the resulting equations are mathematically steady state, therefore, convergence acceleration techniques, originally designed for steady state computation, can be employed to speed up the convergence rate. A variation of the HDHB method is the non-linear frequency domain (NLFD) method developed by McMullen and Jameson[11, 12]. In this approach, the dependent variables are Fourier coefficients, requiring the FFT and inverse FFT of conservation variables and residuals between time and frequency domains at every single iteration. Although the two methods are identical, HDHB is easier to implement into an established steady state solver and avoids the FFT and inverse FFT . Thanks to the benefits mentioned above, the HDHB method has been used in various CFD applications, such as unsteady flows over helicopter rotors[13], aeroelastic analysis in cascades[14], laminar vortex shedding over a circular

cylinder[15–17] and prediction of limit-cycle oscillations[18, 19]. In its original form, the number of harmonics retained is uniform in the entire computational domain and it is necessary to perform a mode convergence study to determine the sufficient number of harmonics for specific problems. However, the strength of unsteadiness usually varies at different locations. For example, there may be strong unsteadiness near the wake region of a circular cylinder, while the disturbances do not travel upstream. Therefore, one could improve the computational efficiency by retaining fewer number of harmonics in the upstream regions. To demonstrate the idea, Maple et al. [20] first proposed an adaptive harmonic method for one-dimensional Euler equations. Later on, Mosahebi and Nadarajah[21, 22] extended the idea to the NLFD method and presented solutions to laminar vortex shedding over a two-dimensional circular cylinder and a NACA0012 airfoil.

Periodic unsteady problems can be classified into two categories. In the first category, the periodic frequency is predefined by an external forcing function. For example, flows of a helicopter rotor or a wind turbine are driven by the rotation of the rotor or the turbine. In turbomachinery aeroelastic analysis, the unsteady flow field may be dominated by self-excited blade vibrations. In the other category, the frequency of unsteady problems is not known a *priori*. For instance, the unsteadiness of vortex shedding over a stationary circular cylinder is triggered by the instability of fluid flow rather than an external forcing function. The shedding frequency is actually a part of the solution rather than a predefined parameter. However, the harmonic balance method requires the excitation frequency as a input parameter. Therefore,

special techniques[15–17] have been developed to determine the frequency during the harmonic balance iterations, which will be discussed in detail in Section 2.3.

Initially, the HDHB method was implemented in an explicit CFD solver[10]. Instability issues were reported occasionally when a large number of harmonics are retained or when the excitation frequency is very high. van der Weide et al.[23] proposed a constraint on the local time step for the explicit Runge-Kutta scheme by taking into account the excitation frequency and the number of harmonics. Implicit treatment of the pseudo-spectral term was proposed by Custer[24] and Campobasso et al.[25] to enhance the stability of the HDHB solver. These stabilization techniques are similar to the technique commonly used to stabilize an explicit dual-time stepping scheme[26]. More recently, Sicot et. al[27], Woodgate and Badcock[28] and Su and Yuan[29] demonstrated the robustness and stability of HDHB for implicit solvers.

One of the disadvantages of the HDHB compared to the classical HB is the introduction of aliasing errors through the discrete Fourier transformation (DFT) of nonlinear terms. The source of aliasing errors and its influence on the stability and convergence are discussed in detail in a review paper[30]. Aliasing errors are blamed for the instability encountered in a multi-stage coupled turbomachinery computation[31]. Liu et al.[32] demonstrated the existence of aliasing errors by expanding HDHB analytically for the Duffing equation and their numerical tests revealed that HDHB solver failed to converge in certain cases or converged to non-physical solutions in others. Later on, LaBryer and Attar[33] managed to obtain

physically correct HDHB solutions for the nonlinear Duffing equaltion using a one-half rule filter or a Fourier smoothing filter. The idea of filtering is to include more sub-time solutions and the higher harmonics obtained from DFT are eliminated, which results in the lower harmonics to be free of aliasing errors.

In this dissertation, a temporal spectral viscosity, similar to the spatial spectral viscosity method commonly used in the pseudo-spectral method[34, 35], is proposed for de-aliasing so as to stabilize HDHB solvers.

1.2 Gradient Based Optimization

Depending on the requirement of the sensitivity information, mathematical optimization algorithms can be classified into two categories: non-gradient and gradient based[36]. In the first approach, only objective function evaluations are used to find the optimum point in the design space, and the gradient and the Hessian of the objective function are not required. Some non-gradient methods have the advantage of being capable of identifying the global minimum. Global optimization methods include deterministic methods, stochastic methods and heuristics methods. Unfortunately, these methods need a large number of design cycles to obtain an optimal solution. Furthermore, the convergence to the global minimum is not guaranteed when there is a large amount of design variables.

To find a local minimum of an objective function using a gradient based optimization, one needs to determine the search direction and a step size at the

current point. The simplest gradient based optimization is known as the steepest descent, in which the search direction is taken as the opposite of the gradient. As a first-order optimization algorithm, the convergence to a local minimum requires a large number of iterations, on the order of N^2, where N is the number of design parameters. A second-order optimization method, known as the Newton's method, converges at a quadratic rate. However, it requires computation of the second-order derivative matrices, also known as the Hessians, at each iteration. The computational cost for evaluating the exact Hessian in CFD shape optimization can be prohibitive. In quasi-Newton methods, the Hessian does not need to be computed exactly, while it is approximated by the changes in the gradients between each iteration. The first quasi-Newton algorithm was proposed in 1959 by Davidon[37], a physicist at Argonne National Laboratory. Ironically, his paper was not well regarded until it was published in the first volume of SIAM Journal of Optimization in 1991. Today, the algorithm is also known as the DFP updating formula (named after William C. Davidon, Roger Fletcher, and Michael J. D. Powell)[36]. The DFP formula is effective, but it was soon superseded by the BFGS method (suggested independently by Broyden, Fletcher, Goldfarb and Shanno in the 1970s)[36].

1.3 Discrete Adjoint Method and Automatic Differentiation

In a gradient based optimization, it is crucial to obtain the gradient in an accurate and efficient way. For turbomachinery blade shape optimization, the number of design parameters may be on the order of hundreds or even thousands. The gradients can be approximated by finite difference in a straight-forward manner. In the finite difference approach, one takes a small perturbation of each design variable, performs a nominal CFD calculation to determine the objective function and then determines the partial derivative. The computation of the gradients associated with N design variables requires at least $(N + 1)$ flow field computations. The gradient based optimization using finite differences in aerodynamic design can be traced back to 1970s. Hicks et al.[38] were the pioneers who applied the finite difference method to evaluate the gradients for 2-D shape optimization using potential flow equations. All early design works were restricted to a small number of design variables and low fidelity flow models because of the high computational cost associated with the finite difference gradient evaluation. Further, the perturbation step size needs to be picked carefully to minimize the cancellation errors in the finite difference method. In theory, the gradients obtained from a finite difference method can be accurate only up to the order of $\mathcal{O}(10^{-8})$ if double precision is used in the CFD computation.

The idea of the adjoint method was first introduced in fluid mechanics by Pironneau[39]. Later on, Jameson[40] successfully extended the adjoint method to

aerodynamic shape optimization. This method eliminates the explicit dependence of the gradient on the variation of flow fields through the introduction of an adjoint variable. The computational cost of the adjoint equation can be approximately five times the cost of the flow field computation. Therefore, the total computational cost is somewhat independent of the number of design variables, making it very promising in the aerodynamic shape optimization where a large number of design variable is considered.

There are mainly two families of adjoint methods: continuous and discrete[41]. In the continuous approach, the adjoint equation is derived from the governing differential equations, which are then discretised. In the discrete approach, on the other hand, the adjoint equation is formulated directly from the discretised PDEs. Jameson and his colleagues performed continuous adjoint shape optimization for airfoils, wings and wing-body configurations with Euler or Reynolds-averaged Navier-Stokes equations[42–44]. Luo et al.[45] extended the continuous adjoint method to internal flows for turbomachinery shape optimization using 3-D Euler equations. The main advantage of the continuous approach is that it gives insight to the PDEs directly. However, there are three drawbacks for the continuous adjoint method. The differentiation of the PDEs, followed by a discretisation leads to an inconsistency between the computed gradient and that of the discrete implementation because of the artificial dissipation terms in the discretised equations. Thus, the convergence of a gradient based optimization algorithm could be hampered by the inconsistent gradient. Secondly, boundary conditions for the adjoint variables are not very easy to

define, certain assumptions need to be made. Thirdly, it may be difficult to derive the adjoint equations for complex turbulence model equations. In practice, the turbulence field is assumed to be constant and independent of the design variables. In addition, the viscous terms are so complicated that it makes it quite challenging to implement.

In contrast to the continuous adjoint method, the sensitivities (i.e. gradients of the objective function with respect to the design variables) obtained from the discrete adjoint method are consistent with the CFD code, including the boundary conditions and the turbulence model. This approach can also be very tedious if one were to differentiate a complex CFD code by hand. Furthermore, if a part of the original CFD code is changed, the discrete adjoint code has to be changed accordingly. Therefore, it is not easy to maintain the hand-written discrete adjoint code. Elliott and Peraire[46] hand-coded a discrete adjoint code and used it for a 3D shape optimization problem. Nielsen and Anderson[47] and Anderson and Bonhaus[48] at NASA Langley have also implemented a hand-written discrete adjoint code with turbulence effects. The difficulty when implementing a discrete adjoint code can be greatly eased with the help of an automatic differentiation (AD) tool. In the aerospace field, Mohammadi and Pironneau[49] were the first to employ an AD tool for adjoint code development. For small applications, it is possible to use AD as a "black box", feeding in a nonlinear code to an AD tool and obtaining a corresponding linear perturbation (forward mode AD) or adjoint (reverse mode AD) code. However, in real applications with very large codes, such as an iterative CFD code, the memory requirement becomes unaffordable

with a "black box" approach. Thus, it is usually necessary to apply the AD very selectively.

Giles and Pierce[50], Giles et al.[51], Giles et al.[52] have contributed substantially to adjoint based CFD design through an AD tool. They used the reverse mode of an AD tool and then assembled the differentiated subroutines to form the adjoint system. The resulting linear system was solved using the same iterative scheme as the original CFD solver. Since the CFD iterative algorithm was "highly optimized", the adjoint solver had the same convergence rate as the CFD solver. However, extra efforts were put into the implementation to utilize convergence acceleration techniques, such as implicit residual smoothing and multigrid. Duta et al.[53] applied the method to optimize the NASA Rotor 37 tubomachinery blade. The isentropic efficiency was raised by one percent using an SQP algorithm with a constraint on the stage pressure ratio value.

Instead of using a fixed point iteration method, Mader and Martins[54] proposed to use the preconditioned GMRES[55] technique in the well-tuned linear algebra package PETSc[56]. He and his co-authors[57, 58] have presented 3D inviscid optimizations for complex wing bodies. However, others[47, 48] have reported convergence problems associated with the p-GMRES solver if the adjoint RANS equations were fully coupled with adjoint turbulence equations, because the turbulence model makes the system less diagonally dominant.

Most adjoint sensitivity analyses in aerodynamic design optimization have focused on steady flows, because the reversal nature of the adjoint calculation normally

requires the entire time history of the flow computation to be stored. However, there have been a few attempts to apply the adjoint method to unsteady time-domain solvers[59, 60]. Wang[61] developed a checkpointing algorithm, which significantly reduces the data storage at the expense of increased computational cost. In another work, Beran et al.[62] developed an elegant technique in which they used proper orthogonal decomposition (POD) to compress the history of time-accurate computations greatly decreasing the storage requirements. As mentioned earlier, the frequency-domain techniques, HDHB and NLFD, are mathematically steady. Therefore, it is straight-forward to extend the adjoint method to these techniques[63–66]. Choi et al.[65] employed the discrete adjoint method with HDHB for helicopter rotor design. In their work, over 100 design variables were chosen and the optimized configuration showed good performance improvement, amounting to a 2% decrease in torque and 7% increase in thrust compared to the initial configuration. Mader et al.[66] have analyzed the sensitives of an oscillating ONERA M6 wing. To the author's best knowledge, there has been no research reported in the literature on the use of the adjoint method for unsteady turbomachinery shape optimization, which is one of the focus points of this research.

In mathematics and computer science, automatic differentiation (AD), also known as algorithmic differentiation, is a technique that analytically evaluates the derivatives of a computer program. An AD tool applies the chain rule to each operation of the input source code so as to obtain the derivatives. There are two differentiation modes in AD: forward mode (linear mode) and reverse mode (adjoint mode). In

the forward mode, a seed of linear derivative is given at the beginning of the code, the derivatives of the objective functions with respect to the seed are obtained after a forward execution. In the reverse mode, a seed of adjoint derivative is given at the end of the code, then the code is run in reverse reaching the beginning of the code. The intermediate variables need to be stored in the forward execution or recomputed from the beginning. The reverse mode is more efficient if the number of design variables is larger than that of the objective functions, which is generally the case for aerodynamic shape optimization. There are two approaches for AD tools to implement AD: source code transformation and operator overloading. In the source code transformation approach, the original code for a function evaluation is replaced by an automatically generated source code that includes not only the original instructions but also the statements for evaluating its derivative. The operator overloading approach is implemented by new user defined data types instead of original floating point numbers. This new data type stores not only the original variable value, but also the derivative. AD tools are available for a variety of programming languages, such as FORTRAN, C/C++ and Matlab. Interested readers can refer to www.autodiff.org for details. In this work, TAPENADE[67] is chosen. TAPENADE is a noncommercial, source code transformation AD tool, supporting both forward and reverse mode for differentiation of FORTRAN source codes.

1.4 Motivation and Objective

In order to take advantage of high-fidelity CFD analysis solutions, it is necessary to include a large number of design variables when performing turbomachinery shape optimization. Although non-gradient algorithms were used for shape optimization in the literature, it is generally accepted that non-gradient algorithms become infeasible for more than 20 or 30 design variables. In gradient based optimizations, the derivative evaluation cost scales linearly with the number of design variables if one uses a finite difference method. The benefit of using an adjoint method to evaluate the derivates of the objective function with respect to large number of design variables becomes prominent. In this dissertation, a discrete adjoint method, based on the HB flow solver, has been developed for turbomachinery shape optimization to improve unsteady aeroelastic characteristics.

The objective of this dissertation research is to investigate an easier implementation strategy for developing a computational efficient adjoint solver for unsteady turbomachinery blade shape optimization using the HDHB method.

The specific aims include:

1. Development and validation of two- and three-dimensional parallelized HDHB CFD codes.

2. Development of the temporal spectral viscosity technique to stabilize HDHB solvers for strongly nonlinear problems.

3. Development and validation of an efficient discrete adjoint solver for sensitivity analysis with partial codes generated by TAPENADE. The CFD code, the adjoint sensitivity code and the optimization code are combined to develop a framework for inverse design and shape optimization of turbomachinery blades. As mentioned earlier, to the best knowledge of the author, this is the first work in the literature that applies the adjoint method for unsteady turbomachinery shape optimization.

Chapter 2

Governing Equations and Numerical Discretisation

This chapter presents the essence of a CFD solver. Section 2.1 describes the integral conservative forms of the Reynolds-averaged Navier-Stokes equations and the non-dimensionalization. Section 2.2 presents the spatial discretisation method for the RANS equations. Section 2.3 discusses the temporal discretisation of the RANS equations using the high-dimensional harmonic balance method. Section 2.4 describes the boundary conditions used in the work and the modified local time step condition and frequency search techniques. Section 2.5 explains the stabilization technique: temporal spectral viscosity. Section 2.6 explains its relationship to other stabilization techniques. Section 2.7 describes parallelization of the CFD code.

2.1 Governing Equations

In turbomachinery, it is appropriate to write the time-dependent three-dimensional Reynolds-averaged Navier-Stokes equations in the frame of reference attached to the cascades that rotate with a rotational speed, Ω. Considering that a finite volume scheme will be employed for discretisation, the governing equations can be written in an integral conservation form[68] as

$$\frac{\mathrm{d}}{\mathrm{d}t}\iiint_{\mathcal{V}} \boldsymbol{U}\,\mathrm{d}\mathcal{V} + \iint_{\mathcal{A}} \left[\boldsymbol{F} - \boldsymbol{U}\dot{f}, \boldsymbol{G} - \boldsymbol{U}\dot{g}, \boldsymbol{H} - \boldsymbol{U}\dot{h}\right] \cdot \boldsymbol{n}\,\mathrm{d}\mathcal{A} = \iiint_{\mathcal{V}} \boldsymbol{S}\,\mathrm{d}\mathcal{V}. \tag{2.1}$$

In the above equation, the vector of conservation variables $\boldsymbol{U}$ and flux vectors $\boldsymbol{F}$, $\boldsymbol{G}$ and $\boldsymbol{H}$ are given by

$$\boldsymbol{U} = \begin{bmatrix} \rho \\ \rho u \\ \rho v \\ \rho w \\ \rho e \\ \rho\tilde{\nu} \end{bmatrix}, \boldsymbol{F} = \begin{bmatrix} \rho u \\ \rho u^2 + p - \tau_{xx} \\ \rho uv - \tau_{xy} \\ \rho uw - \tau_{xz} \\ \rho uI - \tau_{xh} \\ \rho u\tilde{\nu} - \tau_{x\nu} \end{bmatrix}, \boldsymbol{G} = \begin{bmatrix} \rho v \\ \rho vu - \tau_{yx} \\ \rho v^2 + p - \tau_{yy} \\ \rho vw - \tau_{yz} \\ \rho vI - \tau_{yh} \\ \rho v\tilde{\nu} - \tau_{y\nu} \end{bmatrix}, \boldsymbol{H} = \begin{bmatrix} \rho w \\ \rho wu - \tau_{zx} \\ \rho wv - \tau_{zy} \\ \rho w^2 + p - \tau_{zz} \\ \rho wI - \tau_{zh} \\ \rho w\tilde{\nu} - \tau_{z\nu} \end{bmatrix},$$

where $\dot{f}$, $\dot{g}$ and $\dot{h}$ are the x, y and z components of the unsteady grid velocity, respectively. In addition, the source vector $\boldsymbol{S}$ is given by

$$\boldsymbol{S} = \begin{bmatrix} 0 \\ 0 \\ \rho(\Omega^2 y + 2\Omega w) \\ \rho(\Omega^2 z - 2\Omega v) \\ 0 \\ S_t \end{bmatrix},$$

where Ω is the rotational speed. Note that the last entry in the governing equations correspond to the Spalart-Allmaras turbulence model equation[69] written in the strong conservation form. For an ideal gas with a constant specific heat ratio, the pressure p and the rothalpy I can be defined as

$$p = (\gamma - 1)\rho \left[e - \frac{1}{2}(u^2 + v^2 + w^2) + \frac{1}{2}\Omega^2 R^2 \right],$$

$$I = \frac{\rho e + p}{\rho} = \frac{\gamma}{\gamma - 1}\frac{p}{\rho} + \frac{1}{2}(u^2 + v^2 + w^2) - \frac{1}{2}\Omega^2 R^2,$$

where R is the radius, defined as $R = \sqrt{y^2 + z^2}$. In addition, the shear stress terms are defined as

$$\tau_{xx} = (\mu_l + \mu_t)\left(\frac{4}{3}\frac{\partial u}{\partial x} - \frac{2}{3}\frac{\partial v}{\partial y} - \frac{2}{3}\frac{\partial w}{\partial z} \right),$$

$$\tau_{xy} = (\mu_l + \mu_t)\left(\frac{\partial u}{\partial y} + \frac{\partial v}{\partial x} \right),$$

$$\tau_{xz} = (\mu_l + \mu_t)\left(\frac{\partial u}{\partial z} + \frac{\partial w}{\partial x}\right),$$

$$\tau_{xh} = u\tau_{xx} + v\tau_{xy} + w\tau_{xz} + \left(\frac{\mu_l}{Pr_l} + \frac{\mu_t}{Pr_t}\right)\frac{\partial I}{\partial x},$$

where the laminar viscosity μ_l is determined by Sutherland's law. The turbulence viscosity μ_t is computed by the standard Spalart-Allmaras turbulence model[69],

$$\mu_t = \rho\tilde{\nu} f_{v1}(\chi),$$

where

$$f_{v1}(\chi) = \frac{\chi^3}{\chi^3 + 7.1^3}, \chi = \frac{\mu_t}{\mu_l}.$$

It should be noted that the inviscid fluxes and the source terms depend on the conservation variables and the Cartesian coordinates. The viscous fluxes depend on the gradients of the flow velocities, the temperature and the working turbulent variable.

When developing a CFD code, it is desirable to normalize the governing equations. On one hand, normalization transforms numerous flow variables into a few non-dimensional parameters, such as the Reynolds number. On the other hand, the orders of magnitude discrepancy among the dimensional variables can be alleviated by an appropriate choice of non-dimensional parameters so as to minimize the round-off errors in computations. In this dissertation, the free stream total pressure P_{ref}, the free stream total temperature T_{ref} and the chord length L_{ref} are chosen as the

non-dimensional parameters. Therefore, the non-dimensional variables can be defined as:

$$\begin{aligned}
&\hat{t} = \frac{t}{L_{ref}/\sqrt{R_{gas}T_{ref}}}, \hat{x} = \frac{x}{L_{ref}}, \hat{y} = \frac{y}{L_{ref}}, \hat{z} = \frac{z}{L_{ref}}, \\
&\hat{u} = \frac{u}{\sqrt{R_{gas}T_{ref}}}, \hat{v} = \frac{v}{\sqrt{R_{gas}T_{ref}}}, \hat{w} = \frac{w}{\sqrt{R_{gas}T_{ref}}}, \\
&\hat{p} = \frac{p}{P_{ref}}, \hat{T} = \frac{T}{T_{ref}}, \hat{\rho} = \frac{\rho}{P_{ref}/R_{gas}T_{ref}}, \\
&\hat{\mu} = \frac{\mu}{P_{ref}L_{ref}/\sqrt{R_{gas}T_{ref}}}, \hat{\Omega} = \frac{\Omega}{\sqrt{R_{gas}T_{ref}}/L_{ref}}.
\end{aligned} \tag{2.2}$$

Substituting the above non-dimensional variables into Eq. (2.1), the non-dimensional Reynolds number is found to be unit. Therefore, the normalized RANS equations are found to be the same as the original form.

2.2 Spatial Discretisation

The spatial discretisation for the RANS equations employs a vertex-centered central difference finite volume method proposed by Jameson [4]. The control volume is formed by taking the union of cells that meet at that vertex. In two-dimensional cases, the control volume is made of four cells whereas the control volume is made of eight cells in three-dimensional cases. A semi-discrete form of the Navier-Stokes equations can be written as

$$\frac{\mathrm{d}}{\mathrm{d}t}(\mathcal{V}\boldsymbol{U}) + Q_c(\boldsymbol{U}) + Q_v(\boldsymbol{U}) - Q_d(\boldsymbol{U}) = 0, \tag{2.3}$$

where $\mathcal{V}$ is the cell volume. The convective terms, $Q_c(\boldsymbol{U})$, at the cell surface center are evaluated by averaging the conservation variables at the corresponding cell vertex. The physical viscous terms, $Q_v(\boldsymbol{U})$, are determined by a compact stencil central difference formulation[70], which may reduce the odd-even decoupling. The flux balance at each vertex can be determined by summing all the flux balance of its constitute cells. $Q_d(\boldsymbol{U})$ denotes to the artificial dissipative terms.

A blend of second and fourth order dissipative terms, based on the JST's formulation[71], are added to eliminate odd-even decoupling and near shock oscillations, and are given by

$$Q_d(\boldsymbol{U}) = (D_\xi^2 - D_\xi^4 + D_\eta^2 - D_\eta^4 + D_\zeta^2 - D_\zeta^4)\,\boldsymbol{U}. \tag{2.4}$$

The second and fourth difference operators can be written as

$$D_\xi^2\,\boldsymbol{U}_{i,j,k} = \bigtriangledown_\xi \left[\overline{\lambda}_{\xi i+\frac{1}{2},j,k} \cdot \epsilon^{(2)}_{i+\frac{1}{2},j,k}\right] \bigtriangleup_\xi\, \boldsymbol{U}_{i,j,k},$$

$$D_\xi^4\,\boldsymbol{U}_{i,j,k} = \bigtriangledown_\xi \left[\overline{\lambda}_{\xi i+\frac{1}{2},j,k} \cdot \epsilon^{(4)}_{i+\frac{1}{2},j,k}\right] \bigtriangleup_\xi \bigtriangledown_\xi \bigtriangleup_\xi\, \boldsymbol{U}_{i,j,k},$$

where $\bigtriangleup_\xi$ and $\bigtriangledown_\xi$ are the forward and the backward difference operators in ξ-direction, respectively. Following References[72]and [73], the variable scaling factor, $\overline{\lambda}$, is taken to be the maximum eigenvalues of the Jacobian matrices in order to alleviate the

effect of the high aspect ratio grids used in viscous computations. The $\overline{\lambda}$ is defined as

$$\overline{\lambda}_{\xi i+\frac{1}{2},j,k} = \lambda_{\xi i+\frac{1}{2},j,k} \cdot \Phi_{i+\frac{1}{2},j,k},$$

$$\Phi_{i+\frac{1}{2},j,k} = 1 + max\left[\left(\frac{\lambda_{\eta i+\frac{1}{2},j,k}}{\lambda_{\xi i+\frac{1}{2},j,k}}\right)^{\alpha}, \left(\frac{\lambda_{\zeta i+\frac{1}{2},j,k}}{\lambda_{\xi i+\frac{1}{2},j,k}}\right)^{\alpha}\right],$$

$$\lambda_{\xi i+\frac{1}{2},j,k} = \left|u_{i+\frac{1}{2},j,k} \cdot \mathbf{S}_{\xi i+\frac{1}{2},j,k}\right| + c\left|\mathbf{S}_{\xi i+\frac{1}{2},j,k}\right|,$$

$$\lambda_{\eta i+\frac{1}{2},j,k} = \left|u_{i+\frac{1}{2},j,k} \cdot \mathbf{S}_{\eta i+\frac{1}{2},j,k}\right| + c\left|\mathbf{S}_{\eta i+\frac{1}{2},j,k}\right|,$$

$$\lambda_{\zeta i+\frac{1}{2},j,k} = \left|u_{i+\frac{1}{2},j,k} \cdot \mathbf{S}_{\zeta i+\frac{1}{2},j,k}\right| + c\left|\mathbf{S}_{\zeta i+\frac{1}{2},j,k}\right|,$$

where $u_{i+\frac{1}{2},j,k}$ denotes the velocity vector, $\mathbf{S}$ denotes the surface normal vector and c is the speed of sound. It is found that $\alpha = 0.5$ yields a robust scheme. The pressure has been chosen as a switch to determine of the smoothing coefficients $\epsilon^{(2)}$ and $\epsilon^{(4)}$ as follows

$$\epsilon^{(2)}_{i+\frac{1}{2},j,k} = k^{(2)} max(\nu_{i-1,j,k}, \nu_{i,j,k}, \nu_{i+1,j,k}, \nu_{i+2,j,k}),$$

$$\nu_{i,j,k} = \left|\frac{p_{i-1,j,k} - 2p_{i,j,k} + p_{i+1,j,k}}{p_{i-1,j,k} + 2p_{i,j,k} + p_{i+1,j,k}}\right|,$$

$$\epsilon^{(4)}_{i+\frac{1}{2},j,k} = max\left\{0, \left[k^{(4)} - \epsilon^{(2)}_{i+\frac{1}{2},j,k}\right]\right\},$$

where $k^{(2)}$ and $k^{(4)}$ are constants.

After discretising the spatial terms, the ordinary differential equations are marched temporally toward a steady state solution with a modified multi-stage Runge-Kutta

scheme. At the $(q+1)$-st stage

$$\boldsymbol{U}_{q+1} = \boldsymbol{U}_q - \alpha_{q+1}\frac{\Delta t}{\mathcal{V}}\left[Q_c(\boldsymbol{U}^{(q)}) + Q_v(\boldsymbol{U}^{(0)}) - \Sigma_{r=0}^{q}\gamma_{qr}Q_d(\boldsymbol{U}^r)\right]. \tag{2.5}$$

An efficient choice of five stage coefficients is given by

$$\alpha_1 = \frac{1}{4}, \alpha_2 = \frac{1}{6}, \alpha_3 = \frac{3}{8}, \alpha_4 = \frac{1}{2}, \alpha_5 = 1.$$

To save computational cost and maintain a good high frequency error damping property, the physical viscous term Q_v is frozen at the first stage and the artificial dissipative term Q_d is evaluated only at the first, the third and the fifth stage. The weight factors satisfy the condition $\Sigma\gamma_{qr} = 1$ and they are defined as:

$$\gamma_{00} = 1,$$

$$\gamma_{10} = 1, \gamma_{11} = 0,$$

$$\gamma_{20} = \Gamma_3, \gamma_{21} = 0, \gamma_{22} = \overline{\gamma}_3,$$

$$\gamma_{30} = \Gamma_3, \gamma_{31} = 0, \gamma_{32} = \overline{\gamma}_3, \gamma_{33} = 0,$$

$$\gamma_{40} = \Gamma_3\Gamma_5, \gamma_{41} = 0, \gamma_{42} = \overline{\gamma}_3\Gamma_5, \gamma_{43} = 0, \gamma_{44} = \overline{\gamma}_5,$$

where $\Gamma_3 = (1 - \overline{\gamma}_3)$, $\Gamma_5 = (1 - \overline{\gamma}_5)$, $\overline{\gamma}_3 = 0.56$ and $\overline{\gamma}_5 = 0.44$.

Further details about the convergence acceleration techniques, such as implicit residual smoothing and multigrid can be found in Reference[74]. It should be noted that the turbulence equation is frozen on the finest grid in our codes, the multigrid cycle computations are not carried out for the turbulence model equation.

2.3 High-Dimensional Harmonic Balance

For many flows of interest in turbomachinery aerodynamics, the response (when viewed in the relative frame of reference) is periodic in time, with period $T = 2\pi/\omega$. Because the flow is temporally periodic, the flow variables may be approximated as a Fourier series in time with spatially varying coefficients. For example, the conservation variables may be expressed as a truncated Fourier series given by

$$\boldsymbol{U}(x,y,z,t_i) = \boldsymbol{A}_0(x,y,z) + \sum_{n=1}^{N} \left[\boldsymbol{A}_n(x,y,z)\cos(\omega n t_i) + \boldsymbol{B}_n(x,y,z)\sin(\omega n t_i)\right]; \quad i = 1 : 2N+1, \tag{2.6}$$

where ω is the fundamental excitation frequency, and $\boldsymbol{A}_0$, $\boldsymbol{A}_n$ and $\boldsymbol{B}_n$ are the Fourier coefficients of the conservation variables. It is noted that the flow variables are computed and stored at $(2N+1)$ equally spaced points over one temporal period. Following Eq.(2.6), the Fourier coefficients can be determined from the sub-time level solutions by a discrete Fourier transform, i.e.

$$\boldsymbol{U}^* = \boldsymbol{E}^{-1}\,\tilde{\boldsymbol{U}}. \tag{2.7}$$

Conversely, the conservation variables at the sub-time levels can be determined from the Fourier coefficients by the inverse discrete Fourier transform given by

$$\tilde{\boldsymbol{U}} = \boldsymbol{E}\boldsymbol{U}^{*}. \tag{2.8}$$

Note that $\boldsymbol{E}$ and $\boldsymbol{E}^{-1}$ are square matrices as the number of sub-time levels is equal to the number of Fourier coefficients. As an example $\boldsymbol{E}$ and $\boldsymbol{E}^{-1}$ matrices can be written as

$$\boldsymbol{E} = \frac{2}{2N+1}\begin{bmatrix} 1/2 & 1/2 & 1/2 & ... & 1/2 \\ \cos\omega t_1 & \cos\omega t_2 & \cos\omega t_3 & ... & \cos\omega t_{2N+1} \\ \vdots & \vdots & \vdots & & \vdots \\ \cos N\omega t_1 & \cos N\omega t_2 & \cos N\omega t_3 & ... & \cos N\omega t_{2N+1} \\ \sin\omega t_1 & \sin\omega t_2 & \sin\omega t_3 & ... & \sin\omega t_{2N+1} \\ \vdots & \vdots & \vdots & & \vdots \\ \sin N\omega t_1 & \sin N\omega t_2 & \sin N\omega t_3 & ... & \sin N\omega t_{2N+1} \end{bmatrix},$$

$$\boldsymbol{E}^{-1} = \begin{bmatrix} 1 & \cos\omega t_1 & ... & \cos N\omega t_1 & \sin\omega t_1 & ... & \sin N\omega t_1 \\ 1 & \cos\omega t_2 & ... & \cos N\omega t_2 & \sin\omega t_2 & ... & \sin N\omega t_2 \\ 1 & \cos\omega t_3 & ... & \cos N\omega t_3 & \sin\omega t_3 & ... & \sin N\omega t_3 \\ \vdots & \vdots & & \vdots & \vdots & & \vdots \\ 1 & \cos\omega t_{2N+1} & ... & \cos N\omega t_{2N+1} & \sin\omega t_{2N+1} & ... & \sin N\omega t_{2N+1} \end{bmatrix}.$$

To simplify the derivation of HDHB, one rewrites Eq. (2.1) in a general form as

$$\frac{\mathrm{d}\boldsymbol{U}}{\mathrm{d}t} + \boldsymbol{R} = 0. \tag{2.9}$$

The general form of unsteady equations can be written for all sub-time levels simultaneously, so that

$$\omega \boldsymbol{D} \boldsymbol{U}^* + \boldsymbol{R}^* = 0, \tag{2.10}$$

where $\boldsymbol{R}^*$ is the residual evaluated at $\boldsymbol{U}^*$. It is noted that the $2N+1$ sets of conservation equations are coupled only through the time derivative term, which is approximated by the pseudo-spectral operator, $\omega \boldsymbol{D} = \frac{d\boldsymbol{E}^{-1}}{dt}\boldsymbol{E}$. In order to solve the harmonic balance equations, a "pseudo-time" term is introduced so that the equations could be drived rapidly to a steady state condition with a traditional CFD scheme. Thus, Eq. (2.10) becomes

$$\frac{\partial \boldsymbol{U}^*}{\partial \tau} + \omega \boldsymbol{D} \boldsymbol{U}^* + \boldsymbol{R}^* = 0, \tag{2.11}$$

where τ is a fictitious or pseudo time, used only to march Eq. (2.11) to a steady state, driving the pseudo-time term to zero. The pseudo-time harmonic balance equations are similar in form to the original time domain RANS Eq. (2.1), with an additional source term, $\omega \boldsymbol{D} \boldsymbol{U}^*$. Thus, existing well-developed steady CFD techniques may be employed to solve the nonlinear harmonic balance equations efficiently, with comparable number of iterations required.

2.4 Boundary Conditions

In this work, we use the following boundary conditions for cascade flow computations: 1) wall boundary, 2) periodic boundary, 3) far-field boundary. For wall boundary, zero normal velocity boundary is imposed for inviscid computations and no slip boundary is imposed for viscous computations. The control volume for the wall surface grid is formed by two nearest cells near the wall. Governing equations are solved on the wall surface grids for better convergence compared to extrapolation of the conservation variables from the interior grid nodes to the wall nodes. One of the advantages of frequency domain techniques compared to the time-domain method is that the computation domain can be reduced to a single blade passage by using complex periodic boundary conditions. To apply this boundary condition, the solutions $\boldsymbol{U}^*$ located at the periodic boundary are transformed into Fourier coefficients. Inspection of Eq. (2.6) reveals that the appropriate boundary conditions, written in the cylindrical coordinate, are given by

$$\begin{aligned} \boldsymbol{A}_k(x, r, \theta + \theta_G) &= \boldsymbol{A}_k(x, r, \theta) \cdot \cos(n\theta_G) + \boldsymbol{B}_k(x, r, \theta) \cdot \sin(n\theta_G), \\ \boldsymbol{B}_k(x, r, \theta + \theta_G) &= -\boldsymbol{A}_k(x, r, \theta) \cdot \sin(n\theta_G) + \boldsymbol{B}_k(x, r, \theta) \cdot \cos(n\theta_G). \end{aligned} \tag{2.12}$$

Quasi three-dimensional non-reflecting far-field boundary conditions[75, 76] are applied at each spanwise location in the frequency domain to eliminate spurious reflections. For subsonic flows, total pressure, total temperature and flow angles are specified at the upstream, and static pressure is specified downstream. These

conditions are applied to the mean (steady) part of the flow. Non-reflecting conditions are applied to the higher Fourier modes to eliminate spurious incoming waves.

As discussed in the introduction, the frequency, ω, in some problems is unknown a *priori*. For such problems, the frequency can be treated as part of the solution. When an incorrect frequency is specified in a HDHB solver, the residual would not converge to a machine accuracy. The phase change of the solution per iteration varies almost linearly with frequency. Note that only the exact frequency value leads to zero phase angle. Based on this observation, Spiker et al.[16] suggested the following procedure. An initial guess for the frequency is made, and the solution is run until the residual reaches a limit cycle. One then computes the change in the phase angle of the first harmonic of the lift (or some other global quantity) per iteration. This process is repeated at a few nearby frequencies. Then, using this data to define a line, one interpolates or extrapolates to find the frequency that produces zero phase shift per iteration. In another approach, McMullen and Jameson[11] proposed a gradient-based method to estimate the frequency. At each iteration, the frequency is modified so as to by minimize the residual of the solver. Later on, Gopinath and Jameson[15] extended the idea to the time spectral method, which is essentially identical to the HDHB method. Gopinath's approach is a first-order optimization, also known as the steepest descent method. In this work, we employ a similar method. Rewriting the change (at each HB iteration) for each sub-time level and computational node in the domain as

$$\delta \boldsymbol{U}^* = \mathcal{V}\omega \boldsymbol{D}\boldsymbol{U}^* + \boldsymbol{R}(\boldsymbol{U}^*) \tag{2.13}$$

allows one to define a total residual by adding the squares of the changes in conserved variables resulting in

$$\boldsymbol{I} = \frac{1}{2 \times N_{EQU} \times (2N_{HB}+1) \times N_{GRID}} \sum_{i=1}^{N_{EQU}} \sum_{j=1}^{2N_{HB}+1} \sum_{k=1}^{N_{GRID}} (\delta \boldsymbol{U})_{ijk}^2, \tag{2.14}$$

where $2N_{HB}+1$ is the number of sub-time levels retained in the model, and N_{GRID} is the total number of grid nodes in the computational domain. To estimate the "correct" frequency, which will allow the residuals to converge to machine accuracy, we set the first derivative of $\boldsymbol{I}$ with respect to ω to zero (to minimize the value of $\boldsymbol{I}$ at each iteration) and determine the updated value of ω using a Newton-like technique, i.e.,

$$\omega^{new} = \omega^{old} - \frac{\boldsymbol{I}'}{\boldsymbol{I}''}. \tag{2.15}$$

This modification is expected to have a slightly faster convergence rate than the GBVTP method. Apparently, the total residual, $\boldsymbol{I}$, is a function of conserved variables as well as the excitation frequency ω. In practice, however, the dependence of $\mathbf{U}^*$ on ω is ignored because it is impossible to evaluate it analytically, and numerical evaluation by a finite difference approach is computational costly.

In Hall's first paper[10], a Fourier stability analysis on the HDHB scheme was performed to find that such a scheme is unconditionally unstable for nonzero frequencies. However, the instabilities associated with long wavelengths may be stabilized by the finite far-field boundaries. Their numerical solutions showed

the HDHB solver converged with upto five harmonics for a modern high-pressure compressor. Later on, when he and his colleagues applied the method to model laminar vortex shedding over a circular cylinder, and they reported stability problems[77]. In that paper, the solver with more than three harmonics diverged for a large domain of grid (compared to a turbomachinery grid). They designed a filter mechanism to zero out higher harmonics in the far-field regions so that converged solutions with seven harmonics could be obtained. Gentilli[78] investigated the stability condition of a second-order upwind scheme coupled with a fourth-order Runge-Kutta time stepping. This scheme is conditionally stable (on an infinite domain) with a growth factor that depends on both the CFL number and the grid reduced frequency, a non-dimensional parameter that depends on the grid size, characteristic wave speed, and the highest frequency retained in the harmonic balance analysis. It was found that as the grid reduced frequency is increased the CFL limit decreases monotonically. Hall et al.[79] illustrated that a form of Burgers' equation is always unstable in the time-spectral version of the harmonic balance equations. Hall claimed in the paper that the HDHB method and its predecessor, time-linearised method, are both unconditionally unstable for an infinite domain. However, the boundary of a finite computational domain tends to stabilize the solver. When we developed an our turbomachinery CFD solver, no stability problems were encountered. However, for an external code we used to analyze unsteady flow about a circular cylinder, instability issues were encountered. To circumvent these stability problems, a modification to the timestep proposed by van der Weide et al.[23], has

been implemented into our solver,

$$\Delta t_N = \frac{CFL\mathcal{V}}{||\lambda|| + N\omega\mathcal{V}}, \tag{2.16}$$

where $\mathcal{V}$ is the volume of a cell, $||\lambda||$ is the spectral radius of the flux Jacobian, N is the number of harmonics retained in the solver and ω is the excitation frequency. The additional term, $N\omega\mathcal{V}$, appears to stabilize the code.

2.5 Temporal Spectral Viscosity

Spectral viscosity has a long history in the pseudo-spectral method, in which the Fourier transformation is applied for the spatial discretisation. In 1989, Tadmor[80] first proposed a second-order spectral viscosity and also demonstrated that the spectral viscosity prevents oscillations and the convergence of physical correct solution to the inviscid Burgers' equation. Later on, he extended the method to high-order viscosity, also known as super-viscosity method[81]. Spectral viscosity has been widely employed to stabilize the spectral method and the spectral element method for problems with large gradients[82, 83].

As discussed earlier, the high-dimensional harmonic balance method may suffer from aliasing errors compared to the classical harmonic balance method. McMullen and Jameson[12] have applied the spectral viscosity to the coarse grid of the multigrid NLFD solver to accelerate the convergence. In this paper, a second-order spectral

viscosity is applied in time to damp the high frequency modes which are contaminated by aliasing errors so as to stabilize Duffiing equation HDHB solver. The amount of viscosity should be carefully controlled to keep the temporal spectral accuracy. In this paper, we add a second-order temporal spectral viscosity term to Eq. (2.11) so that

$$\frac{\partial \boldsymbol{U}^*}{\partial \tau} + \omega \boldsymbol{D} \boldsymbol{U}^* + \boldsymbol{R}^* = \omega^2 \boldsymbol{D}_2 \boldsymbol{U}^*, \tag{2.17}$$

where

$$\omega^2 \boldsymbol{D}_2 = \epsilon_N \frac{\mathrm{d}^2 \boldsymbol{E}^{-1}}{\mathrm{d}t^2} \rho_n \boldsymbol{E},$$

the viscosity coefficient $\epsilon_N \sim \frac{1}{N} \sim \mathcal{O}(\Delta t)$, ρ_n is a Fourier cut-off function

$$\rho_n = \begin{cases} 0, \text{if} \;\; n \leq m \\ \\ 1, \text{if} \;\; n > m \end{cases},$$

$m \sim N^{\frac{1}{2}}$ is the cut-off harmonic number, determining the inviscid spectrum. The spectral viscosity method can be regarded as a compromise between a stable first oder accuracy algorithm ($m = 0$) and a spectral accuracy algorithm ($m = N$), which may exhibit instability for strong nonlinear cases. The spectral viscosity coefficient is chosen to be $\epsilon_N = \frac{1}{N}$ and cut-off harmonic $m = 1$ in the paper, unless it is explicitly specified.

When applying the pseudospectral method to hyperbolic problems, a convergence stability is a concern due to the lack of inherent dissipation mechanism. A classical way to stabilize a central difference discretization of a hyperbolic PDE can be accomplished by adding artificial dissipation.

$$\frac{\partial u}{\partial t} + \frac{\partial f(u)}{\partial x} = \epsilon(-1)^{p+1}\frac{\partial^{2p} u}{\partial x^{2p}} \tag{2.18}$$

For example, a blend of a second and fourth order dissipation term is added in the JST scheme[71].

To show the temporal spectral viscosity is actually a dissipation term, one rewrites a hyperbolic equation with the stabilized TSV term as,

$$\frac{\partial u}{\partial t} + \frac{\partial f(u)}{\partial x} = \epsilon\frac{\partial^2 u}{\partial t^2} \tag{2.19}$$

The equation can be linearized as

$$\frac{\partial u}{\partial t} + a\frac{\partial u}{\partial x} = \epsilon\frac{\partial^2 u}{\partial t^2} \tag{2.20}$$

Taking a derivative of the linearized equation with respect to t and only retaining the leading term yields to

$$\frac{\partial^2 u}{\partial t^2} \sim -a\frac{\partial^2 u}{\partial x \partial t} \tag{2.21}$$

Taking a derivative of the linearized equation with respect to x and then multipling by a yields

$$a\frac{\partial^2 u}{\partial x \partial t} \sim -a^2 \frac{\partial^2 u}{\partial x^2} \tag{2.22}$$

Finally, one obtains

$$\epsilon\frac{\partial^2 u}{\partial t^2} \sim \epsilon a^2 \frac{\partial^2 u}{\partial x^2} \tag{2.23}$$

Thus, the TSV term can be regarded as a second-order artificial dissipation term for hyperbolic equations.

2.6 Another Point of View of The Pseudospectral Operator

As discussed before, the spectral operator is a central difference matrix. For example, $N = 3$, the $\boldsymbol{D}$ matrix is given by

$$\boldsymbol{D} = \begin{bmatrix} 0.0000 & 1.1524 & -0.6395 & 0.5129 & -0.5129 & 0.6395 & -1.1524 \\ -1.1524 & 0.0000 & 1.1524 & -0.6395 & 0.5129 & -0.5129 & 0.6395 \\ 0.6395 & -1.1524 & 0.0000 & 1.1524 & -0.6395 & 0.5129 & -0.5129 \\ -0.5129 & 0.6395 & -1.1524 & 0.0000 & 1.1524 & -0.6395 & 0.5129 \\ 0.5129 & -0.5129 & 0.6395 & -1.1524 & -0.0000 & 1.1524 & -0.6395 \\ -0.6395 & 0.5129 & -0.5129 & 0.6395 & -1.1524 & 0.0000 & 1.1524 \\ 1.1524 & -0.6395 & 0.5129 & -0.5129 & 0.6395 & -1.1524 & 0.0000 \end{bmatrix}.$$

In a similar way, a second-order backward difference formula and a central difference formula for seven sub-time levels with an enforced periodic condition can be written as

$$\boldsymbol{D}_{bdf} = \begin{bmatrix} 1.5 & 0 & 0 & 0 & 0 & 0.5 & -2 \\ -2 & 1.5 & 0 & 0 & 0 & 0 & 0.5 \\ 0.5 & -2 & 1.5 & 0 & 0 & 0 & 0 \\ 0 & 0.5 & -2 & 1.5 & 0 & 0 & 0 \\ 0 & 0 & 0.5 & -2 & 1.5 & 0 & 0 \\ 0 & 0 & 0 & 0.5 & -2 & 1.5 & 0 \\ 0 & 0 & 0 & 0 & 0.5 & -2 & 1.5 \end{bmatrix},$$

and

$$\boldsymbol{D}_{cdf} = \begin{bmatrix} 0 & 0.5 & 0 & 0 & 0 & 0 & -0.5 \\ -0.5 & 0 & 0.5 & 0 & 0 & 0 & 0 \\ 0 & -0.5 & 0 & 0.5 & 0 & 0 & 0 \\ 0 & 0 & -0.5 & 0 & 0.5 & 0 & 0 \\ 0 & 0 & 0 & -0.5 & 0 & 0.5 & 0 \\ 0 & 0 & 0 & 0 & -0.5 & 0 & 0.5 \\ 0.5 & 0 & 0 & 0 & 0 & -0.5 & 0 \end{bmatrix}.$$

The BDF temporal discretization is widely used in time-accurate solvers. Higher-order center difference operators can be derived accordingly. It is important to note that the pseudo-spectral operator can be obtained as the limit of a high order central

difference method with an enforced periodic condition[84]. The second-order central-difference in time is usually referred to as the Leapfrog scheme, in which the even and odd time steps may be decoupled. To circumvent this potential problem and to stabilize the leapfrog scheme, Robert[85] and Asselin[86] suggested to add a second-order time derivative to the original scheme. This modification is also referred as the Robert-Asselin filter, which is designed to damp high temporal frequencies. The TSV method and the Robert-Asselin filter are similar in that both of them add an explicit second-order time derivative term to stabilize central difference temporal discretisations. However, the TSV is implemented in the frequency domain rather than the time-domain.

2.7 Parallelization with OpenMP

As stated before, all sub-time level solutions are only coupled with each other by the pseudo-spectral terms and non-reflecting boundary conditions. This property makes it suitable for parallelization with OpenMP. OpenMP is multi-threaded, shared memory parallelism. The harmonic balance code is parallelized by work-sharing constructs, in which each thread works on its own sub-time level solution. Therefore, it is desirable to use the same number of processors as the number of sub-time levels to achieve the best performance. Generally, the computational time for one harmonic with three processors can be halved compared to a sequential code.

Chapter 3

Discrete Adjoint Method Using an Automatic Differentiation Tool

The objective of the adjoint method is to compute the sensitivities of objective functions with respect to a large amount of design variables efficiently. In the turbomachinery shape optimization field, the objective functions can be the total pressure loss or drag coefficient on the blades, and the design variables are those which parameterize the blade geometry.

One can define the objective function to be differentiated as

$$\boldsymbol{I} = \boldsymbol{I}(\boldsymbol{x}, \boldsymbol{U}(\boldsymbol{x})), \tag{3.1}$$

where $\boldsymbol{x}$ is the vector of design variables and $\boldsymbol{U}$ is the state variable of the flow field. Keeping the chain rule in mind, one can write the total derivative of the function $\boldsymbol{I}$

with respect to $\boldsymbol{x}$ as

$$\frac{\mathrm{d}\boldsymbol{I}}{\mathrm{d}\boldsymbol{x}} = \frac{\partial \boldsymbol{I}}{\partial \boldsymbol{x}} + \frac{\partial \boldsymbol{I}}{\partial \boldsymbol{U}} \frac{\mathrm{d}\boldsymbol{U}}{\mathrm{d}\boldsymbol{x}}. \tag{3.2}$$

It is worth noting the difference between the total and partial derivatives in the above equations. The partial derivatives can be determined easily either by an analytical method or a finite difference method. However, the total derivative requires solving the governing equations for each component of $\boldsymbol{x}$. Therefore, it is desirable to avoid an explicit computation of $\frac{\mathrm{d}\boldsymbol{U}}{\mathrm{d}\boldsymbol{x}}$ in order to save computational cost using an adjoint method. One can rewrite the governing equations including the boundary conditions as

$$\boldsymbol{R}(\boldsymbol{x}, \boldsymbol{U}(\boldsymbol{x})) = 0. \tag{3.3}$$

Since the governing equations and the associated boundary conditions have to be satisfied no matter what $\boldsymbol{x}$ is given, the total derivative of the residual with respect to the design variables must be zero, that is

$$\frac{\mathrm{d}\boldsymbol{U}}{\mathrm{d}\boldsymbol{x}} = \frac{\partial \boldsymbol{R}}{\partial \boldsymbol{x}} + \frac{\partial \boldsymbol{R}}{\partial \boldsymbol{U}} \frac{\mathrm{d}\boldsymbol{U}}{\mathrm{d}\boldsymbol{x}} = 0. \tag{3.4}$$

The system of Eq.(3.4) can be rearranged to isolate $\frac{\mathrm{d}\boldsymbol{U}}{\mathrm{d}\boldsymbol{x}}$ as follows,

$$\frac{\mathrm{d}\boldsymbol{U}}{\mathrm{d}\boldsymbol{x}} = -\left[\frac{\partial \boldsymbol{R}}{\partial \boldsymbol{U}}\right]^{-1} \frac{\partial \boldsymbol{R}}{\partial \boldsymbol{x}}. \tag{3.5}$$

The Eq.(3.5) can be substituted into Eq.(3.2), leading to

$$\frac{\mathrm{d}\boldsymbol{I}}{\mathrm{d}\boldsymbol{x}} = \frac{\partial \boldsymbol{I}}{\partial \boldsymbol{x}} - \frac{\partial \boldsymbol{I}}{\partial \boldsymbol{U}} \left[\frac{\partial \boldsymbol{R}}{\partial \boldsymbol{U}}\right]^{-1} \frac{\partial \boldsymbol{R}}{\partial \boldsymbol{x}}. \tag{3.6}$$

At this point, one has two approaches to solve the equations. In the direct method, one first solves the linear system with the last two terms, namely Eq.(3.4), for N_x times (N_x is the number of design variables). As an alternative, one can choose to solve the linear system with the first two terms as,

$$\psi^T = -\frac{\partial \boldsymbol{I}}{\partial \boldsymbol{U}} \left[\frac{\partial \boldsymbol{R}}{\partial \boldsymbol{U}}\right]^{-1}. \tag{3.7}$$

This approach is referred to as the adjoint method, which needs to be solved N_l times (N_l is the number of objective functions),

$$\left[\frac{\partial \boldsymbol{R}}{\partial \boldsymbol{U}}\right]^T \psi = -\left[\frac{\partial \boldsymbol{I}}{\partial \boldsymbol{U}}\right]^T. \tag{3.8}$$

With the ψ satisfying the adjoint equation, Eq.(3.8), one finds the sensitivity as

$$\frac{\mathrm{d}\boldsymbol{I}}{\mathrm{d}\boldsymbol{x}} = \frac{\partial \boldsymbol{I}}{\partial \boldsymbol{x}} + \psi^T \left[\frac{\partial \boldsymbol{R}}{\partial \boldsymbol{x}}\right]. \tag{3.9}$$

Note that the linear systems in both the direct method and the adjoint method have the same size. In the case of aerodynamic shape optimization, there are typically a few object functions, such as C_D or C_L. However, there can be on the order of

hundreds or thousands of design variables parameterizing the shape. Thus, the adjoint method benefits substantially in terms of the computational cost for aerodynamic shape optimization.

As mentioned earlier, there are two approaches to solve adjoint problems. Compared to continuous adjoint, it is much easier to develop the discrete adjoint method with the help of an automatic differentiation (AD) tool. For instance, it has taken two years to develop and validate the two and three-dimensional CFD solvers used in this work. It could be expected to take an even longer time to develop a continuous adjoint solver. Aside from the adjoint viscous terms being very complex, we do not know much about the gradient of the flow field. Therefore, it is rather difficult to validate an adjoint solver. Instead, it takes a relatively short time to differentiate an entire CFD code using an AD tool. However, the generated adjoint code can be very inefficient, with a prohibitively high memory requirement. Therefore, it is necessary to come up with an approach to balance the code implementation complexity and the code run-time efficiency. Mader et al.[54] proposed a hybrid method, they called "Adjoint", in which the residual subroutine and the object subroutine are differentiated by an AD tool to obtain the four partial derivatives in Eq.(3.8) and Eq.(3.9). Then they solved the linear system of equations with the GMRES[55] method in the well-tuned linear algebra package PETSc[56]. In that methodology, it is necessary to rewrite the residual subroutine in the format of nested loop over each single cell residual and then differentiate the single cell residual.

However, it is not straight-forward to implement the "ADjoint" method in our CFD solver because of the non-reflecting far-field boundary condition used in our solver.

Alternatively, there is a third approach to generate an efficient adjoint solver by considering that the steady and harmonic balance solutions are independent of the pseudo-time stepping. In the reverse mode, the intermediate variables for each iteration are recorded in memory, then they are pushed back reversely for the adjoint iteration. Figure 3.1 and Figure 3.2 show the flow chart of a CFD solver and unmodified AD code generated by Tapenade, respectively. As it can be seen, the memory demand can easily grow beyond what is available if the adjoint code is used directly without modification. The unmodified AD code is actually unsteady adjoint to the original code. For steady state and harmonic balance computations, however, the time-stepping is actually performed in pseudo-time, which means that the final solutions should be independent of the pseudo-time integration. To take advantage of this, it is reasonable to assume that one feeds the CFD solver with a converged solution so that the intermediate variables do not change from one iteration to another. With this assumption, one can take out the most of PUSH and POP instructions from the original AD code without changing the adjoint solutions. This strategy saves both memory usage and code development efforts substantially. The flowchart of the modified flowchart is illustrated in Figure 3.3. It should be noted that this strategy can be implemented automatically in the commercial AD tool, TAF/TAMC[87]. On the other hand, it would be impossible to apply this strategy to an time-accurate

solver. One needs to resolve the memory issues using a checkpoint. etc. It is the great advantage of using HB solvers for adjoint techniques.

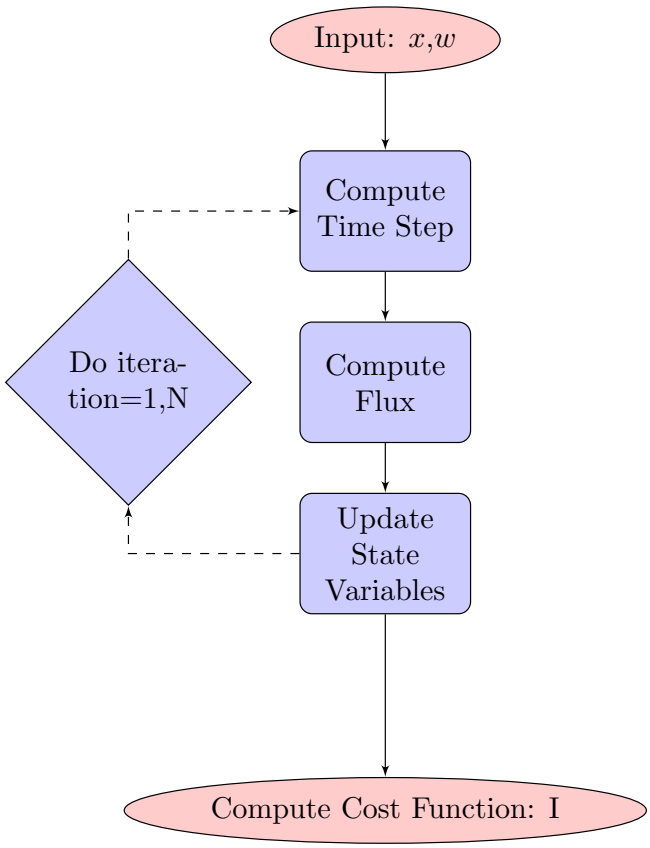


Figure 3.1: Flow chart of a CFD solver.

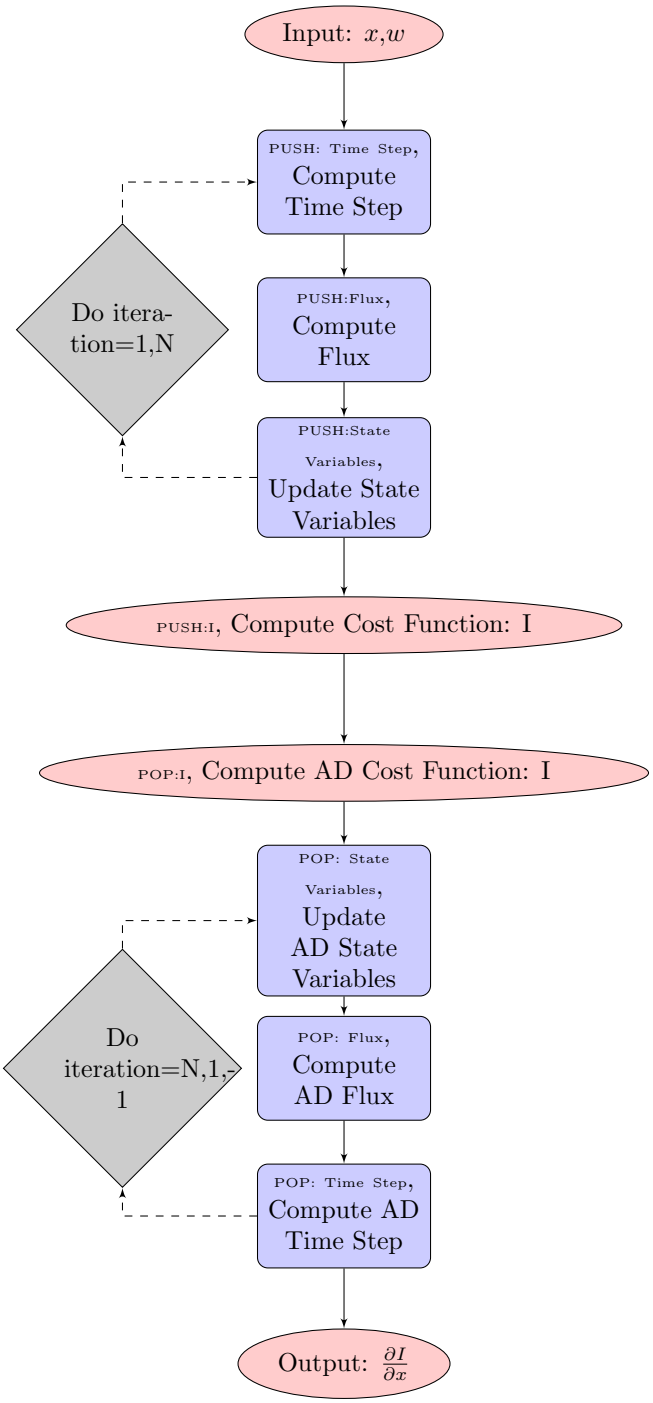


Figure 3.2: Flow chart of an original adjoint solver.

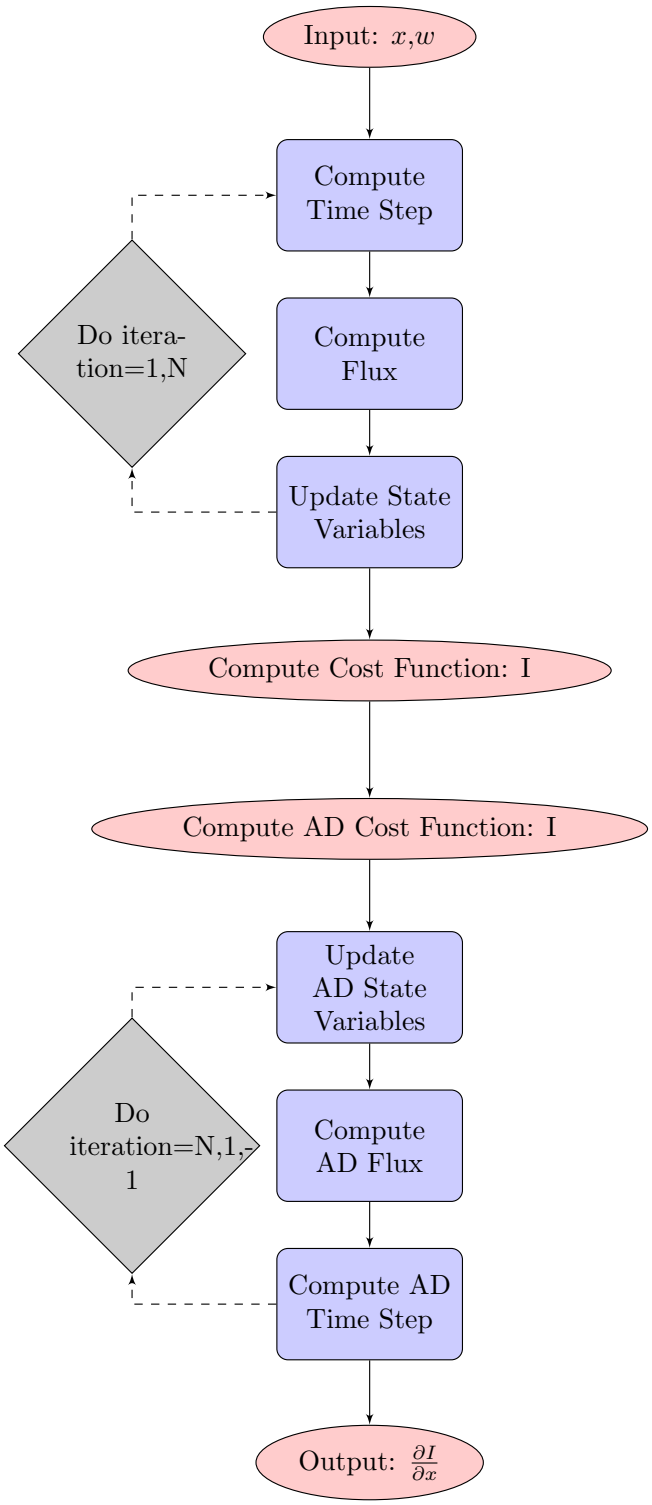


Figure 3.3: Flow chart of a modified adjoint solver.

Chapter 4

Aerodynamic Shape Optimization Framework

The design variables, which parameterize the shape, play an important role for effective aerodynamic shape optimization. The desirable design variables ought to have the following three characteristics: 1. Forming a complete design space. 2. Smooth parameterized shape. 3. The orthogonality of the design variables. In an optimization problem, the optimized point may be excluded within an incomplete design space. In an inverse design problem, the target shape may not be parameterized by an incomplete design space. A non-smooth shape usually causes a CFD convergence issues. Therefore, the design variables should be capable of producing a smooth aerodynamic shape in the optimization process. The orthogonal design variables are expected to have a fast optimization convergence rate. A direct use of the discrete blade x, y, z coordinates as the design variables is generally not preferred,

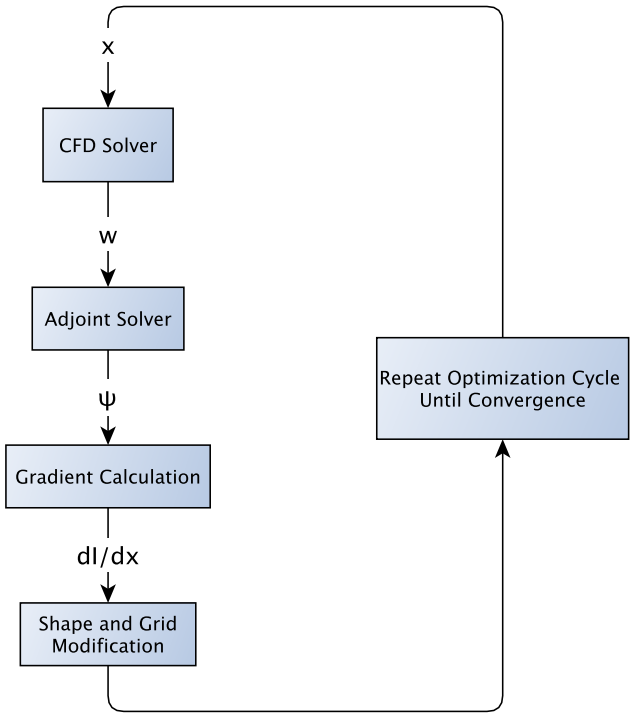


Figure 4.1: Flow chart for optimization process.

because the blade shape could become non-smooth during the optimization process. Smoothing the gradients or adding a penalty function to control the smoothness is required in this approach. Alternatively, one may choose a smooth function to perturb the original blade shape, such as B-splines functions or Hicks-Henne bump functions[88].

After obtaining the sensitivities of the object function with respect to the design variables, an appropriate gradient based optimization must be employed to perturb the blade shape and the grid accordingly. Shown in Figure 4.1 is a typical flow chart for the complete optimization process.

In this work, the limited-memory BFGS algorithm[89] and the steepest descent are chosen for shape optimization. Before discussing the L-BFGS algorithm, it is useful to present the gradient descent method, the smoothed gradient descent method and the Newton's method used for optimization. With the notation of a cost function $\boldsymbol{I}$ and its derivatives $\nabla \boldsymbol{I}$, starting with an initial guess $\mathbf{x_0}$ and its gradient $\nabla \boldsymbol{I}(\mathbf{x_0})$, the gradient descent method can be written as

$$\mathbf{x_{n+1}} = \mathbf{x_n} - a_n \nabla \boldsymbol{I}(\mathbf{x_0}), \tag{4.1}$$

where the step size, a_n, is a small number, satisfying the Wolfes conditions[90, 91].

To preserve the smoothness of the profile with mesh points as design variables, Jameson and Reuther[92] proposed to smooth the gradient implicitly as

$$\bar{\nabla} \boldsymbol{I} - \frac{\partial}{\partial \xi} \epsilon \frac{\partial}{\partial \xi} \bar{\nabla} \boldsymbol{I} = \nabla \boldsymbol{I}, \tag{4.2}$$

where ϵ is the smoothing parameter and $\bar{\nabla} \boldsymbol{I}$ is the smoothed gradient. High frequency contents are eliminated by the smoothing procedure.

In the Newton's method, the cost function is approximated by a quadratic model at current point $\mathbf{x}_n$ as

$$\boldsymbol{I}(\mathbf{x}) = \boldsymbol{I}(\mathbf{x}_n) + \mathbf{p}_n^T \nabla \boldsymbol{I}(\mathbf{x_n}) + \frac{1}{2} \mathbf{p}_n^T B(\mathbf{x_n}) \mathbf{p}_n, \tag{4.3}$$

where $\mathbf{p}_n = \mathbf{x} - \mathbf{x}_n$ and $B(\mathbf{x}_n)$ is the Hessian matrix. Taking the first derivate with respect to $\mathbf{x}$, we get

$$\nabla \boldsymbol{I}(\mathbf{x}) = \nabla \boldsymbol{I}(\mathbf{x}_n) + B(\mathbf{x}_n)\mathbf{p}_n. \tag{4.4}$$

The cost function is minimized when $\nabla \boldsymbol{I}(\mathbf{x})$ vanishes, that's

$$\mathbf{p}_n = -B(\mathbf{x}_n)^{-1}\nabla \boldsymbol{I}(\mathbf{x}_n). \tag{4.5}$$

The next point is found by a line search given by

$$\mathbf{x}_{n+1} = \mathbf{x}_n + a_n\mathbf{p}_n. \tag{4.6}$$

In quasi-Newton methods, such as the DFP method or the BFGS method, the $B(\mathbf{x}_n)$ matrix is never computed exactly, but is approximated by the changes of the gradients[36]. To determine the approximate Hessian matrix, it is natural to impose that the gradient expression (Eq. 4.3) matches at least two points $\mathbf{x}_n$ and $\mathbf{x}_{n+1}$. Since the condition is automatically satisfied at $\mathbf{x}_n$, it is imposed the condition at the other point $\mathbf{x}_{n+1}$

$$B(\mathbf{x}_{n+1})a_n\mathbf{p}_n = \nabla \boldsymbol{I}(\mathbf{x}_{n+1}) - \nabla \boldsymbol{I}(\mathbf{x}_n). \tag{4.7}$$

To simplify the derivation, it is helpful to define

$$\mathbf{s}_n = \mathbf{x}_{n+1} - \mathbf{x}_n = a_n\mathbf{p}_n, \mathbf{y}_n = \nabla \boldsymbol{I}(\mathbf{x}_{n+1}) - \nabla \boldsymbol{I}(\mathbf{x}_n), \tag{4.8}$$

so that Eq (4.7) becomes

$$B(\mathbf{x}_{n+1})\mathbf{s}_n = \mathbf{y}_n. \tag{4.9}$$

The condition is usually referred to as the secant equation. To determine a unique $B(\mathbf{x}_{n+1})$, the next $B(\mathbf{x}_{n+1})$ are require to be close to the previous $B(\mathbf{x}_n)$ in certain sense. In mathematical words, the problem is written as

$$min_B \|B - B_n\|, \text{ subject to } B = B^T, B\mathbf{s}_n = \mathbf{y}_n. \tag{4.10}$$

Different choices of norm lead to different quasi-Newton methods. A weighted Frobenius norm[93] $\|A\|_W = \|W^{\frac{1}{2}} A W^{\frac{1}{2}}\|$ yields the DFP algorithm. After obtaining the **B** matrix, one is required to solve a linear system of equations to update design variables. A simple change by imposing the secant equation on the inverse of $B(\mathbf{x}_n)$, namely $H_n = B_n^{-1}$, leads to a more efficient BFGS algorithm. The unique solution H_{n+1} is given by

$$H_{n+1} = (\mathbf{I} - \rho_n \mathbf{s}_n \mathbf{y}_n^T) H_n (\mathbf{I} - \rho_n \mathbf{y}_n \mathbf{s}_n^T) + \rho_n \mathbf{s_n} \mathbf{s_n^T}, \tag{4.11}$$

where $\rho_n = \frac{1}{\mathbf{y}_n^T \mathbf{s}_n}$. A matrix-vector multiplication computes the updates of the design variables.

Storing the approximated inverse Hessian, H_n, becomes prohibitively costly for large scale problems. To circumvent the problem, a variant limited-memory BFGS algorithm only stores a certain number (say, m) of pairs $\{\mathbf{s}_i, \mathbf{y}_i\}$ instead. The set

of vector pair $\{\mathbf{s}_i, \mathbf{y}_i\}$ for $i = n-m, ..., n-1$ is stored for the current iteration. After new iterations are carried out, the latest pair $\{\mathbf{s}_n, \mathbf{y}_n\}$ replaces the oldest pair $\{\mathbf{s}_{n-m}, \mathbf{y}_{n-m}\}$. The L-BFGS method is accomplished by "unrolling" the inverse Hessian update m times. Defining $\mathbf{V}_n = \mathbf{I} - \rho_n \mathbf{y}_n \mathbf{s}_n^T$, the L-BFGS can be written as

$$H_n = \mathbf{V}_{n-1}^T H_{n-1} \mathbf{V}_{n-1} + \mathbf{s}_{n-1} \rho_{n-1} \, \mathbf{s}_{n-1}^T. \tag{4.12}$$

Unrolling back one step leads to

$$H_n = \mathbf{V}_{n-1}^T \mathbf{V}_{n-2}^T H_{n-2} \mathbf{V}_{n-2} \mathbf{V}_{n-1} + \mathbf{V}_{n-1}^T \mathbf{s}_{n-2} \rho_{n-2} \mathbf{s}_{n-2}^T \mathbf{V}_{n-1} + \mathbf{s_{n-1}} \rho_{\mathbf{n-1}} \mathbf{s_{n-1}^T}. \tag{4.13}$$

Unrolling back m steps leads to

$$\begin{aligned} H_n = \; & (\mathbf{V}_{n-1}^T ... \mathbf{V}_{n-m}^T) H_{n-m} (\mathbf{V}_{n-m} ... \mathbf{V}_{n-1}) \\ & + (\mathbf{V}_{n-1}^T ... \mathbf{V}_{n-m+1}^T) \mathbf{s}_{n-m} \rho_{n-m} \mathbf{s}_{n-m}^T (\mathbf{V}_{n-m+1} ... \mathbf{V}_{n-1}) \\ & + (\mathbf{V}_{n-1}^T ... \mathbf{V}_{n-m+2}^T) \mathbf{s}_{n-m+1} \rho_{n-m+1} \mathbf{s}_{n-m+1}^T (\mathbf{V}_{n-m+2} ... \mathbf{V}_{n-1}) \\ & + ... \\ & + \mathbf{s_{n-1}} \rho_{\mathbf{n-1}} \mathbf{s_{n-1}^T}. \end{aligned} \tag{4.14}$$

The L-BFGS algorithm is more clearly illustrated in the following two-loop recursion pseudo-code:

$q \leftarrow \nabla \boldsymbol{I}_n$

for $i = n-1 \rightarrow n-m$ **do**

$\alpha_i \leftarrow \rho_i s_i^T q$

$q \leftarrow q - \alpha_i y_i$

end for

$r \leftarrow H_n^0 q$

for $i = n - m \rightarrow n - 1$ **do**

$\beta_i \leftarrow \rho_i y_i^T r$

$r \leftarrow r + s_i(\alpha_i - \beta)$

end for

Chapter 5

Results and Discussion

Numerical solutions are presented in this chapter. First, stable HDHB solutions, including two and three-dimensional, inviscid and viscous, steady and unsteady flow results, are presented in Section 5.1. Second, a Duffing oscillator and unsteady laminar flow around an oscillating circular cylinder at $Re = 500$ are numerically investigated with the addition of the temporal spectral viscosity in Section 5.2. Finally, aerodynamic shape optimization test cases are presented in Section 5.3.

5.1 HDHB Solutions

In this section, unsteady solutions are presented to validate the HDHB CFD solvers. It must be noted that no instability issues were encountered for the test cases presented in this section, which mainly includes cascade flow solutions.

5.1.1 Tenth Standard Configuration

Tenth Standard Configuration[94] is a two-dimensional inviscid compressor cascade with airfoils made of modified NACA 0006 profiles. The stagger angle of the airfoils is 45 deg and the gap to chord ratio is 1.0. Here, we consider two flow conditions: first one corresponding to a fully subsonic case, and the second one corresponding to a transonic case. For the results presented in this paper, we used the H-O-H type grid shown in Figure 5.1 with 193×33 nodes in the O-grid block. Although not presented here, a grid convergence study was performed and this grid resolution was found to be adequate.

Subsonic Case

In this section, we present harmonic balance computations for unsteady flow under subsonic flow conditions with an inlet Mach number of 0.7 and an inlet flow angle of 55 deg. Note that this case is also investigated and well documented in the work of other researchers [95]. First consider the steady flow field in the cascade. The steady surface pressure distributions are plotted in Figure 5.2 demonstrating a good agreement with the computational results from Petrie-Repar's time-linearized solver[95], which has been extensively validated against other independent data.

Next, it is assumed that the blades vibrate harmonically in pitch about their mid-chords with a full chord reduced frequency, $\omega^* = \omega c/U_{ref}$, of 0.5, where U_{ref} is the inlet flow velocity for a compressor and outlet flow velocity for a turbine. To eliminate any potential nonlinear effects and to be able to compare our harmonic

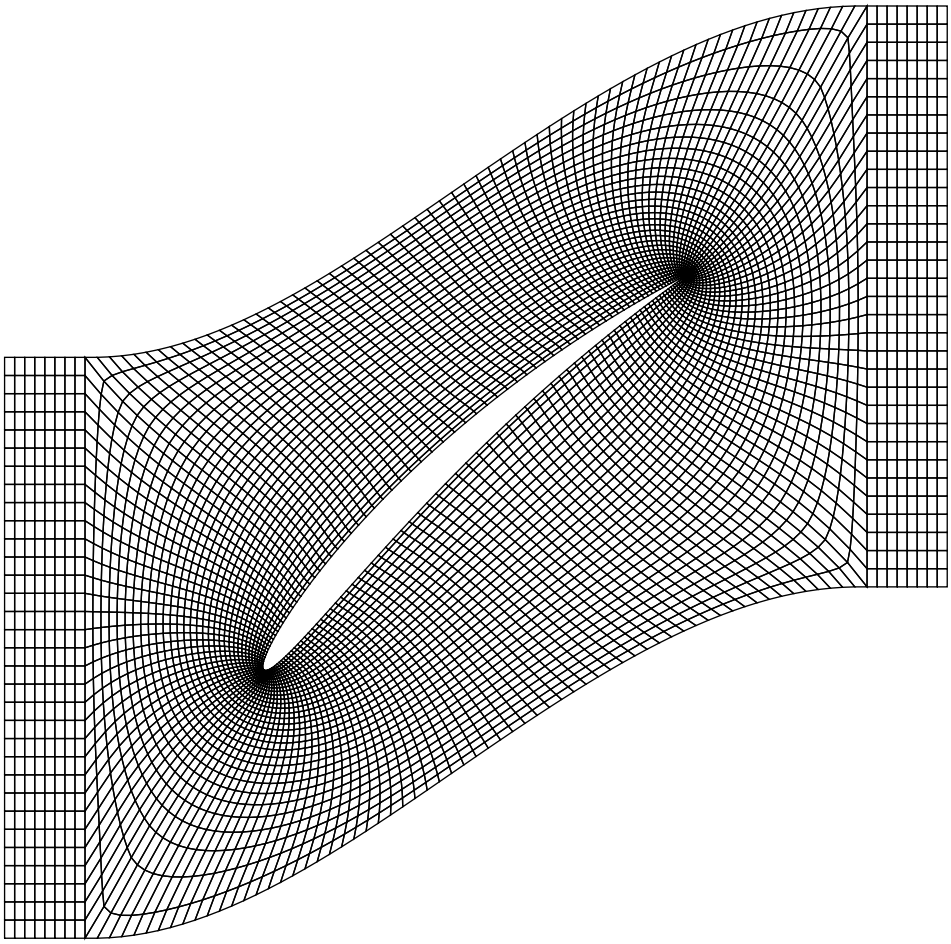


Figure 5.1: Computational grid for the Tenth Standard Configuration.

balance results to the time-linearized computational solutions of Petrie-Repar, blade pitching amplitude is taken to be very small (1×10^{-6} deg). The resulting unsteady flow is essentially linear because of the small amplitude of motion and the cascade is assumed to be vibrating at its first harmonic. Therefore, it should be adequate to retain only one harmonic (three sub-time level solutions) in these computations. Shown in Figure 5.3 are the imaginary part of the first harmonic of the surface pressure

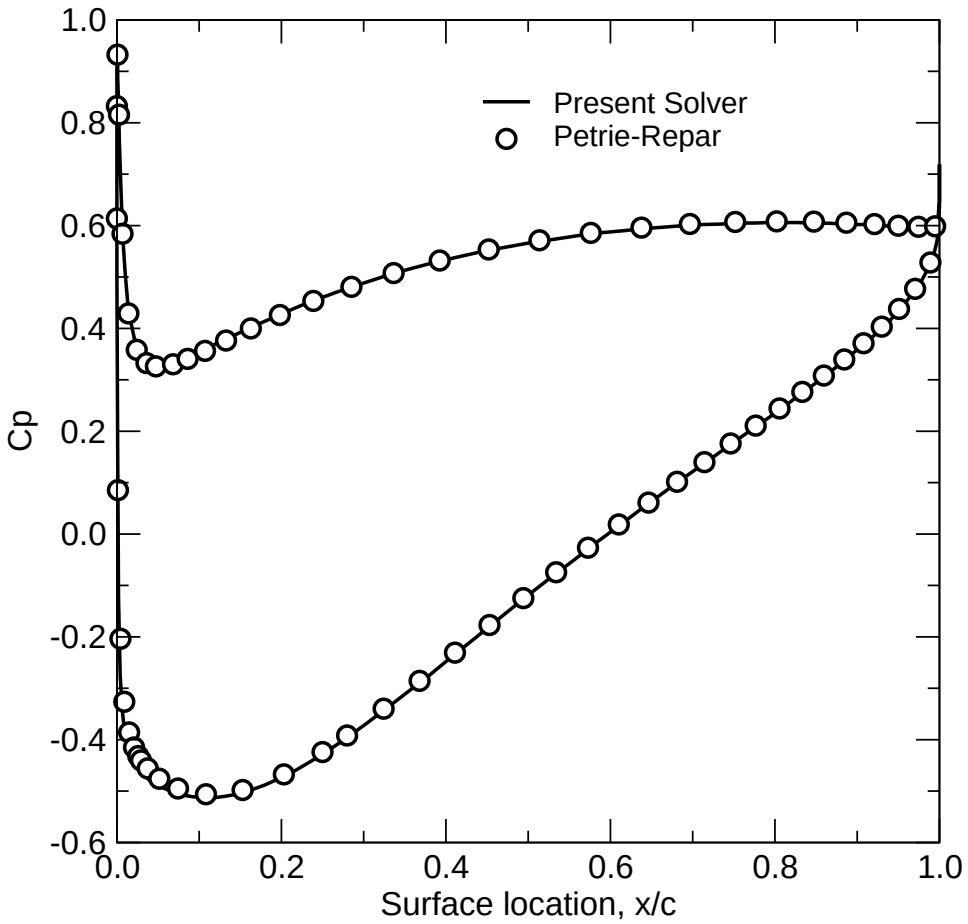


Figure 5.2: Pressure coefficient distribution for the Tenth Standard Configuration. Subsonic case.

coefficients scaled by the pitching amplitude. As can be seen, the results from our flow solver are in excellent agreement with those reported by Petrie-Repar[95].

Having presented unsteady surface pressure results from our computations, we now turn our attention to the issue of aeroelastic stability. Figure 5.4 shows the computed aerodynamic damping for different interblade phase angles. Note that the structural stability is determined by the sign of the aerodynamic damping with a positive value

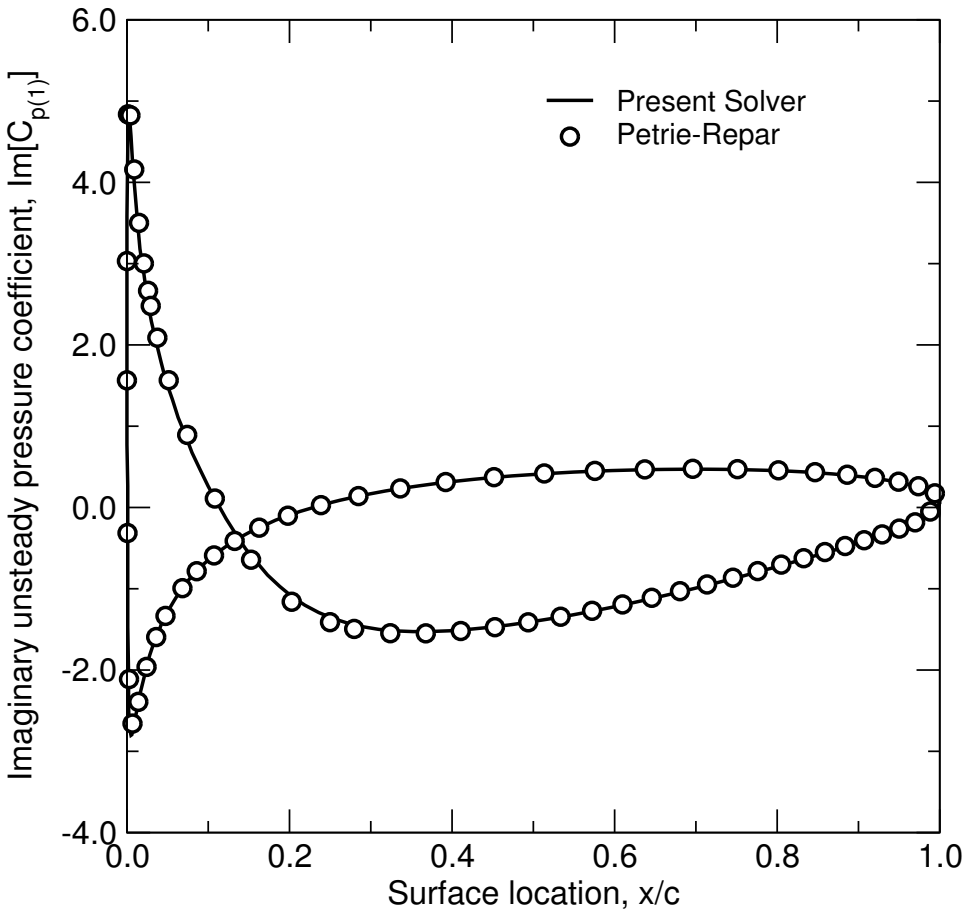


Figure 5.3: Imaginary unsteady pressure coefficient distribution for the Tenth Standard Configuration. Subsonic case, σ=0 deg, ω^*=0.5.

corresponding to a stable system. For this case, it is seen that the rotor is stable for all interblade phase angles and is in good agreement with Petrie-Repar's analysis.

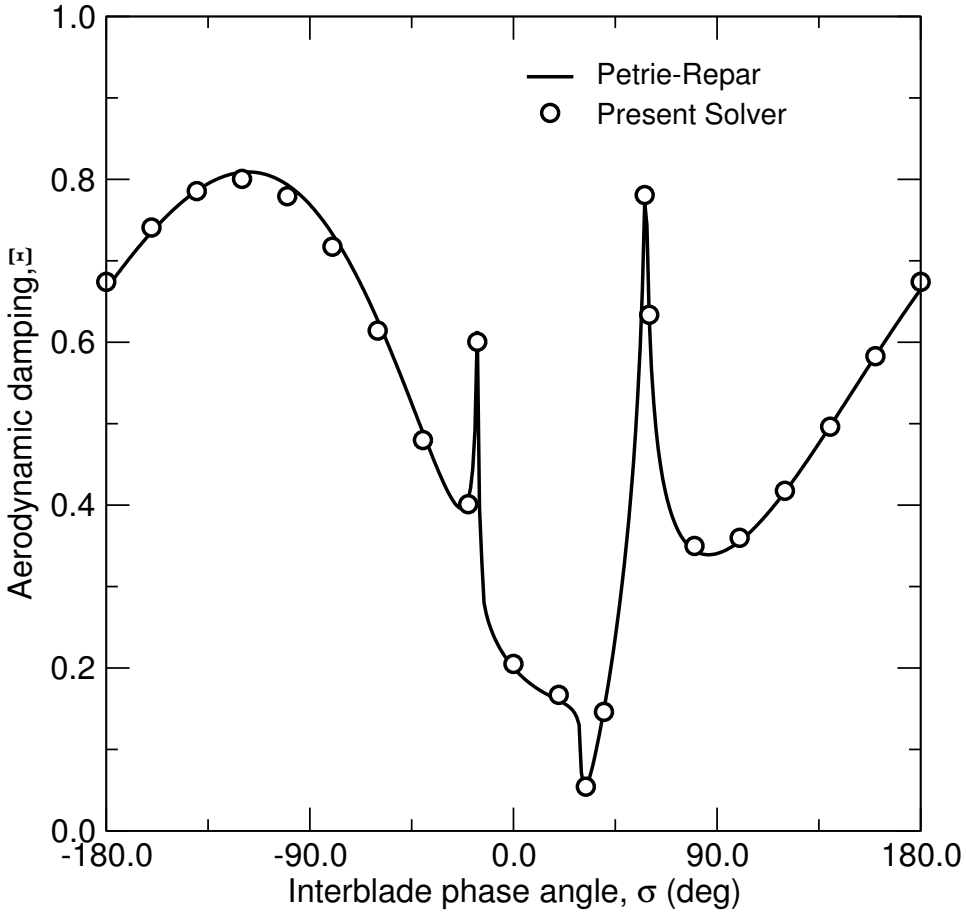


Figure 5.4: Aerodynamic damping coefficient versus IBPA σ for the Tenth Standard Configuration. Subsonic case, ω^*=0.5.

Transonic Case

In this section, we present results for unsteady flow under transonic flow conditions with an inlet Mach number of 0.8 and an inlet flow angle of 58 deg. At these flow conditions, a normal shock forms on the suction side of the blades (see Figure 5.5). First, we consider the mean flow surface pressure distribution, which is plotted in Figure 5.6.

Next, it is assumed that the blades pitch about their mid-chords at a reduced frequency of 0.5 and an interblade phase angle of 0 deg. The imaginary part of the unsteady surface pressure coefficients obtained from our flow solver with one harmonic together with those from the time-linearized solver of Petrie-Repar [95] are shown in Figigure 5.7. As can be seen, the present solver displays an oscillatory behavior compared to the time-linearized approach. This is mainly due to the fact that Jameson's scheme used in this work has a tendency to generate over- and under-shoots around shocks. As expected, a higher second-order dissipation coefficient typically used in Jameson's scheme yields a smoother solution around the shock. On the other hand, in his time-linearized flow solver Petrie-Repar [95] uses the AUSMDV scheme, which is known to be less susceptible to oscillations near shocks resulting in a slightly lower impulse.

Finally, we computed the unsteady aerodynamic response of the blades to pitching motion at a number of different interblade phase angles. The aerodynamic damping values are shown in Figure 5.8. The present method is in good agreement with the

time-linearized solution, except for the peak value at the resonant condition, which is usually difficult to predict accurately. These results demonstrate the accuracy of the present harmonic balance method in predicting dynamically linear inviscid flows in two-dimensional cascades. A simple two levels V-cycle multigrid together with local time stepping and implicit residual smoothing were used to accelerate the convergence rate. It is noted that our harmonic balance solver starts from the converged steady state solution. Shown in Figure 5.9 is the convergence history of the root mean square global residual with and without these acceleration techniques. Computational efficiency has been improved substantially with these acceleration techniques and the convergence rate of the harmonic balance solver is identical to that of the steady state solver. Therefore, computational cost of the harmonic balance method scales well with the number of harmonics. Note that our main purpose in developing a harmonic balance code is to be able to accurately predict nonlinear unsteady flows in turbomachinery. In the next section, we will demonstrate this capability for a transonic turbine undergoing large amplitude vibrations.

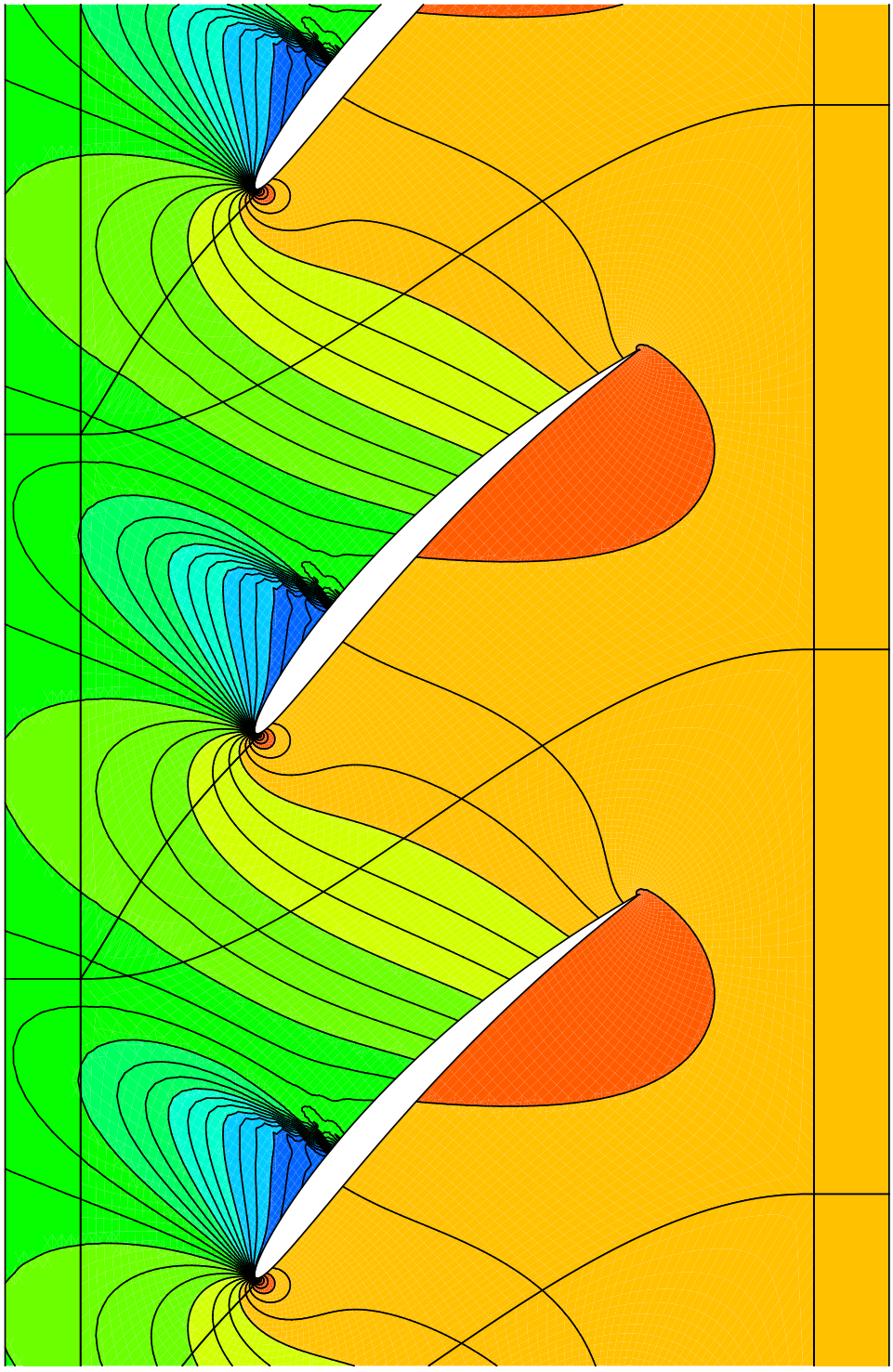


Figure 5.5: Static pressure contours for the mean flow of the Tenth Standard Configuration. Transonic case.

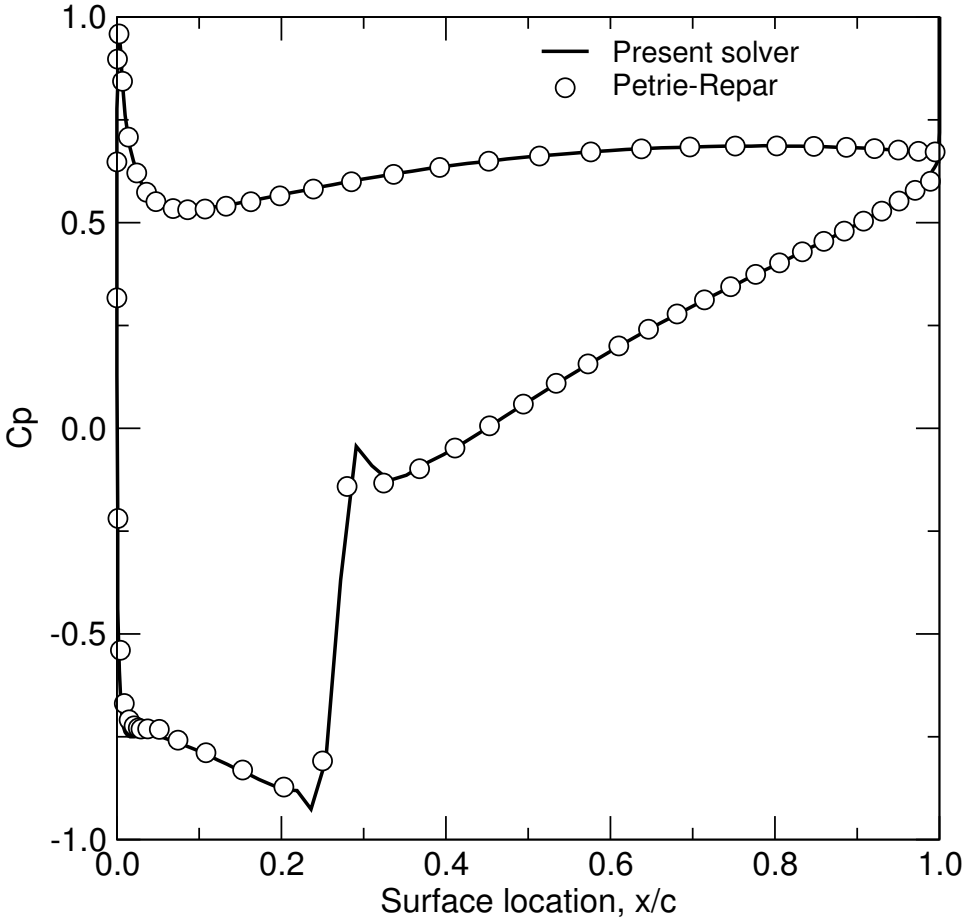


Figure 5.6: Pressure coefficient distribution for the Tenth Standard Configuration steady state. Transonic case.

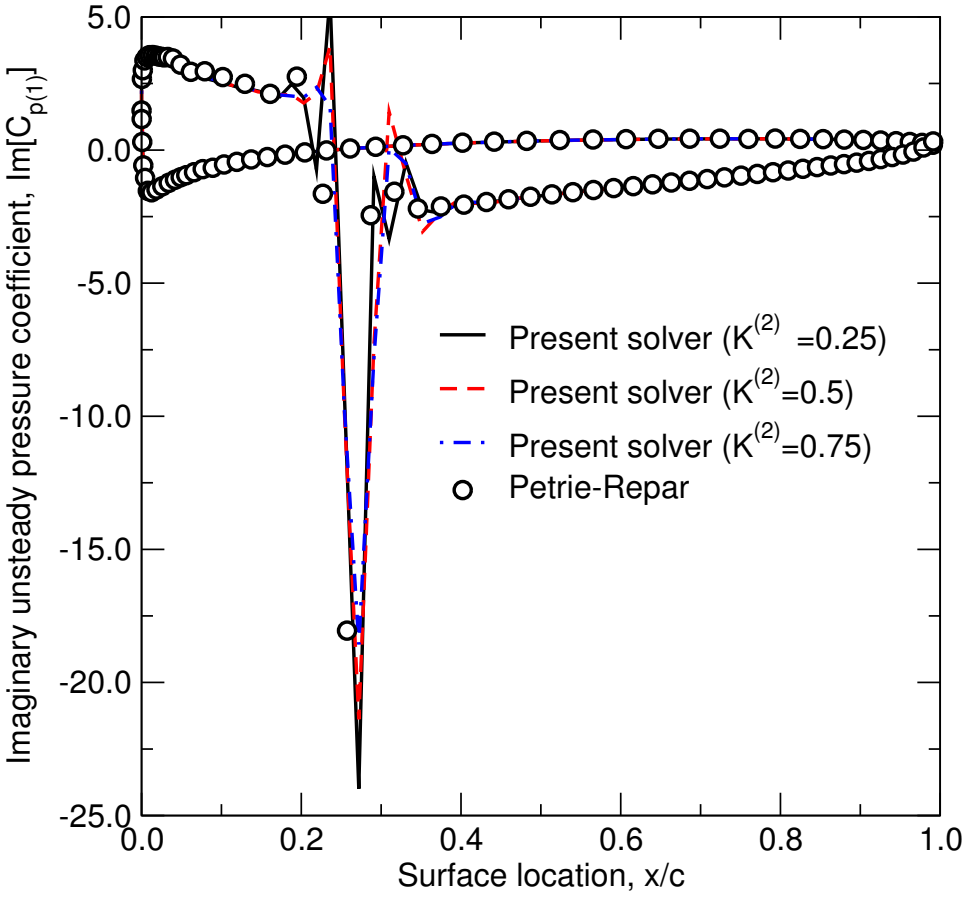


Figure 5.7: Imaginary unsteady pressure coefficient distribution for the Tenth Standard Configuration. Transonic case, σ=0 deg, ω^*=0.5.

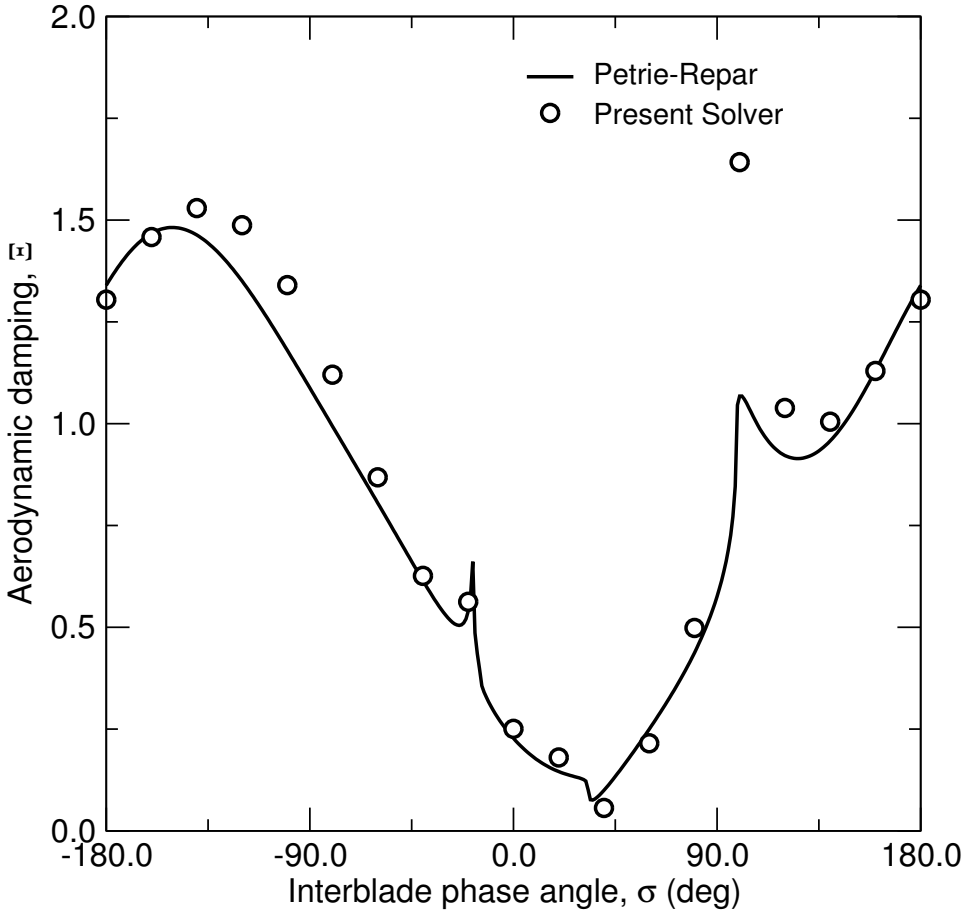


Figure 5.8: Aerodynamic damping coefficient versus IBPA σ for the Tenth Standard Configuration. Transonic case, ω^*=0.5.

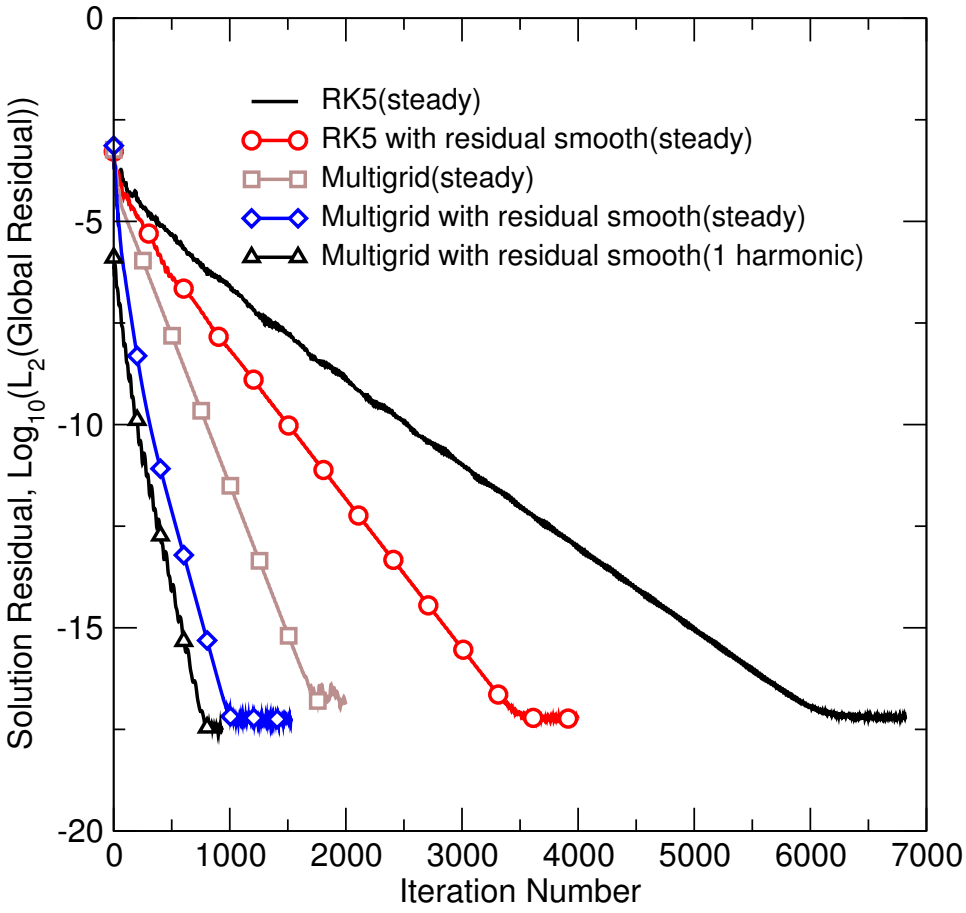


Figure 5.9: Convergence history for the Tenth Standard Configuration. Subsonic case.

5.1.2 Eleventh Standard Configuration

Eleventh Standard Configuration[96] is a two-dimensional viscous turbine cascade (see Figure 5.10). The turbine chord is 77.8 mm, the blade-to-blade gap is 56.55 mm and the stagger angle is -40.85 deg. Experimental measurements for this configuration were performed by Fransson et al. [96]. Two-dimensional turbine geometry coordinate and experimental data, measured from the midspan of the three-dimensional blade are available and a number of investigators compared their time-linearized and time-accurate computations[7, 96–98] to available data. A number of different flow conditions are available for this turbine. However, we only consider the transonic off-design condition in this paper mainly due to the fact that it is the most interesting and challenging test case. The flow enters the blade row at 34 deg with respect to the axial axis and exits with an isentropic Mach number of 0.99. The isentropic Mach number is the Mach number one could reach without any losses in the flow. It is defended as

$$Ma_{ise} = \sqrt{\left(\left(\frac{p_{0,in}}{p}\right)^{\frac{\gamma-1}{\gamma}} - 1\right) \cdot \frac{2}{\gamma - 1}},$$

where $p_{0,in}$ denotes to inlet total pressure and p denotes to the static pressure. The Reynolds number, based on inlet flow conditions and the chord length, is approximately 1,100,000. Figure 5.10 shows the H-O-H viscous computational grid, 29315 nodes in total, with 385×65 nodes in the O-grid block. The distance from the first inner node to the wall is 1.0×10^{-5} times the chord. We must note that this grid

resolution is typically high for our solver. However, coarser grids for this case did not provide grid independent results.

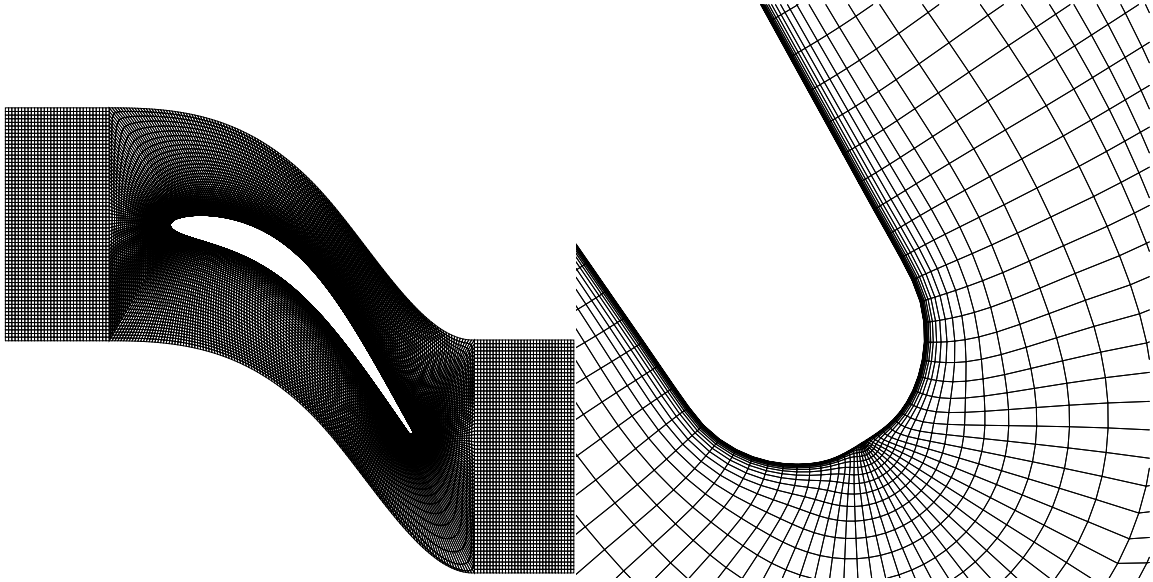


Figure 5.10: Left: Computational grid for the Eleventh Standard Configuration. Right:Close-up of the grid near the trailing edge.

First, we consider the steady flow. As shown in Figure 5.11 there is a separation bubble near the leading edge on the suction side due to the high incidence angle. In addition, a weak shock forms on the suction side of the blades at approximately 80% of the chord (see Figure 5.12). Figure 5.13 shows the steady isentropic Mach number distribution on the wall. Overall the predicted values are in good agreement with the experimental data, except for a small region upstream of the weak shock. However, as pointed out by Fransson et al.[96], fairly small changes in the inlet flow conditions may

result in significantly different flow structures near the shock, which was also observed by other investigators. Next we turn our attention to the unsteady computations.

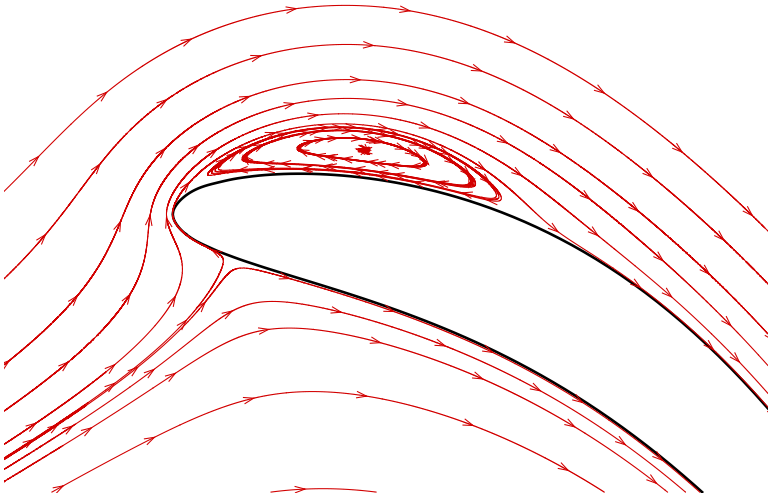


Figure 5.11: Streamline near the leading edge for the Eleventh Standard Configuration.

The blades undergo a plunging motion (normal to the chord) with a reduced frequency of 0.309 (based on the exit velocity). The amplitude of vibration is 0.0035 times the chord length and the interblade phase angle is 180 deg. The amplitude of vibration is relatively small resulting in a dynamically linear flow, which can be accurately predicted using a single harmonic. Figure 5.14 shows the first harmonic of unsteady pressure distribution on the wall. The discrepancy between the experimental data and the predicted solution is noticeable in the vicinity of the suction surface trailing edge. This may be due to inaccurate prediction of the shock/boundary-layer interaction

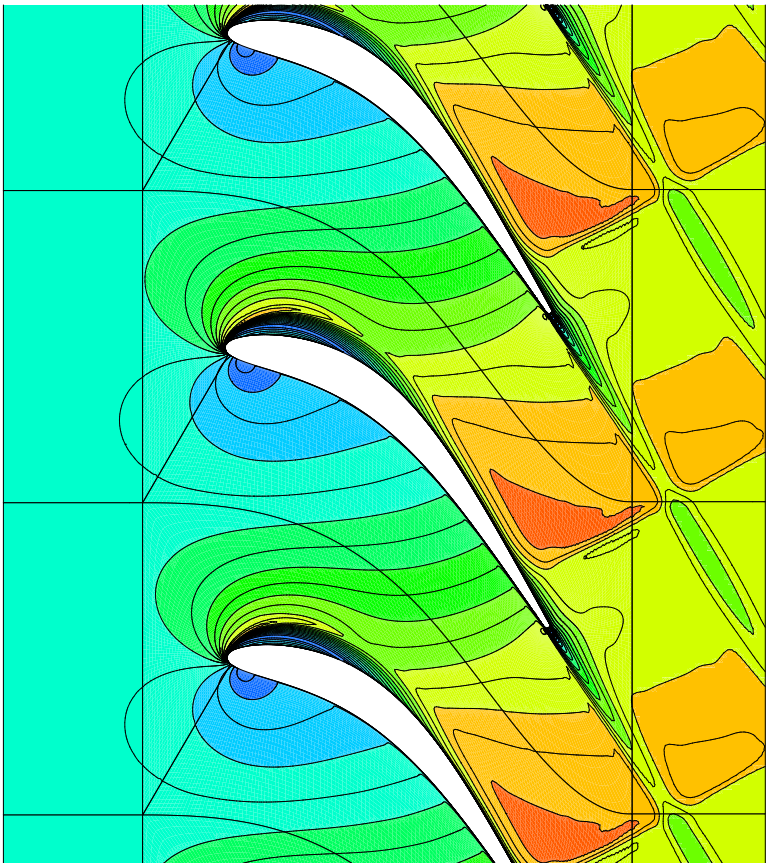


Figure 5.12: Steady state Mach number contour for the Eleventh Standard Configuration.

as well as uncertainties in measurements. However, the present solution is in good agreement with Petrie-Repar's time-linearized results[95] whereas the agreement with the time-accurate solutions of Cinnella et al. [7] is not satisfactory. For completeness, the aerodynamic response was computed for other interblade phase angles, which is presented in Figure 5.15. Based on the numerical solutions, the configuration is stable for all interblade phase angles under these flow conditions.

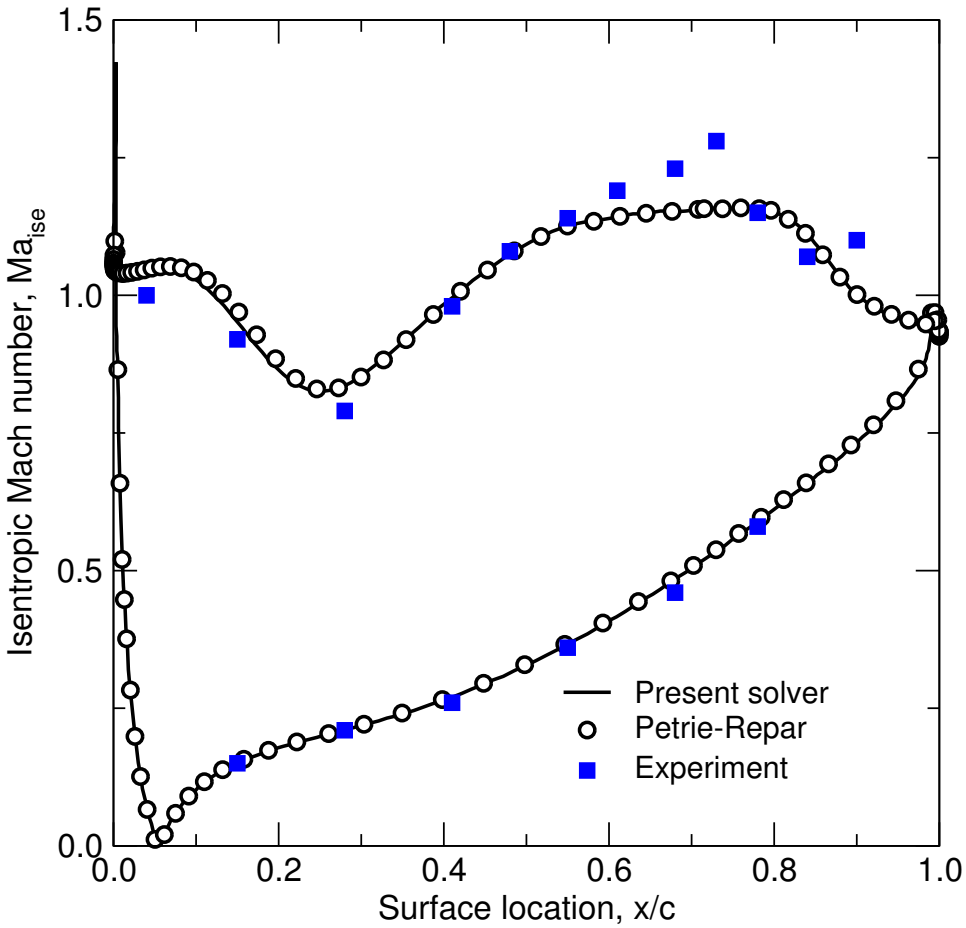
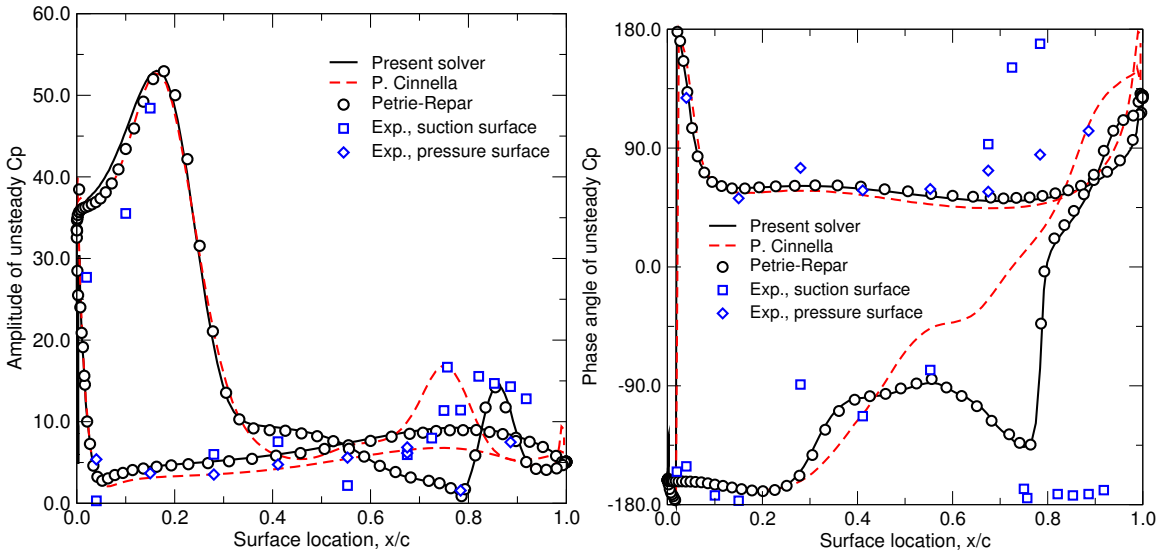


Figure 5.13: Isentropic Mach number surface distribution for the Eleventh Standard Configuration.

Next, we consider possible nonlinear aerodynamic effects due to large amplitude blade motions. First, to determine the number of harmonics required for "mode convergence", we compute the unsteady response for a 10% plunging motion. Since this amplitude of vibration is relatively large, one may expect to see nonlinear effects in the flowfield. The mean flow pressure coefficient, and the real and imaginary components of the first harmonic are shown in Figs. 5.16. As can be seen, the mean



(a) Amplitude of Cp **(b)** Phase angle of Cp

Figure 5.14: First Harmonic of unsteady pressure coefficient distribution for the Eleventh Standard Configuration, ω^*=0.309, σ=180 deg.

pressure distribution for three, five and seven harmonic solutions are in very good agreement, but are significantly different from a single harmonic solution. Considering the first harmonic of the unsteady response, it is clear that the three harmonic solution is somewhat different from five and seven harmonic solutions. Therefore, it can be said that harmonic convergence can be achieved for as few as five harmonics (or 11 sub-time level solutions), and single harmonic computations do not produce accurate results. Therefore, for the rest of the results we retained five harmonics in our computations. Also, the fact that the mean pressure distribution is significantly different for a single harmonic computation compared to three, five and seven harmonic computations indicates a nonlinear behavior.

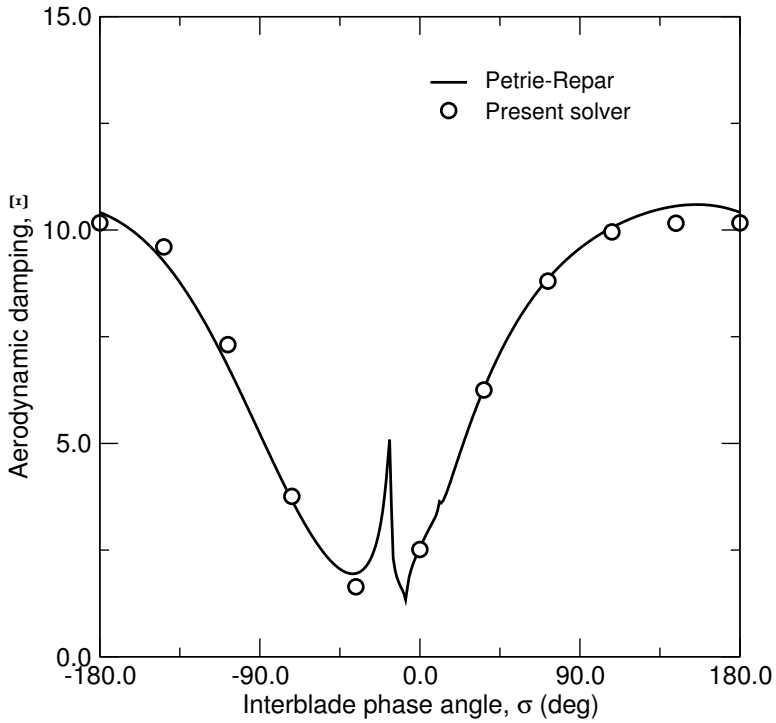
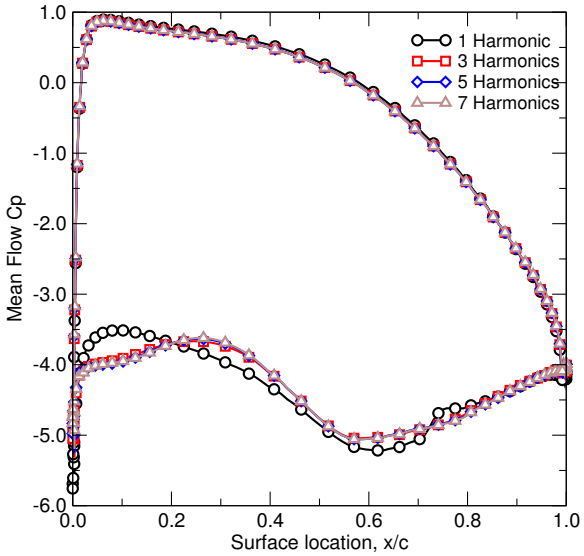


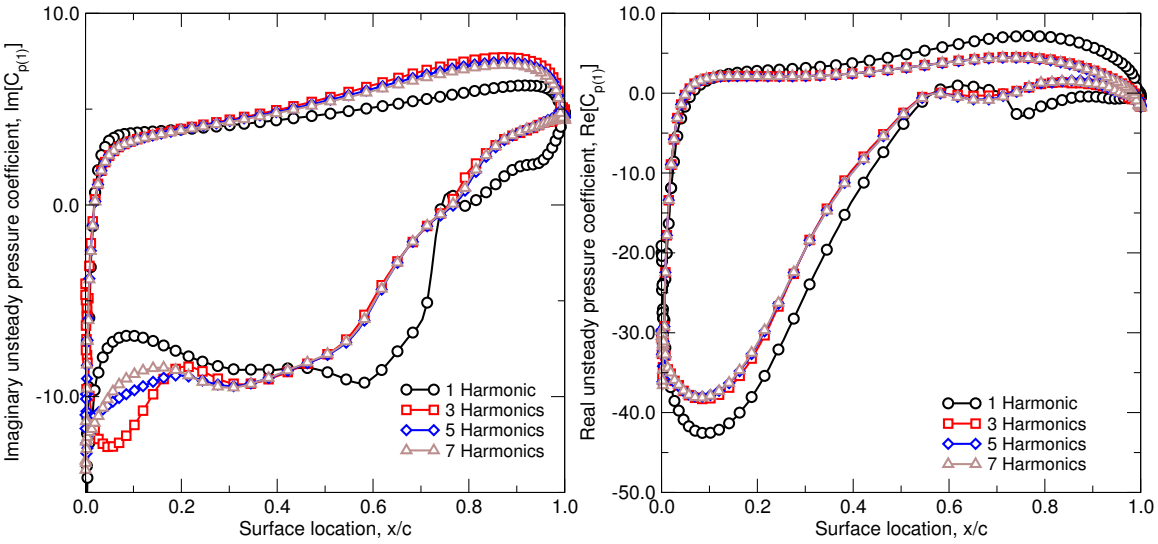
Figure 5.15: Aerodynamic damping coefficient versus IBPA σ for the Eleventh Standard Configuration, ω^*=0.309.

Next, we investigate nonlinear effects due to blade plunging amplitude. The aerodynamic response to three different blade amplitudes, namely 1%, 5% and 10% of the chord, were computed by the present harmonic balance technique and the results are presented in Figure 5.17. It is seen that both the mean flow and the first harmonic of the unsteady flow change significantly with increased amplitudes of plunging, especially near the separation bubble and the shock regions. The unsteady shock impulse peak gets smeared out as the bending amplitude increases. This clearly shows the presence of nonlinearities in the flow field. Although the blade is forced to plunge at its first harmonic, the spatial nonlinearity of flow field could introduce

higher harmonics spectral content even for small-amplitude vibrations (1% chord plunge), especially near strong nonlinearities such as separation bubbles and shocks. Figure 5.18 and Figure 5.19 show the second and the third harmonics of the unsteady pressure coefficient (scaled by the plunge amplitude), respectively. Note that the amplitude of the higher harmonics decay indicating a Fourier convergence.

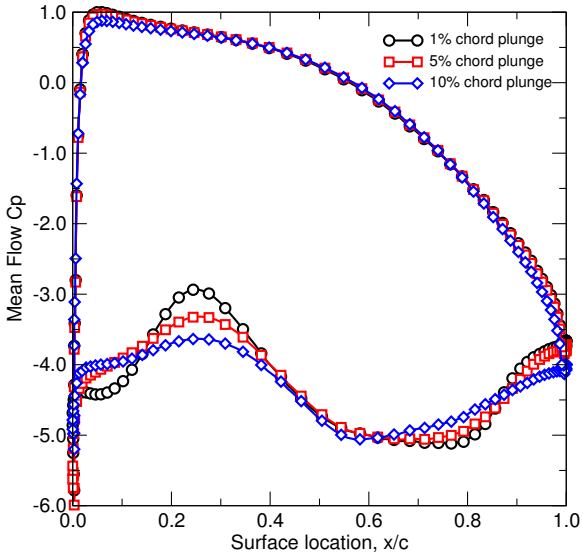


(a) Mean flow Cp

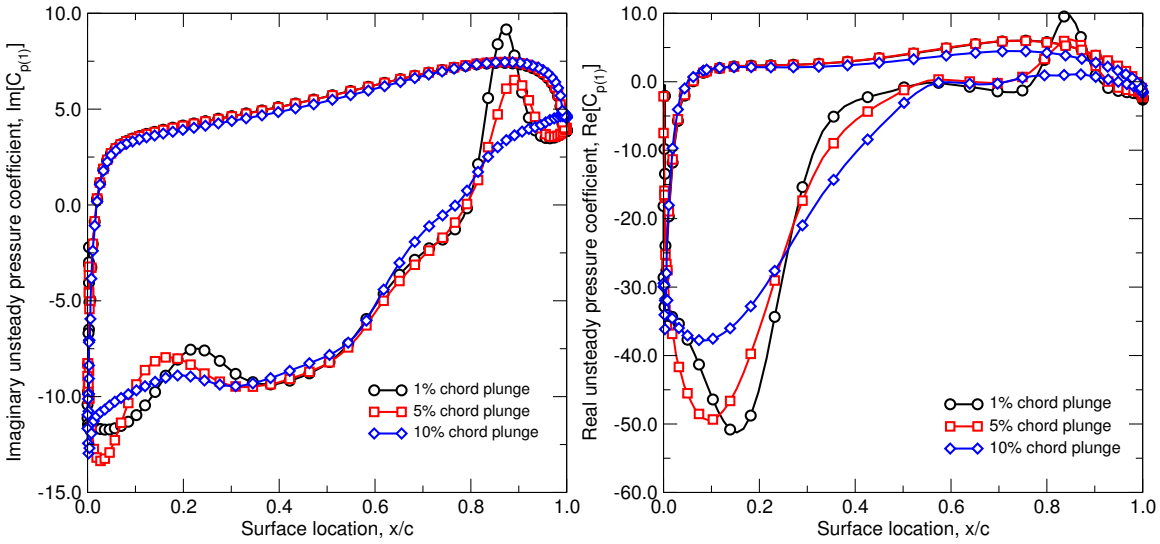


(b) Imaginary Cp **(c)** Real Cp

Figure 5.16: Pressure coefficient distribution for the Eleventh Standard Configuration with 10% motion, ω^*=0.309, σ=180 deg.



(a) Mean flow Cp



(b) Imaginary Cp

(c) Real Cp

Figure 5.17: Pressure coefficient distribution for the Eleventh Standard Configuration, ω^*=0.309, σ=180 deg.

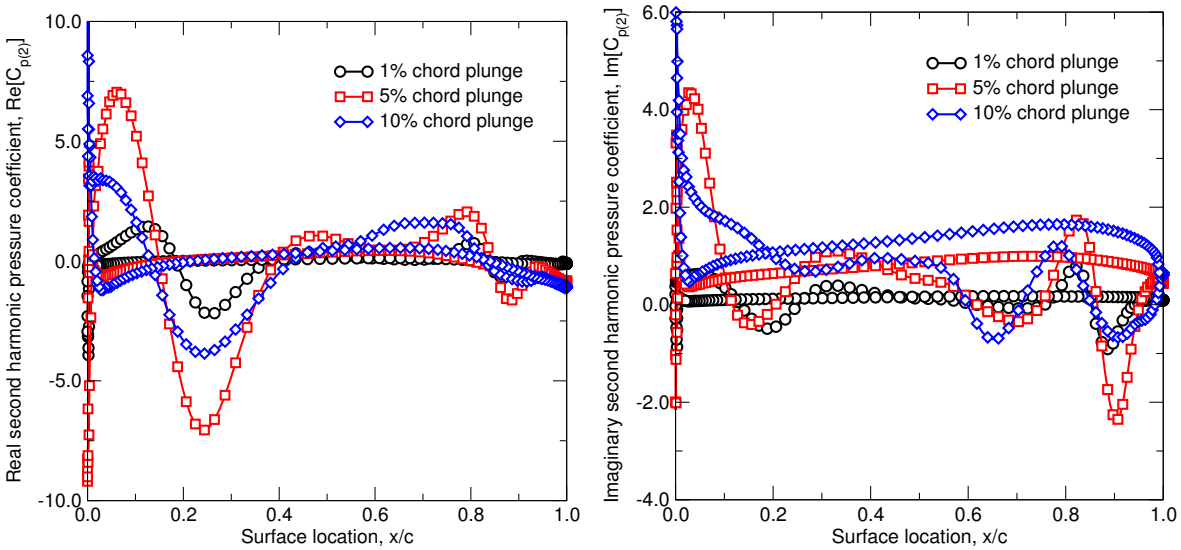


Figure 5.18: Second harmonic of unsteady pressure distribution on the blade surface for 1, 5 and 10% plunging, $\omega^* = 0.309$, $\sigma = 180$ deg.

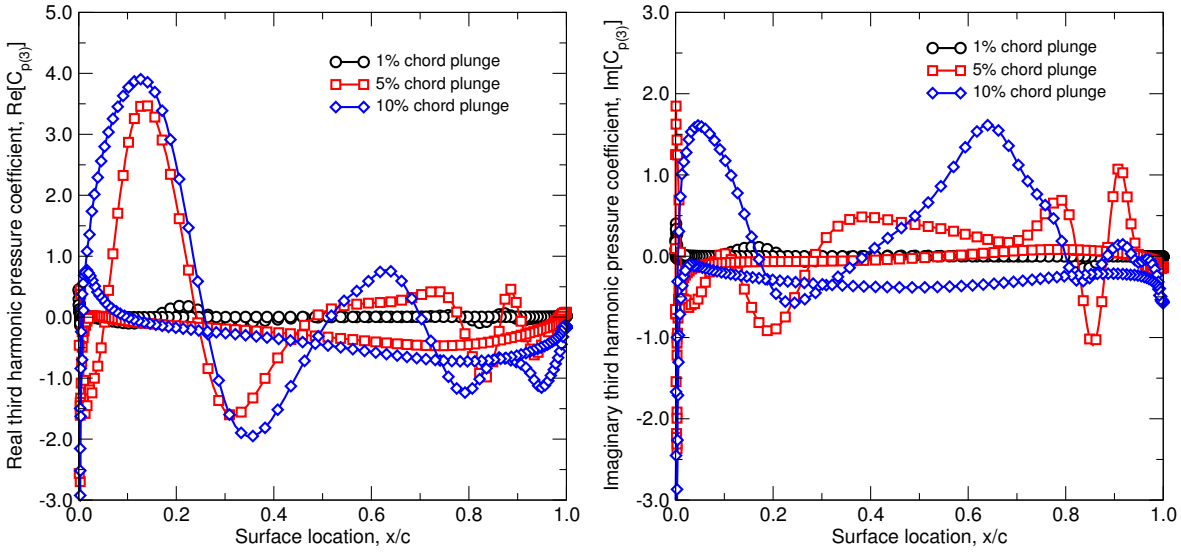


Figure 5.19: Third harmonic of unsteady pressure distribution on the blade surface for 1, 5 and 10% plunging, $\omega^* = 0.309$, $\sigma = 180$ deg.

5.1.3 Unsteady Laminar Flow Around a Stationary Circular Cylinder

In this section, we consider the unsteady laminar flow around a stationary circular cylinder. For specific values of Reynolds number ($47 \leq Re \leq 200$), Karman vortex shedding occurs behind the cylinder. Generally, the frequency of shedding (ω) for Reynolds numbers of interest must be prescribed for the HB solution. The HB solver can converge to the zero machine accuracy only if the specified shedding frequency is correct. If the prescribed value is incorrect, the HB solution will not converge and the residual of the unsteady solution will display a low-level limit-cycle behavior.

Figure 5.20 shows the computational grid, with 275×65 nodes in the O-block. The distance from the first nodes to the wall is 1×10^{-3} of the cylinder diameter and the far-field boundary is located about 20 diameters away. We assume that the top and the bottom boundaries are periodic with an interblade phase angle of zero. Although, the periodicity condition is somewhat inaccurate, its effects are minimized since the boundaries are placed far away from the cylinder.

In order to save computational time, a steady solution is used as the initial condition for the time-accurate and harmonic balance solutions. It must be noted that for this case, the flow is laminar and the turbulence values are set to zero in our flow solvers. To trigger the unsteady vortex shedding, the flowfield is perturbed by rotating the cylinder for the first 20 multigrid iterations (for both HB and time-accurate solutions). As shown in Figure 5.21, for $Re = 176$, the instantaneous

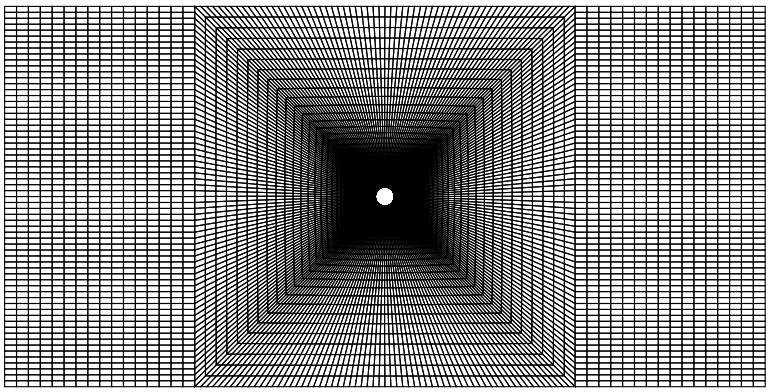
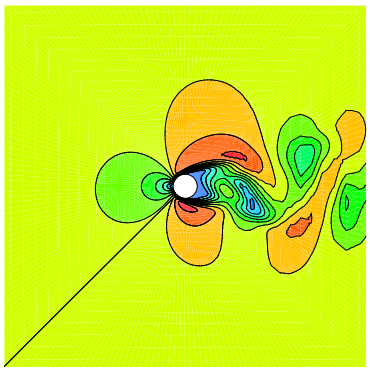
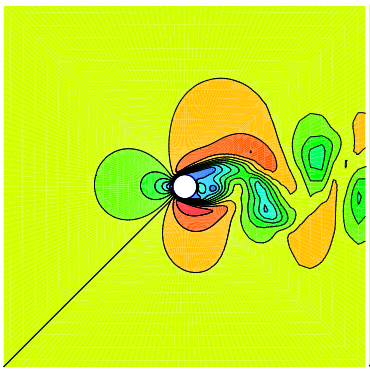


Figure 5.20: Computational grid for the circular cylinder.

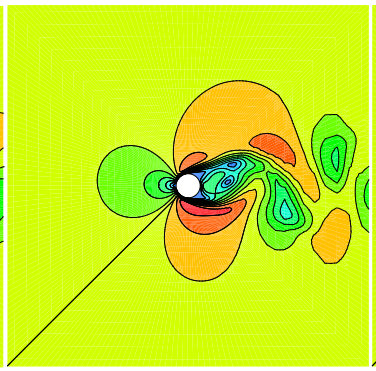
velocity contours obtained by our HB solver clearly demonstrates the vortex shedding phenomenon downstream of the cylinder. These results were obtained where an initial guess of ω was input into the solver and the frequency search (Eq. (2.15)) was turned on after 300 iterations. As can be seen from Figure 5.22, the residual stalls after first 300 multigrid iterations with a guessed initial frequency, then the frequency search technique is turned on to drive the residual to zero machine accuracy with 6000 multigrid iterations.



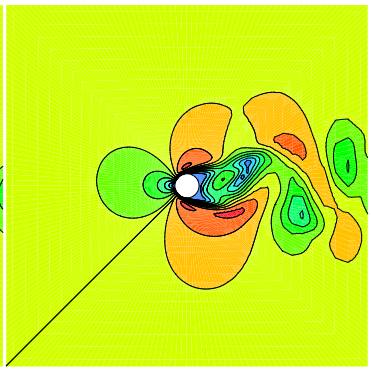
(a) $t = 0$



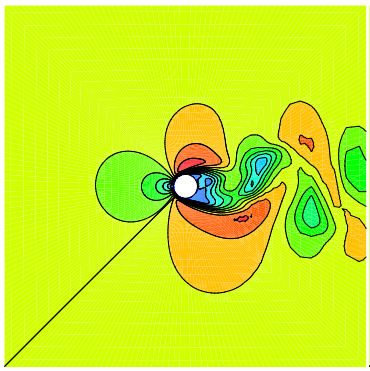
(b) $t = T/7$



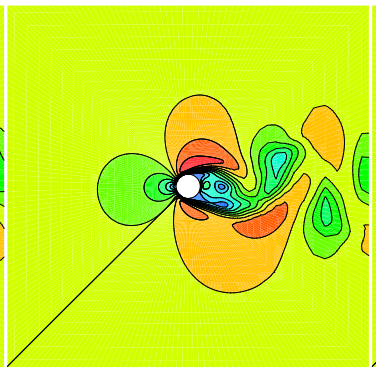
(c) $t = 2T/7$



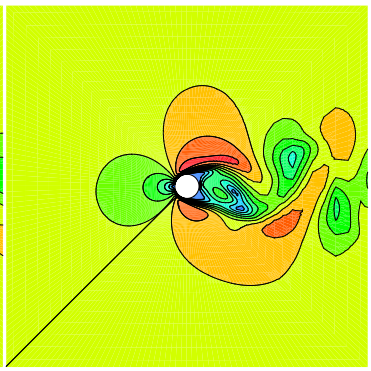
(d) $t = 3T/7$



(e) $t = 4T/7$



(f) $t = 5T/7$



(g) $t = 6T/7$

Figure 5.21: Instantaneous velocity contours computed using the HB solver.

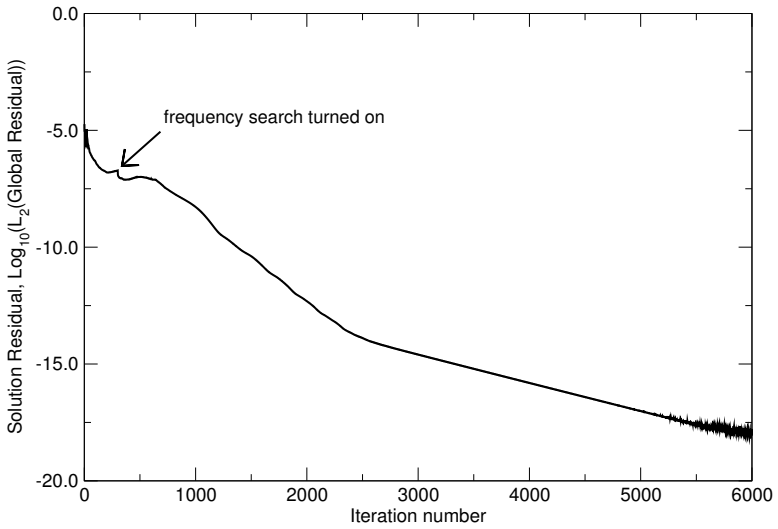
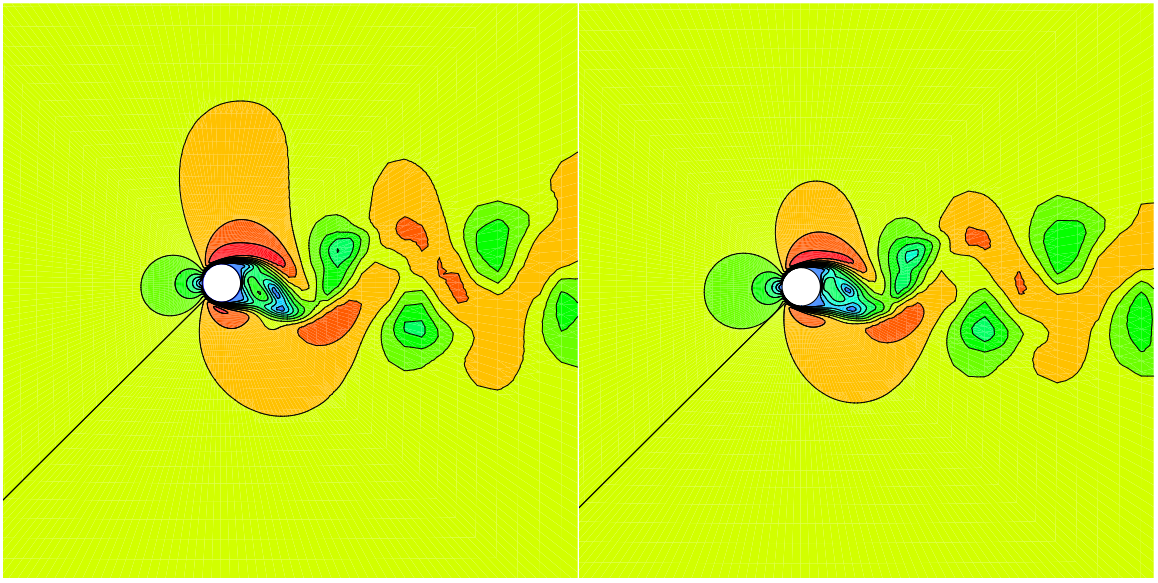


Figure 5.22: Convergence history for the HB solver.

Next, we compare the HB solutions to those obtained from our time-accurate solver. Figure 5.23 shows the instantaneous velocity contour plots for both solvers. As can be seen, the agreement between the solvers is good. The small differences in the contour plots are due to the fact that the physical time levels for both solvers are slightly different from each other. Figure 5.24 shows the lift and drag force coefficients from both solvers. Although a quasi-periodic response is obtained for the time-accurate solver after three hundred physical time steps (six shedding cycles), in practice we need to run more shedding cycles since the response is not absolutely periodic. Overall, it is seen that the agreement between the solvers is good although the time-accurate solver apparently needs more computations to reach periodic state. The fact that the HB solver attains periodicity with much less effort demonstrates the strength of the technique compared to the dual time-stepping technique.



(a) Time-Accurate Solution **(b)** HB Solution

Figure 5.23: Instantaneous velocity contours for a circular cylinder in cross flow. $Re = 176$.

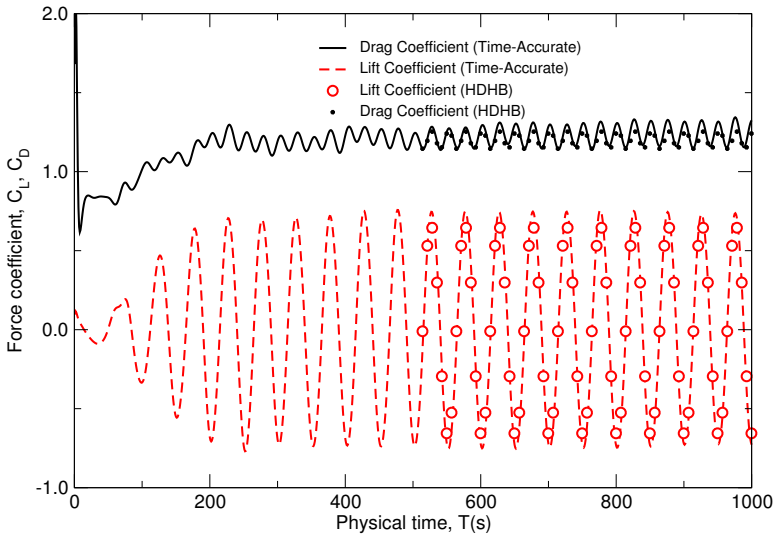


Figure 5.24: Lift and Drag Coefficient for a Circular Cylinder

Next, we compare our solvers to available experimental data[99]. Figure 5.25 plots the Strouhal number versus Reynolds number. Note that the values for the Strouhal number were obtained through the frequency search method employed in this work and it is seen that the values are determined pretty accurately. Overall, the solutions of the time-accurate and the HB methods (three harmonics retained in the solver) are in good agreement with the experimental data.

Finally, we consider the efficiency of the two methods. For the HB solutions, it has taken 112 minutes to reach machine accuracy on a 2.8 GHz Intel Core i7 processor, and 26 minutes to reach an acceptable engineering accuracy (10^{-10}). For the time-accurate solver, 50 physical time levels are computed within each shedding cycle and 100 inner iterations are performed to reduce the residual by four orders of magnitude to around 10^{-10}. The overall computational time required was 204 minutes for one

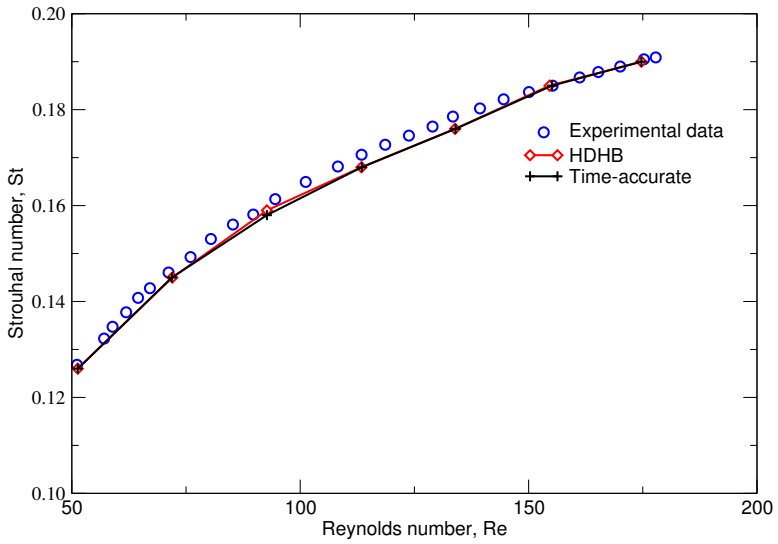


Figure 5.25: Strouhal Number Versus Reynolds Number

thousand physical time steps. As noted earlier, to reach a purely periodic state, one needs to run the solver longer. This shows that, for this problem, the HB method requires around 5-10 times less computational effort than the time-accurate technique.

5.1.4 Three-Dimensional Steady Flow through the NASA Rotor 67 Fan

In order to validate the three-dimensional flow solver, steady viscous flow through the NASA Rotor 67 fan[100] is analyzed herein. The rotor consists of 22 blades. The design rotational speed is 16,043 RPM and the total pressure ratio is 1.63. An H-O-H topology grid was used in this work, with 227 nodes in the axial direction, 33 nodes in the tangential direction and 49 nodes in the radial direction for the O-block. Another H-block, with $89 \times 9 \times 9$ nodes, discretises the tip clearance region. Figure 5.26 shows the hub and the blade surface grid. Total pressure, total temperature, flow angles and turbulent intensity are specified at the inlet while the static pressure at the exit is determined from radial equilibrium equation with the static pressure prescribed at the hub. The inlet flow conditions considered here correspond to the near peak efficiency operation point. Shown in Figure 5.27 are circumferentially averaged total pressure, static pressure, total temperature and flow angle distribution along the radial direction at the exit. As we can see, there is good agreement between the present solver and the experimental data[100]. Although the NASA Rotor 67 case provides detailed experimental data for steady state CFD code validation, there are no unsteady experimental data that we are aware of. In the literature, many investigators have presented results from their time-dependent solvers for this case. However, the results are not consistent among these solutions[101–104]. Therefore, we have decided to use additional test cases to validate the unsteady three-dimensional HB solver.

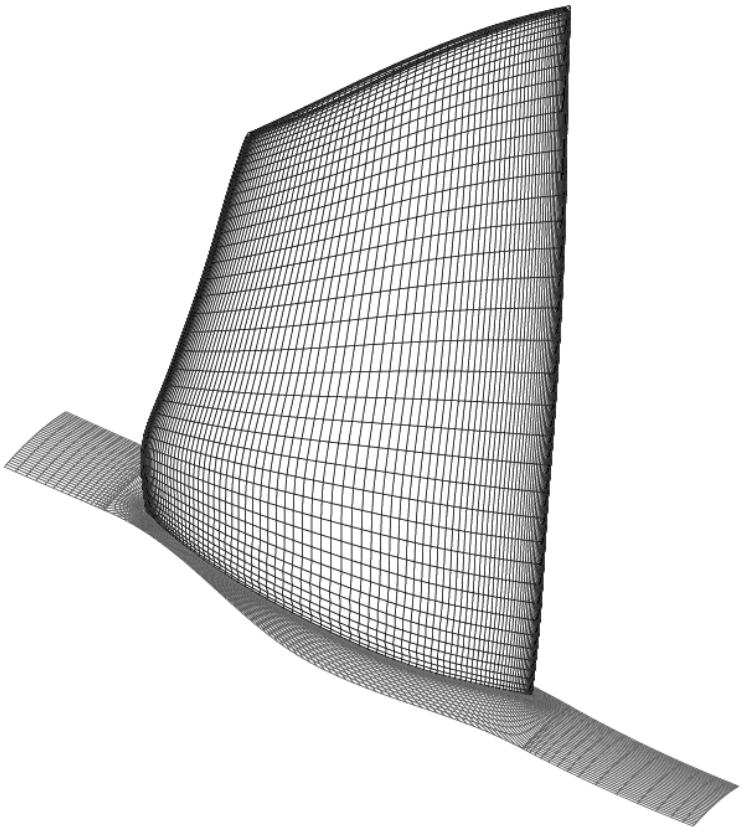


Figure 5.26: Hub and blade surface computational grid for the NASA Rotor 67 fan.

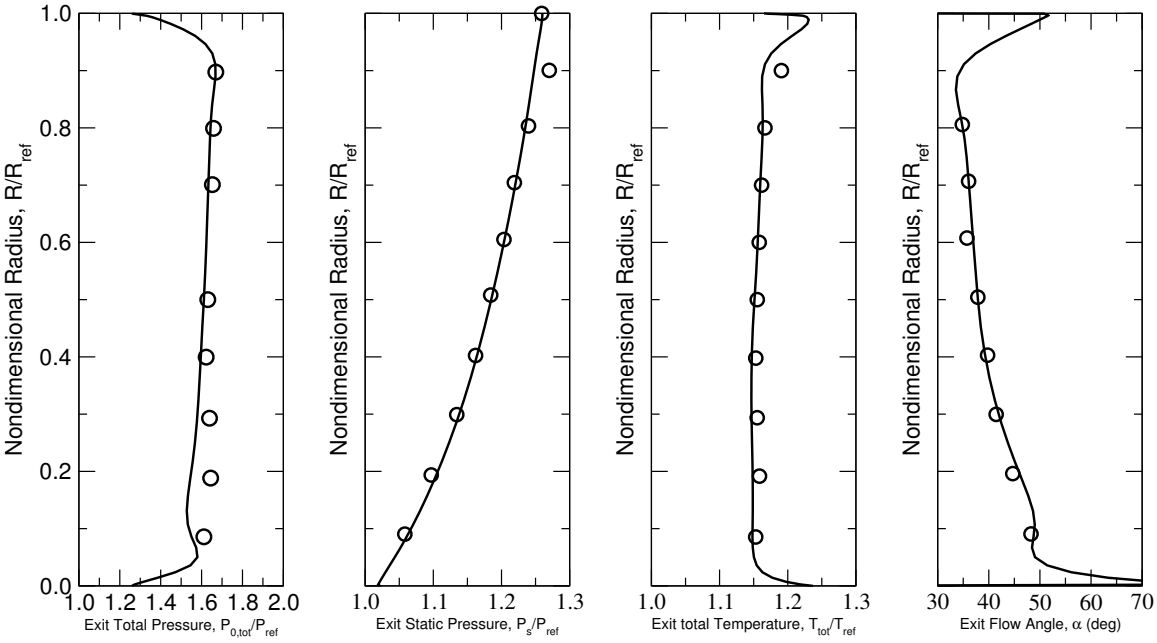


Figure 5.27: Experimental(o) and numerical solution (-) for NASA Rotor 67 fan: total pressure, static pressure, total temperature and flow angle distribution along radial direction at the exit (circumferentially averaged, near peak efficiency).

5.1.5 Inviscid Analysis of Three-Dimensional Tenth Standard Configuration

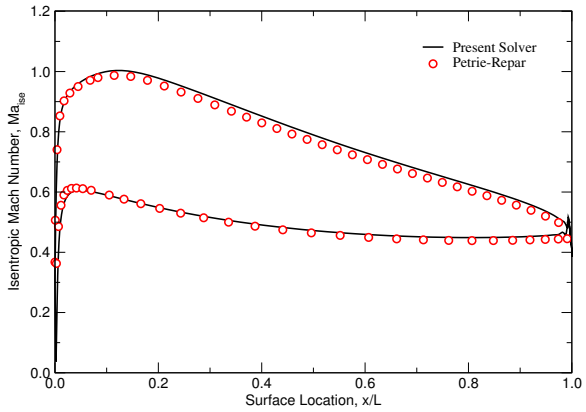
The three-dimensional Tenth Standard Configuration test case was proposed by Petrie-Repar et.al[105]. This configuration consists of 24 straight blades. The cross section of the blades is exactly the same as the two-dimensional cascade. The radius at the hub and the tip are 3.395 and 4.244 chord lengths, respectively. The cascades are assumed to be stationary. The inlet flow conditions, which are the same as the subsonic two-dimensional case, are summarized in Table 5.1. An inviscid slip boundary condition is specified at the hub and the tip. The back pressure is specified so that the average inlet Mach number is 0.7.

Table 5.1: Inflow conditions for the 3-D Tenth Standard Configuration.

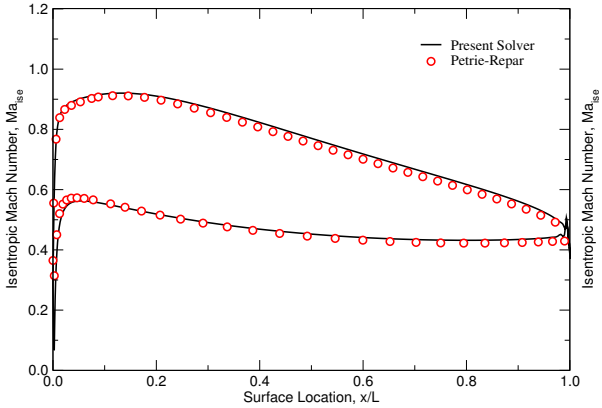
Total Pressure, p_o	$101.3kPa$
Total Temperature, T_o	$300K$
Inflow Angle, α	$55°$
Inflow Mach Number, Ma_{in}	0.7

The steady isentropic Mach number distribution at 10%, 50% and 90% blade spanwise locations are plotted in Figure 5.28. For unsteady computations, the blades are assumed to pitch around their middle chords with a reduced frequency of 0.5 and an interblade phase angle of 0 deg. The mode shape is constant over the entire spanwise direction. Thefore, it is assumed that the blades slide over the hub and

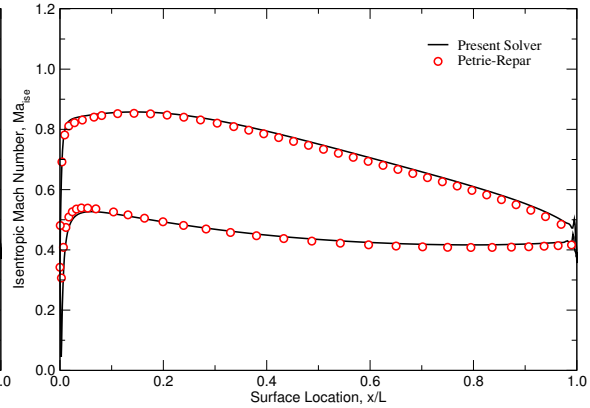
the shroud surfaces. The vribation amplitude is taken to be very small, so that a direct comparison can be made with a time-linearised solver. The imaginary part of the unsteady pressure coefficient is plotted in Figure 5.29. Finally, the aerodynamic damping coefficient versus different interblade phase angle angle values are plotted in Figure 5.30. The positive aerodynamic damping indicates the stability of the blades ensuring the structural integrity. Overall the present solutions are in good agreement with solutions of Petrie-Repar et al.[105].



(a) 10% span of the blade

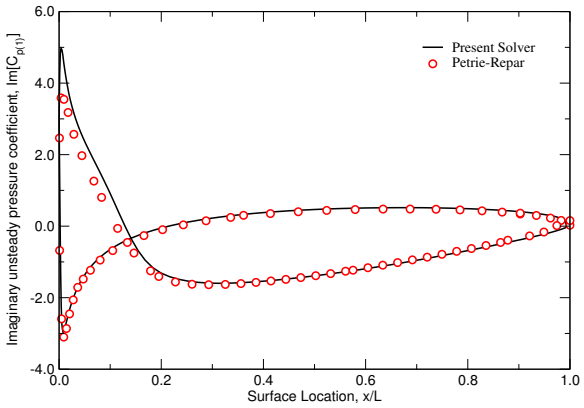


(b) 50% span of the blade

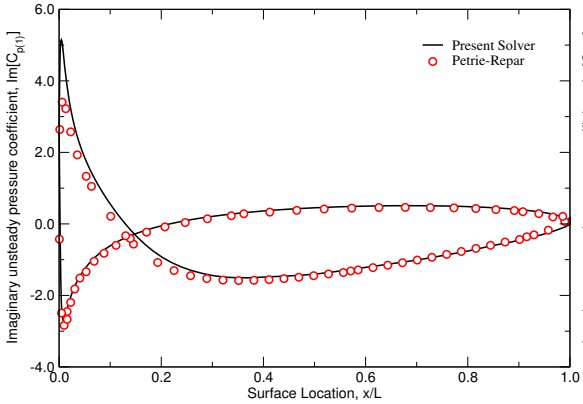


(c) 90% span of the blade

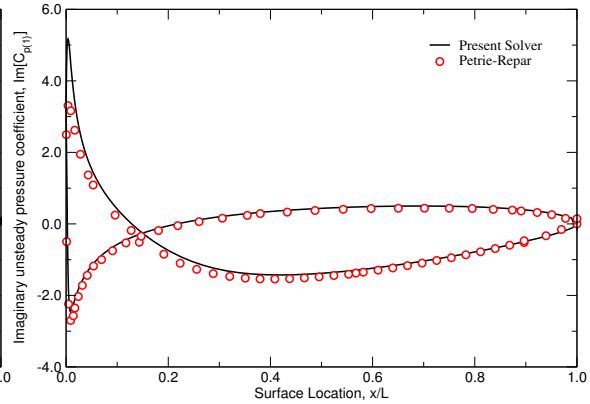
Figure 5.28: Isentropic Mach number distribution.



(a) 10% span of the blade



(b) 50% span of the blade



(c) 90% span of the blade

Figure 5.29: Imaginary part of unsteady pressure distribution, ω^*=0.5, σ=0 deg.

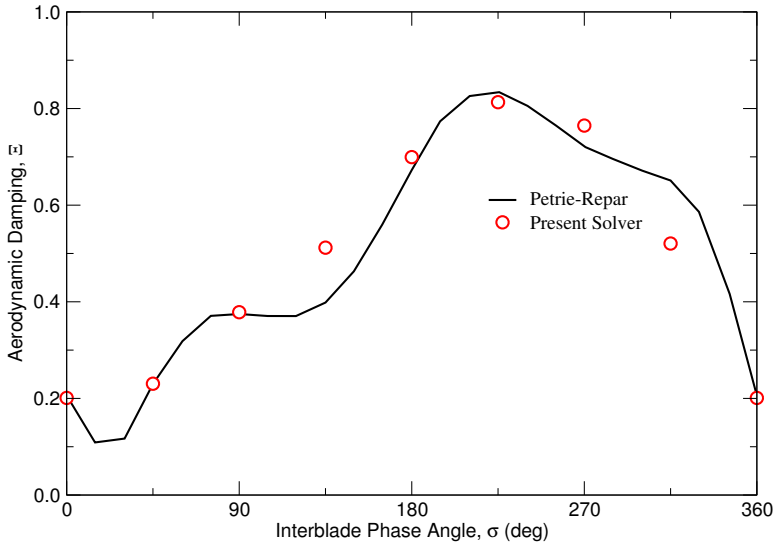


Figure 5.30: Aerodynamic damping versus interblade phase angle, ω^*=0.5.

5.1.6 Transonic Three-Dimensional Fourth Standard Configuration

A major difficulty in the simulation of three-dimensional aeroelasticity in turbomachinery is the lack of experimental data to validate numerical computations. Yang and He[106] have performed experimental research on a three-dimensional compressor cascade with tip clearance effects. Their studies, however, were limited to linear cascade. The Fourth Standard Configuration[94] is an annular turbine cascade. The three-dimensional SC4 consists of 28 blades, which can be generated from the two-dimensional profile by stacking it along the cross section gravity center. The steady state pressure data were measured at 25%, 50%, and 75% of the blade span direction and the unsteady pressure data was only measured at 50% of the blade span direction. Since the experimental measurement was carried out in 1986, the purpose of this case was to provide high quality data for two-dimensional CFD validation at the time. With the advance computing technology, It is now feasible to perform three-dimensional computations. Therefore, the three-dimensional blade geometry parameter and experimental data were recovered in a more recent report[107]. A couple of different flow conditions are available for this configuration. Cinnella et.al[108] have performed an aeroelastic analysis on the configuration in the subsonic flow regime. In this section, the transonic Case 628 is considered. Both steady and unsteady solutions are computed and are compared with the experimental data as well as time-accurate numerical solutions reported by McBean et al.[6].

The aeroelastic parameters for the Fourth Standard Configuration Case 628 are summarized in Table 5.2. The steady and unsteady surface pressure coefficients are defined as

$$C_p = \frac{p - p_i}{p_{oi} - p_i} \tag{5.1}$$

and

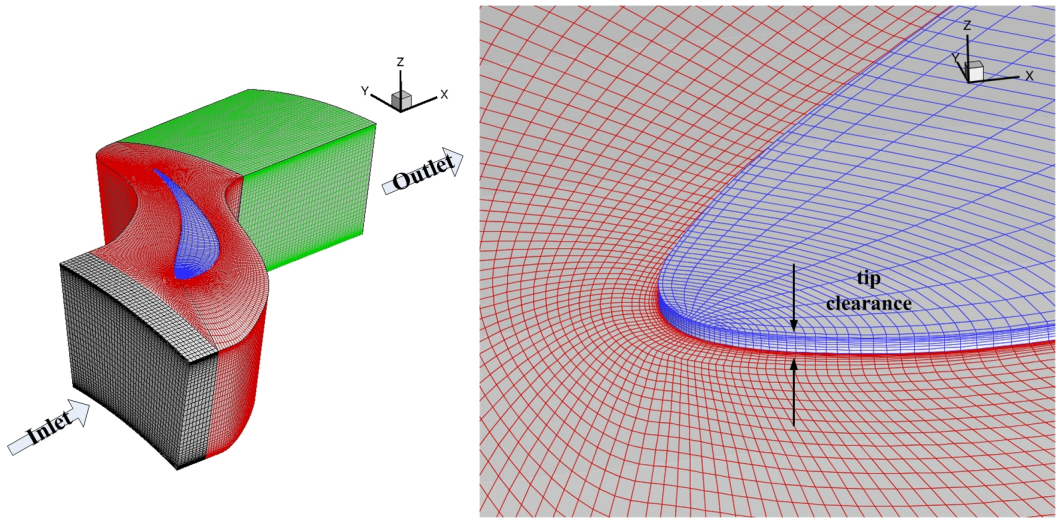
$$C_{p(n)} = \frac{p_{(n)}}{b_c(p_{oi} - p_i)}, \tag{5.2}$$

where b_c is the blade span, p_{oi} is the inlet total pressure and p_i is the inlet static pressure. After a re-evaluation of the original experimental data, however, it was

Table 5.2: Inflow conditions for the 3-D Fourth Standard Configuration Case 628.

Reynolds number, Re	5.9×10^5
Bending mode direction	$63.0°$
Bending amplitude at hub	3.15×10^{-3}
Bending amplitude at tip	4.91×10^{-3}
Inflow isentropic Mach number, $Ma_{ise,in}$	0.2
Inflow angle, α	$-12.0°$
Full chord reduced frequency, ω^*	0.1558
Outlet isentropic Mach number, $Ma_{ise,out}$	1.39

found that the inlet flow angle may be larger than the originally reported value[109], which could explain the difference between the experimental and computed steady state pressure distributions, especially in the leading edge region. In our code, the inlet flow angle is set to be $-26°$, same as McBean et al.[6]. A three-dimensional H-O-H topology grid, with $305 \times 45 \times 49$ nodes in the O-block, is used model a single



(a) (b)

Figure 5.31: Left: computational grid for the Fourth Standard Configuration. Right: close-up of the grid near the tip clearance region.

blade passage. The tip clearance region, about 0.3 mm, is filled with a fourth H-block with a grid size of $141 \times 13 \times 9$. The entire computational grid consists of one million nodes approximately. Figure 5.31 shows the four blocks of the computational grid and the close-up grid near the tip clearance region.

The total pressure, total temperature, inlet flow angles and turbulent working variable are specified at the inlet, whereas the static pressure at the exit is specified according to the experimental data. The steady state Mach number at the 50% span location is plotted in Figure 5.32. An interesting shock structure is captured at the trailing edge and the shock impinges near the blade pressure side about 65% blade surface location. The steady state pressure coefficients at 25%, 50% and 75% span locations are plotted in Figure 5.33. The predicted point of shock impingement is

about 10% behind the experimental data. The flow field on the pressure side actually separates because of the shock, which explains the difficulty for an accurate prediction of the pressure coefficients there. For unsteady aeroelastic analysis, the blades are allowed to vibrate in their first bending mode. The interblade phase angle is assumed to be 180°. With the use of the complex periodic boundary conditions, and only one blade passage is required to model flowfield, which makes the current method computationally efficient compared to a time-accurate method. Because of the small amplitude vibration, the unsteady flow field is essentially linear, only one harmonic is retained in the harmonic balance unsteady computations. The first harmonic of unsteady pressure coefficients at midspan are plotted in Figure 5.34. The shock induced boundary layer separation imposes a challenge for the unsteady pressure prediction as well.

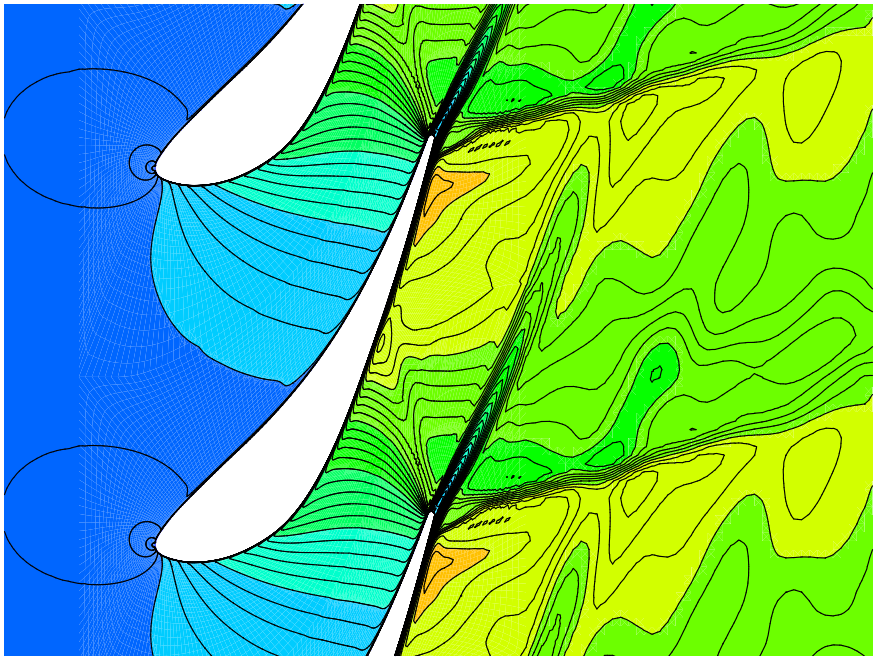


Figure 5.32: Steady state Mach number contours for the Fourth Standard Configuration at 50% span location.

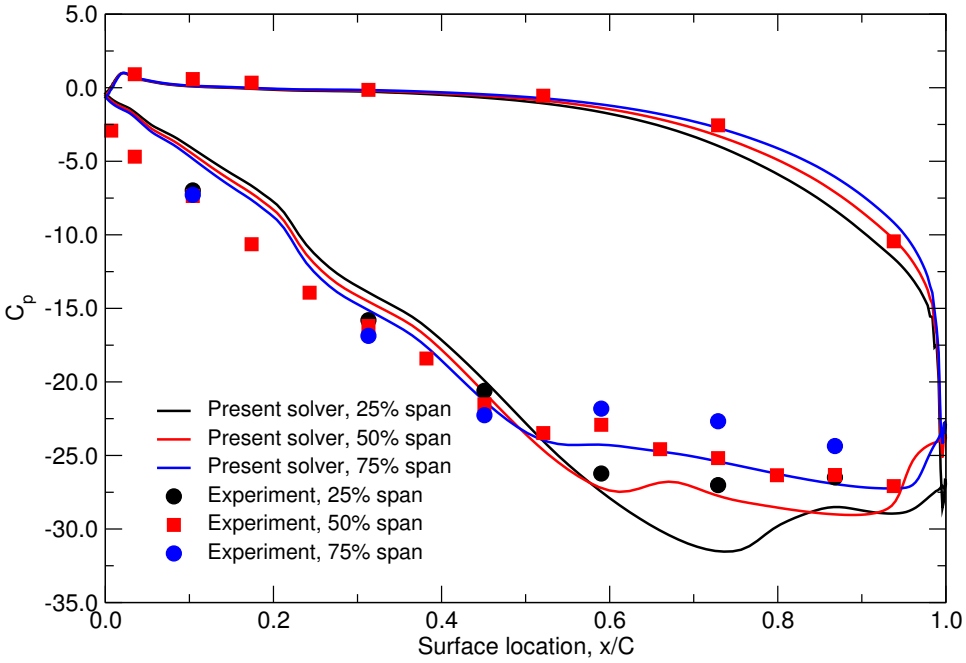
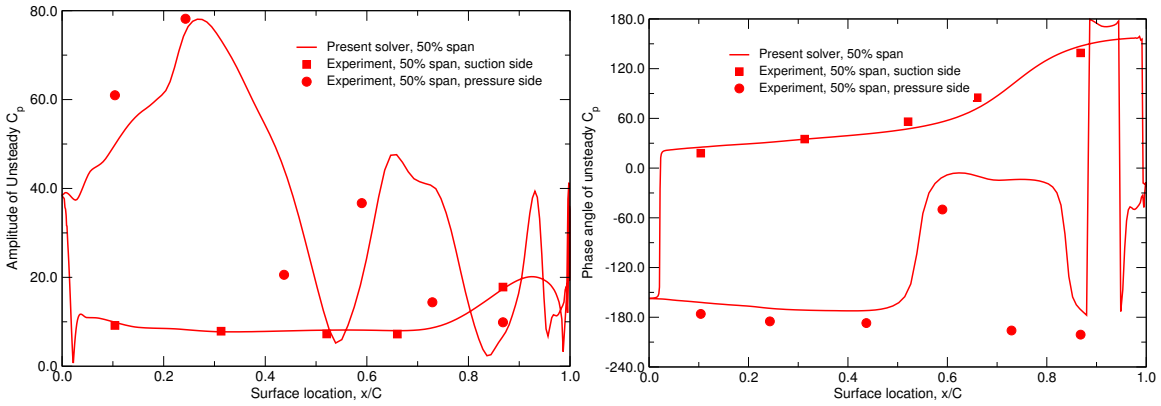


Figure 5.33: Steady state pressure coefficient for the Fourth Standard Configuration.



(a) Amplitude of unsteady pressure

(b) Phase angle of unsteady pressure

Figure 5.34: First harmonic of unsteady pressure coefficients, ω^*=0.1558, σ=180 deg.

5.2 Stabilized HDHB Solutions with Temporal Spectral Viscosity

In this section, the TSV method is applied to two model problems for which the original HDHB method encounters stability issues. Furthermore, the TSV method is also applied to a stable HDHB case to demonstrate the accuracy of the proposed method.

5.2.1 Stabilized HDHB for the Duffing Equation

In the section, the time-domain HDHB formulation of the Duffing equation[110] is expanded into the frequency domain to demonstrate the existence of aliasing errors. A numerical investigation for a strongly nonlinear case is then performed using HDHB with and without the temporal spectral viscosity. Both stable and unstable physical solutions are accurately predicted with this modified HDHB method.

Nonlinear Duffing equation models a driven spring-mass system with a nonlinear stiffening spring and is given by

$$\ddot{x} + 2\zeta\dot{x} + x + x^3 = F sin(\omega t), \tag{5.3}$$

where x is the non-dimensional displacement, ζ is the damping ratio, F is the non-dimensional forcing amplitude, ω is the non-dimensional excitation frequency and t is the non-dimensional time. By casting into the state-space form, Eq. (5.3) can be

rewritten as a system of first order ODEs, i.e,

$$\frac{\mathrm{d}\mathbf{X}}{\mathrm{d}t} + \mathbf{R}(\mathbf{X}) = 0, \tag{5.4}$$

where

$$\mathbf{X} = \left\{ \begin{array}{c} x \\ \dot{x} \end{array} \right\}, \mathbf{R} = \left\{ \begin{array}{c} -\dot{x} \\ 2\zeta\dot{x} + x + x^3 - Fsin(\omega t) \end{array} \right\}. \tag{5.5}$$

The above equations can be solved by both the classical harmonic balance method and the high-dimensional harmonic balance method.

For simplicity, only the first harmonic systems, denoted as HB1 and HDHB1, are expanded in frequency formulation for comparison. In HB1, the solution is approximated as

$$x(t) = \hat{x}_0 + \hat{x}_1 \cos(\omega t) + \hat{x}_2 \sin(\omega t). \tag{5.6}$$

The Fourier expansions of the first and the second order time derivative terms are

$$\dot{x}(t) = -\omega\hat{x}_1 \sin(\omega t) + \omega\hat{x}_2 \cos(\omega t) \tag{5.7}$$

and

$$\ddot{x}(t) = -\omega^2\hat{x}_1 \cos(\omega t) - \omega^2\hat{x}_2 \sin(\omega t). \tag{5.8}$$

The expansion of the cubic term can be written as

$$
\begin{aligned}
x(t)^3 =&(\hat{x}_0 + \hat{x}_1\cos(\omega t) + \hat{x}_2\sin(\omega t))^3 \\
=&\left(\hat{x}_0^2 + \frac{3}{2}(\hat{x}_1^2 + \hat{x}_2^2)\right)\hat{x}_0 + \left(3\hat{x}_0^2 + \frac{3}{4}(\hat{x}_1^2 + \hat{x}_2^2)\right)\hat{x}_1\cos(\omega t) \\
&+ \left(3\hat{x}_0^2 + \frac{3}{4}(\hat{x}_1^2 + \hat{x}_2^2)\right)\hat{x}_2\sin(\omega t) + \frac{3}{2}(\hat{x}_1^2 - \hat{x}_2^2)\hat{x}_0\cos(2\omega t) + 3\hat{x}_0\hat{x}_1\hat{x}_2\sin(2\omega t) \\
&+ \frac{1}{4}(-3\hat{x}_2^2 + \hat{x}_1^2)\hat{x}_1\cos(3\omega t) + \frac{1}{4}(3\hat{x}_1^2 - \hat{x}_2^2)\hat{x}_2\sin(3\omega t).
\end{aligned}
\tag{5.9}
$$

In the classical HB1, the higher harmonic terms, 2ω, 3ω, etc., are all discarded. After substituting all the remaining terms back and grouping, HB1 system leads to three distinct equations as

$$
\begin{aligned}
&\left(1 + \hat{x}_0^2 + \frac{3}{2}(\hat{x}_1^2 + \hat{x}_2^2)\right)\hat{x}_0 = 0 \\
&(1-\omega^2)\hat{x}_1 + 2\zeta\omega\hat{x}_2 + \left(3\hat{x}_0^2 + \frac{3}{4}(\hat{x}_1^2 + \hat{x}_2^2)\right)\hat{x}_1 = 0 \\
&(1-\omega^2)\hat{x}_2 - 2\zeta\omega\hat{x}_1 + \left(3\hat{x}_0^2 + \frac{3}{4}(\hat{x}_1^2 + \hat{x}_2^2)\right)\hat{x}_2 = F.
\end{aligned}
\tag{5.10}
$$

The HDHB1 solution retains every term in Eq (5.9). The coefficients of $\cos(2\omega t)$, $\sin(2\omega t)$, $\cos(3\omega t)$, $\sin(3\omega t)$ are all absorbed by the $\boldsymbol{E}$ matrix. For example, assuming three sub-time level solutions are defined at phase angle(ωt) equal to 0, $\frac{2}{3}\pi$ and $\frac{4}{3}\pi$, it can be shown that $\cos(3\omega t) = 1.0$ and $\sin(3\omega t) = 0.0$. Therefore, when multiplying the $\boldsymbol{E}$ matrix with the nonlinear cubic term Eq (5.9), the coefficient of the $\cos(3\omega t)$ term, $\frac{1}{4}(-3\hat{x}_2^2 + \hat{x}_1^2)\hat{x}_1$, is aliased into the zero harmonic and the coefficients of the

$\sin(3\omega t)$ term disappears in the HDHB1 system. In the same way, we can also find that the $\cos(2\omega t)$ term is aliased into the $\cos(\omega t)$ term and the $\sin(2\omega t)$ term gets aliased into the $\sin(\omega t)$ term with a negative sign. Therefore, the time-spectral HDHB1 system can be transformed into the frequency-domain formulation as (with the phase angle of the three sub-time levels defined at 0, $\frac{2}{3}\pi$ and $\frac{4}{3}\pi$, respectively)

$$\begin{aligned}
&\left(1+\hat{x}_0^2+\frac{3}{2}(\hat{x}_1^2+\hat{x}_2^2)\right)\hat{x}_0+\frac{1}{4}\hat{x}_1^3-\frac{3}{4}\hat{x}_1\hat{x}_2^2=0,\\
&(1-\omega^2)\hat{x}_1+2\zeta\omega\hat{x}_2+\left(3\hat{x}_0^2+\frac{3}{4}(\hat{x}_1^2+\hat{x}_2^2)\right)\hat{x}_1+\frac{3}{2}(\hat{x}_1^2-\hat{x}_2^2)\hat{x}_0=0,\\
&(1-\omega^2)\hat{x}_2-2\zeta\omega\hat{x}_1+\left(3\hat{x}_0^2+\frac{3}{4}(\hat{x}_1^2+\hat{x}_2^2)\right)\hat{x}_2-3\hat{x}_0\hat{x}_1\hat{x}_2=F,
\end{aligned} \tag{5.11}$$

which clearly shows the existence of aliasing. It should be noted that aliasing errors differ from the above form if different phase angles are chosen. Further study of this problem shows that the HDHB always includes more terms than the classical HB system for the same number of harmonics retained in the system.

The Duffing equation has been numerically investigated by Liu et al.[32] using the classical HB and the time-spectral HDHB method for three different responses. It was shown that, for a weak nonlinear case without hysteresis, both methods yield identical solutions. On the other hand, for a highly nonlinear case with a large region of hysteresis, the HDHB method was shown to suffer from stability and convergence problems. Their numerical tests have shown that the aliasing error in the HDHB technique could lead to non-physical solutions in addition to the physical solutions.

After analyzing the difference between the classical HB and the HDHB methods, the strongly nonlinear case used by Liu et al.[32] will be numerically investigated next. More specifically, a damping ratio of $\zeta = 0.1$ and a forcing amplitude of $F = 1.25$ will be investigated using the HDHB method with and without temporal spectral viscosity. Shown in Figure 5.35 is the comparison of the time-accurate and the HDHB1 solutions of the first harmonic amplitude. The HDHB equations are solved by the Newton-Raphson iteration whereas the time-accurate solution is computed using a four stage classical Runge-Kutta method. To capture the hysteresis, the frequency is gradually increased from 0.05 (or decreased from 2.8) with a step size $\Delta\omega = 0.05$, while the previous converged solutions are used as the initial conditions for the next frequency computation. As the frequency increases, the amplitude of the first harmonic eventually increases but drops suddenly from 2.5 to 0.24 near $\omega = 2.40$. When decreasing the frequency, the amplitude of the first harmonic suddenly jumps from 0.74 to 1.78 near $\omega = 1.75$. HDHB1 solution misses the drop phenomenon when the frequency is increased. Therefore, the solutions beyond the $\omega = 2.40$ are non-physical. On the other hand, the jump phenomenon is successfully captured when decreasing the frequency. As explained by Liu. et al[32], HDHB may yield extra non-physical solutions compared to the classical HB method or the time-accurate method because of aliasing errors and our initial computations are consistent with those findings.

In order to apply the temporal spectral viscosity (TSV), it is necessary to retain at least two harmonics in the solver. The viscosity is applied to the second harmonic

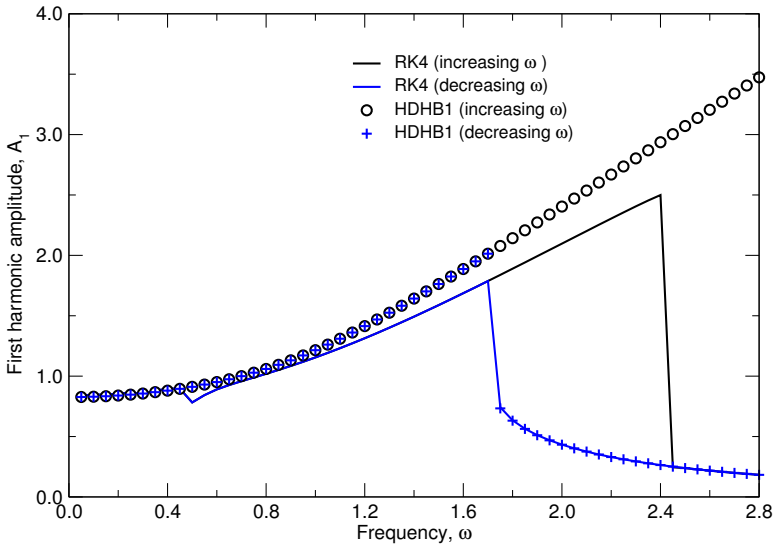
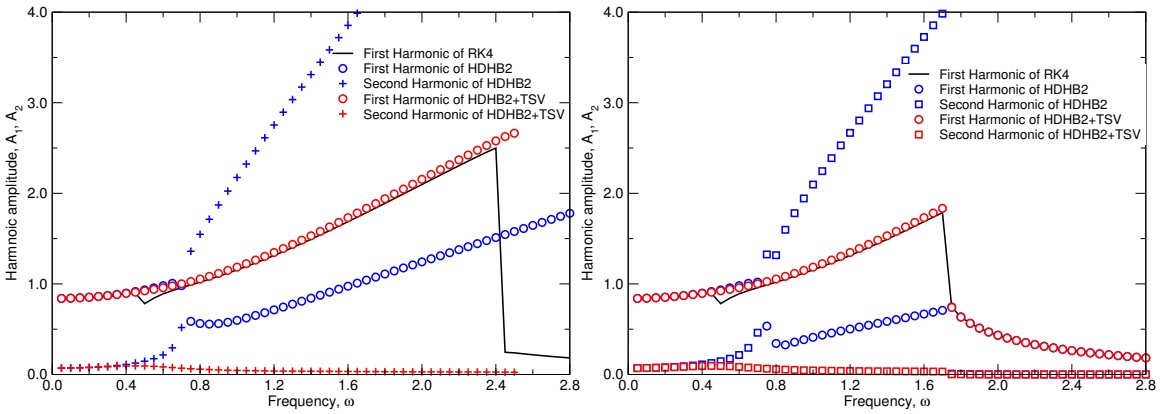


Figure 5.35: Comparison of time-accurate and HDHB1 solutions of the first harmonic amplitude for the Duffing equation.

of HDHB2, while keeping the first harmonic "inviscid". Figure 5.36 compares the first harmonic amplitude of HDHB2 with and without TSV. The original HDHB2 solutions (without the TSV) deviate from the time-accurate solutions substantially in the range $\omega = 0.75$ to $\omega = 2.8$ when increasing frequency and in the range $\omega = 0.75$ to $\omega = 1.75$ when decreasing frequency. The solutions at those regimes are non-physical, identified by the fact that the amplitude of the second harmonic is much greater than that of the first one. On the other hand, the HDHB2 with TSV solutions are in good agreement with the time-accurate solutions.

As can be seen from Figure 5.37, the HDHB3 solution without TSV is not correct. Our HDHB3 solver converges to different solutions with different number of Newton iterations, although the residuals have all converged to the same level (a low level



(a) Increasing ω **(b)** Decreasing ω

Figure 5.36: Comparison of harmonic amplitude of HDHB2 with and without TSV.

limit-cycle, around $1e-13$). Figure 5.37 shows the first harmonic amplitude when the frequency is decreased. It can be seen that HDHB3 gives multiple non-physical solutions from $\omega = 0.5$ to $\omega = 1.75$.

Having investigated the effect of aliasing errors for this case, we now apply the temporal spectral viscosity to the HDHB3 solution. Note that, the TSV is applied to the second and third harmonics and the solution is fully converged to the machine accuracy. It can be seen in Figure 5.38 that the first harmonic amplitude is captured accurately for the most part except for a small region near $\omega = 0.5$. On the other hand, the third harmonic amplitude appears to be heavily damped by the spectral viscosity especially near $\omega = 0.5$.

In order to determine the cause of the problem, we have recomputed the solutions using different viscosity coefficients, ϵ_N. As expected, the accuracy improves with decreased spectral viscosity (see Figure 5.39). Also note that, the viscosity coefficient

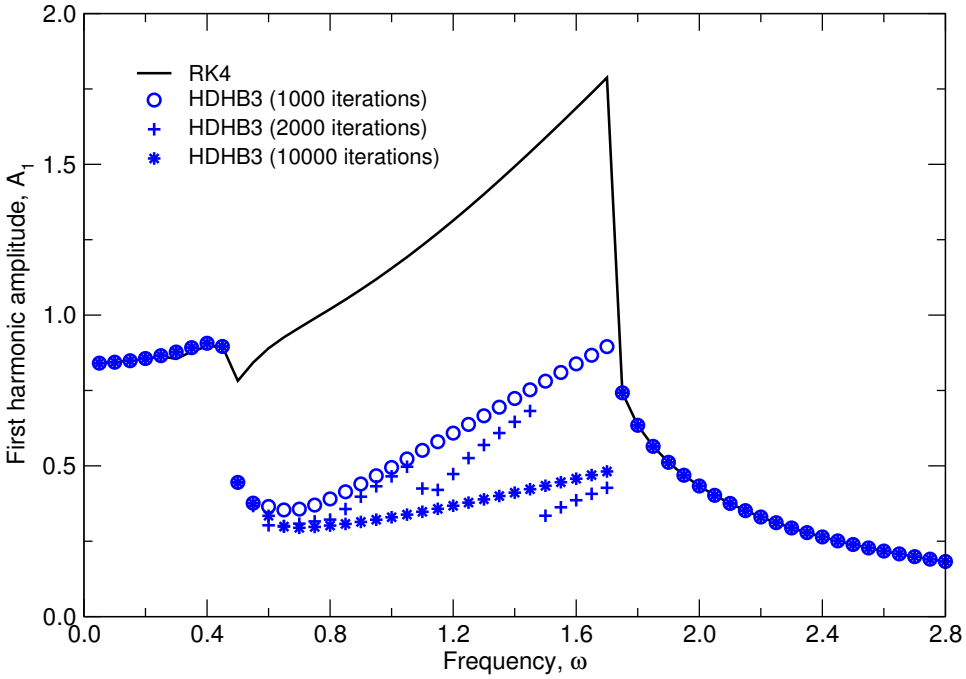
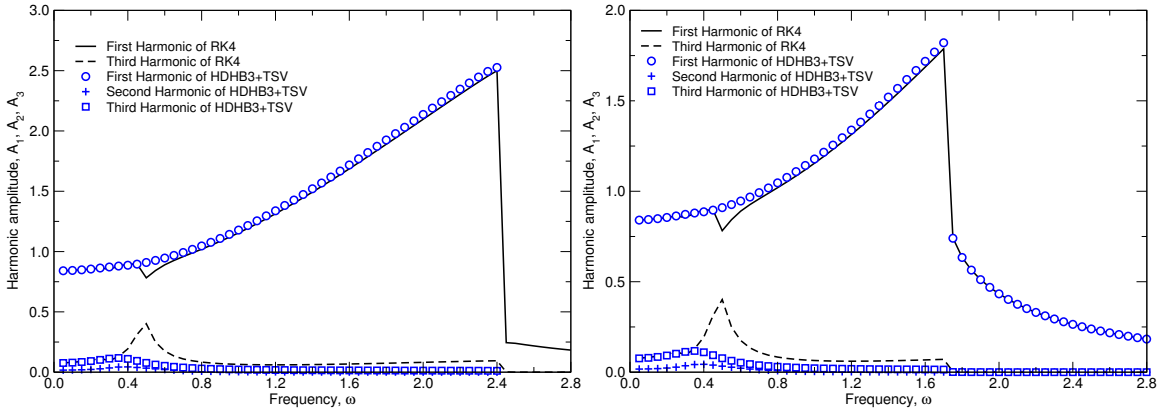


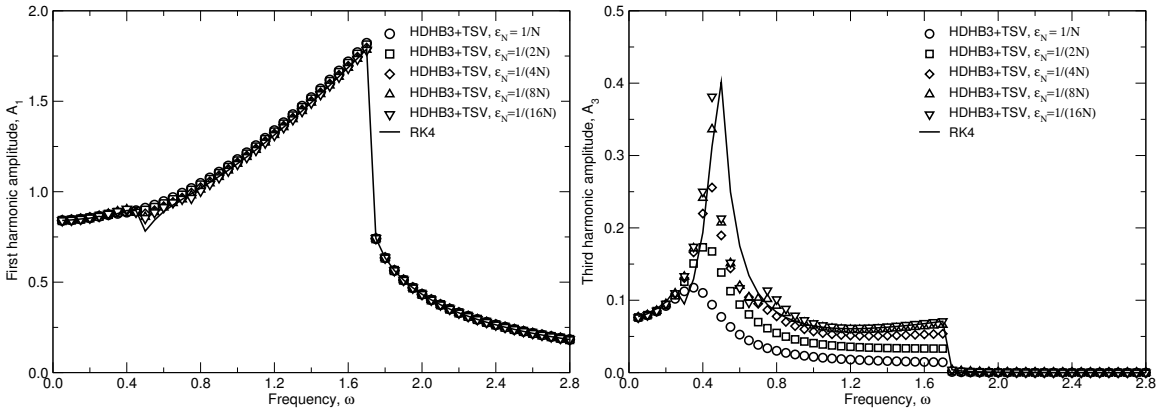
Figure 5.37: Multiple non-physical solutions of HDHB3 without TSV.



(a) Increasing ω **(b)** Decreasing ω

Figure 5.38: Harmonic amplitude of HDHB3 with temporal spectral viscosity.

was further reduced to $\epsilon_N = \frac{1}{32N}$, which lead to non-physical solutions. Therefore, we conclude that a viscosity coefficient between $\frac{1}{4N}$ and $\frac{1}{16N}$ gives acceptable results for this case.



(a) First Hamonic **(b)** Third Harmonic

Figure 5.39: HDHB3 solution using different temporal spectral viscosity coefficients.

Liu et .al[32] have pointed out that retaining more harmonics in an HDHB analysis may help to alleviate the aliasing error side-effects. To verify this, we ran our solver using eight harmonics and were able to obtain a physically correct HDHB8 solution with a very small step size $\Delta\omega = 0.002$, as shown in Figure 5.40. The HDHB8 solution without TSV appears to be in good agreement with the time-accurate solutions, especially at the $\omega = 0.5$ region. However, if a larger step size ($\Delta\omega$) is used, the HDHB8 solver becomes unstable and fails to converge. Therefore, it is required to provide a sufficiently close initial condition to get a physically correct solution without

TSV, even if a large number of harmonics are retained. This may impose a challenge for a complex CFD problem. On the contrary, HDHB8 with a step size $\Delta\omega = 0.05$ and temporal spectral viscosity coefficient $\epsilon_N = \frac{1}{4N}$ yields physically correct solutions without any convergence problems.

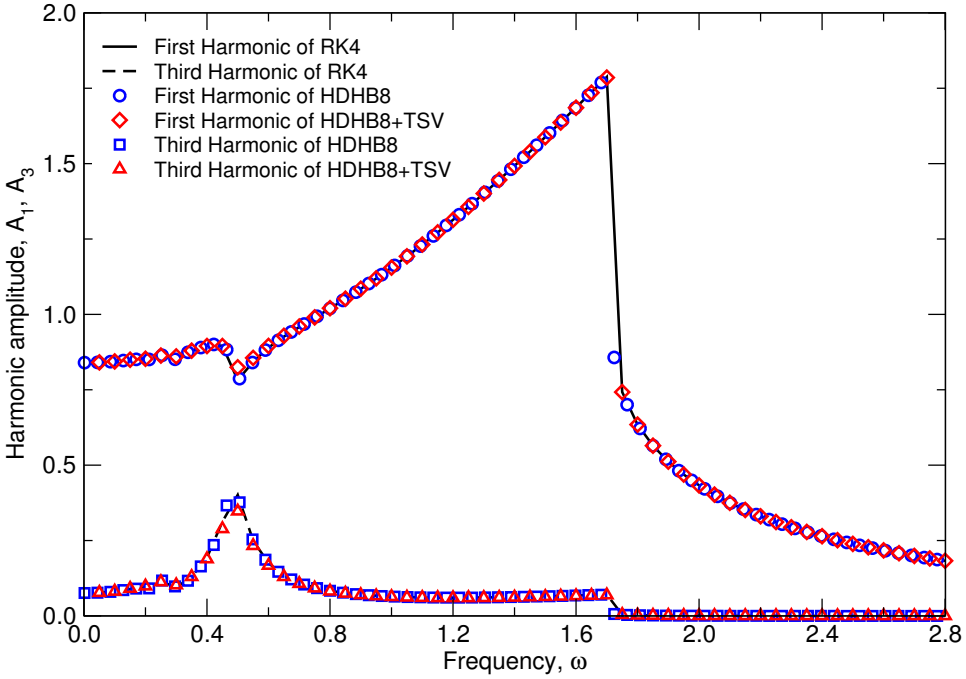


Figure 5.40: Physical correct solutions of HDHB8 without TSV.

Results presented up to this point were all stable solutions. In fact, unstable solutions also exist between the upper branch and the lower branch of the hysteresis. To determine these unstable solutions, a technique proposed by Liu et. al [32] has been implemented herein. The search procedure is as follows. Instead of prescribing the force and the frequency, one prescribes the force and the amplitude of the first

harmonic treating the excitation frequency and the rest of the harmonics as unknowns. To determine the unstable solutions corresponding to the upper branch, we have started with an initial value of $A_1 = 0.9$ and obtained a converged solution for the modified problem. That converged solution is then used as an initial condition for the next amplitude of A_1, which is increased with a step of $\Delta A_1 = 0.05$. Similarly, the unstable solutions corresponding to the lower branch are obtained when an initial value of $A_1 = 0.2$ is used. Solutions for HDHB1 (without TSV) and HDHB2 (with TSV applied to the second harmonic) are shown in Figure 5.41. This demonstrates that both stable and unstable solutions can be determined quite accurately using HDHB2+TSV.

In addition to the harmonic balance method, the second-order backward difference formula (BDF) operator and the second-order central difference formula (CDF) operator are employed to solve the same problem. Numerical experiments show that the second-order BDF is stable for 17, 33 and 65 sub-time level solutions. In contrast, the solver with CDF operator fails to converge for 17 and 33 sub-time level solutions but converges for 65 sub-time levels, which are not shown here. It is found that TSV can stabilize the CDF as well. The solutions from the BDF as well as stabilized CDF are given in Figure 5.42.

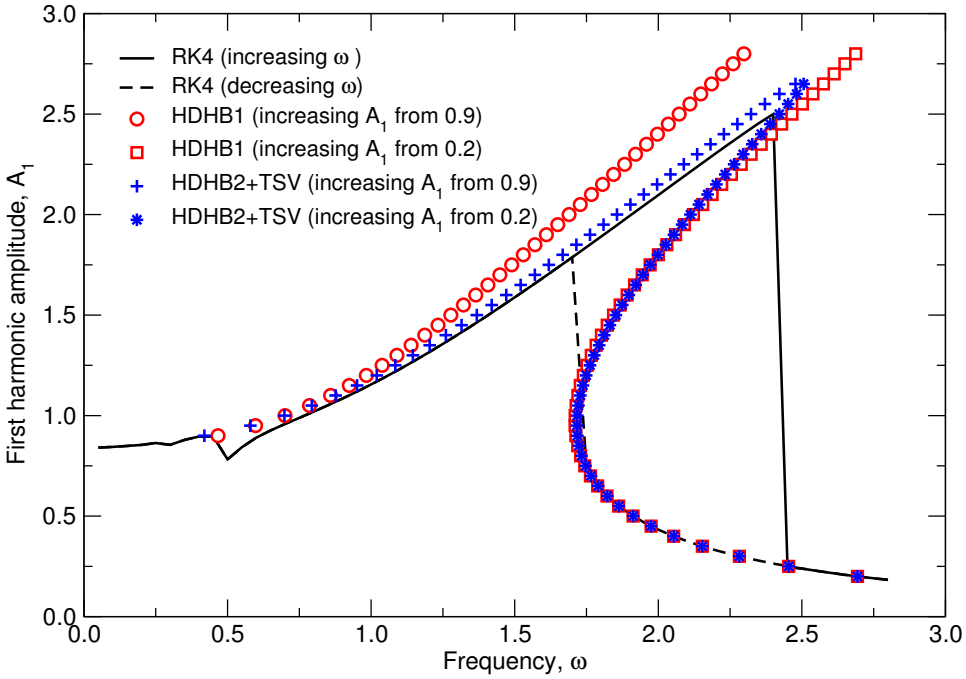
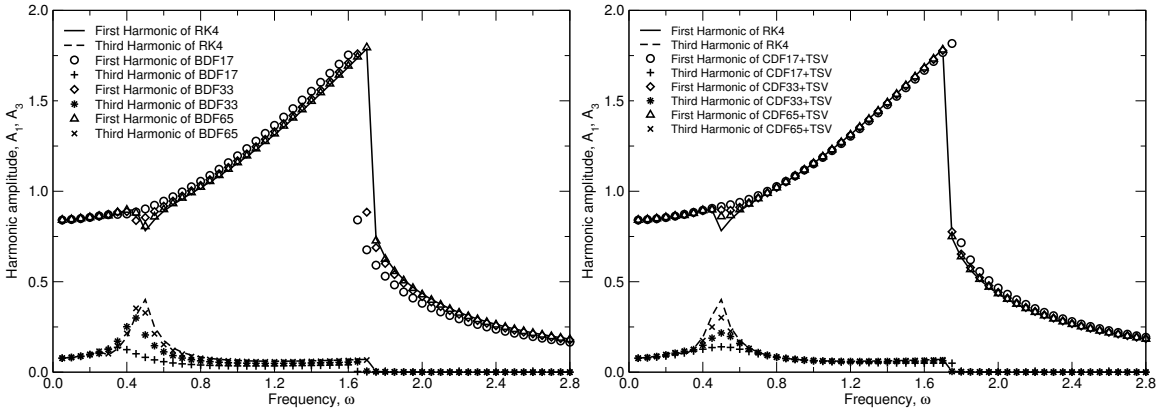


Figure 5.41: Comparison of unstable solutions.



(a) BDF **(b)** Stabilized CDF

Figure 5.42: solutions using BDF and CDF operators

5.2.2 Stabilized HDHB Solutions of Unsteady Flow Around an Oscillating Circular Cylinder

Vortex shedding is a classical flow problem and has a long history of being investigated. The famous Karman vortex street is such a phenomenon. Sieverding and Heinemann[111] experimentally investigated the vortex shedding phenomenon for flat plates and turbine cascades in the subsonic flow regime. They measured the Strouhal number variation with respect to a large range of Mach and Reynolds numbers and demonstrated the influence of the boundary layer state, laminar flow, turbulent flow or transitional flow, on the Strouhal number. In addition, they measured the shedding frequency for different boundary layer states. The spectrum with a sharp peak at a high Reynolds number indicates fully turbulent separation from both of pressure and suction sides. The spectrum becomes extremely wide with two distinct peaks at a moderate Reynolds number. They claim that the pressure side boundary layer flips back and forth between transitional and fully turbulent regimes while the suction side remains of fully turbulent. Bassi et al.[112] performed numerical computations of vortex shedding over a blunt turbine trailing edge using an unsteady RANS solver with $k-\omega$ turbulence model. Despite of large number of vortex shedding cycles, the pressure at the trailing edge does not become periodic. FFT analysis of pressure fluctuations reveals two frequency peaks and a broad spectrum. The author attributed this to the transition in the boundary layer. Note that, in the current form, multiple

frequency cases are not applicable to the harmonic balance solver developed in this work.

In this section, the temporal spectral viscosity is applied to stabilize an HDHB CFD solver. Unsteady laminar flow over a stationary circular cylinder at low Reynolds numbers ($50 < Re < 180$) has been investigated using the HDHB method in the past[15–17]. For a stationary cylinder, since the shedding frequency is unknown *a priori*, investigators have developed frequency search techniques based on the phase angle interpolation method[16] or a gradient-based approach[15]. However, we have attempted to compute the unsteady flow over a stationary circular cylinder with $Re > 200$ without success in our HDHB CFD solver. For this flow regime, the flow fields become three-dimensional and irregular as $Re > 200$ and aliasing errors originating from strong nonlinearity trigger the instability of the HDHB CFD solver. Spiker[113] also reported a similar instability when modeling flow over an oscillating cylinder associated with retaining more than three harmonics. She proposed to filter out higher harmonics at the far-field region to stabilize the solver.

In order the eliminate the effects of frequency search, we consider an oscillating cylinder case for which the shedding frequency is locked onto the forced vibration frequency. The test case was also numerically investigated by Blackburn and Henderson[114] and Pedro et al.[115] using a time-accurate method. The circular cylinder is assumed to harmonically vibrate in the translational direction with the amplitude of 25% of the cylinder diameter, and the ratio of the vibration frequency to the shedding frequency is 0.85, which results in a Strouhal number of 0.1995. The

Reynolds number based on the inlet flow conditions and the cylinder diameter is 500. Although the wake of a cylinder is three-dimensional and becomes irregular at Re=500, the goal of this high Reynolds number case is to demonstrate the stabilization capability and accuracy of the proposed spectral operator. Figure 5.43 shows a close up look at the O-block grid used in the paper. The grid consists of 361 nodes in the circumferential direction and 257 nodes in the normal direction and extends about 50 diameters away from the cylinder wall surface. The governing equations are discretised by a vertex-based finite volume method proposed by Jameson[4]. A modified local time stepping[23] and multigrid technique are employed to accelerate the convergence rate. Riemann boundary conditions are applied in the time-domain for each sub-time level solution. Since the present code is a compressible CFD solver, the inlet Mach number is set to be 0.1 to minimize the compressibility effects.

First, the lift and drag coefficients over one vibration period are plotted in Figure 5.44. To investigate mode convergence and the accuracy of the HDHB method, we also present results from our time-accurate solver, in which the time-derivative term is approximated by a second-order backward difference operator. The slow harmonic mode convergence rate could be ascribed to the highly nonlinear nature of the flow and the added spectral viscosity. In order to retain the spectral accuracy, as discussed before, it is critical to minimize the added spectral viscosity. However, it is found by numerical tests that if the spectral viscosity coefficients for all harmonics are reduced at the same time, the method may fail to stabilize the CFD solver. Because the lower harmonic content is more important than the higher harmonic counterpart,

we only decrease the second harmonic coefficient $\epsilon_N = \frac{1}{4N}$, while leaving the third harmonic and higher harmonics to be $\epsilon_N = \frac{1}{N}$ to ensure convergence. It can be seen from Figure 5.44 that the reduced TSV HDHB11 and HDHB15 solutions are in good agreement with the time-accurate solutions. The maximum C_L and time-averaged C_D, shown in Table 5.3, for the HDHB15 with reduced TSV compares fairly well with the numerical solutions reported by other researchers[114, 115].

Table 5.3: Comparison of the force coefficients.

	Maximum C_L	Time-averaged C_D
Present Solver: HDHB	0.664	1.504
Present Solver: Time-accurate	0.645	1.505
Blackburn and Henderson[114]	0.72	1.46
Pedro et al.[115]	0.67	1.35

Next, we qualitatively compare the results obtained from four different runs, namely: HDHB7+TSV, HDHB11 +TSV, time-accurate and results from Blackburn and Henderson[114]. The four sets of figures consist of five instantaneous vortex plots equally spanned over half a vibration cycle, starting with the cylinder in the most upper position and ending with the cylinder in the lowest position. It can be seen that there is good agreement among all solutions. The HDHB7+TSV solution appears to be less accurate due to the lack of mode convergence. Our HDHB11+TSV solution seems to be in good agreement with Blackburn and Henderson[114] as well as our

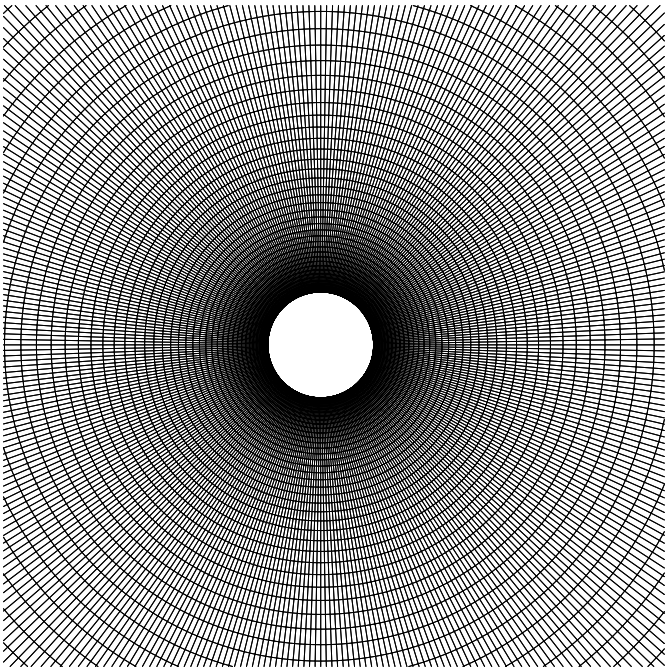
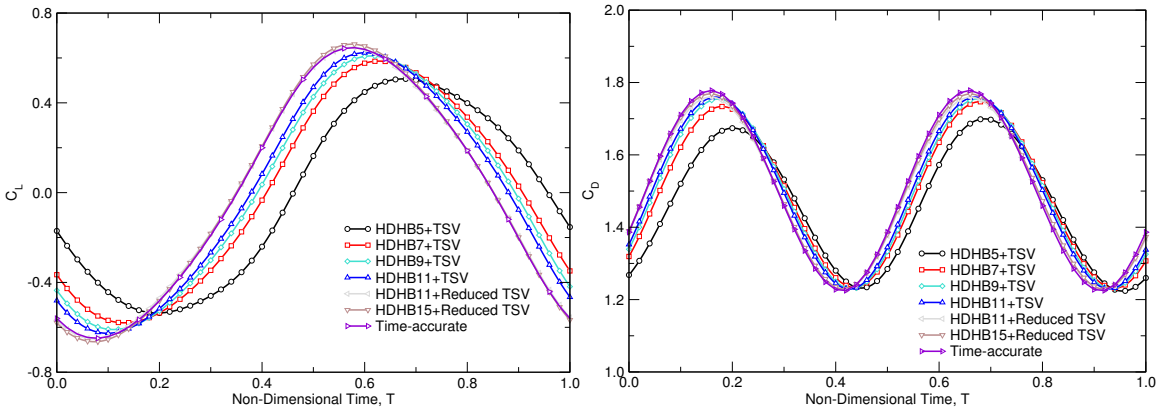


Figure 5.43: Computational grid for a circular cylinder.

time-accurate solution, although there are minor but visible differences in contour plots.

Finally, the convergence history for different numbers of harmonics is shown in Figure 5.46. All the solutions start from the same initial condition. Three-levels of multigrid are employed to speed up the convergence. The convergence rate for the stabilized HDHB solvers are almost identical. On the contrary, the original method without TSV fails to converge. The computational time reuqirements for the stabilized harmonic balance solver and the time-accurate solver are summarized in Table 5.4. All solvers have converged to a residual of 10^{-10}.



(a) Lift coefficient **(b)** Drag coefficient

Figure 5.44: Force coefficients over one vibration cycle with different harmonics. $Re = 500$, $Ma = 0.1$.

Twenty vibration cycles have been executed in the time-accurate solver in order to reach a temporal periodic flow solution. In practice, it is desirable to restart a higher harmonic computation from a converged lower harmonic computation to improve the computational efficiency. First, the converged time domain solution with n harmonics is transferred to Fourier coefficients using $\mathbf{E}_n$ matrix. Then, the higher Fourier coefficients are assumed to be zero. Finally, frequency domain solutions are transferred back into expanded $(2m + 1)$ sub-time level solutions using $\mathbf{E}_m^{-1}$ matrix $(n < m)$. It is very efficient to use this restart strategy to perform the mode convergence study.

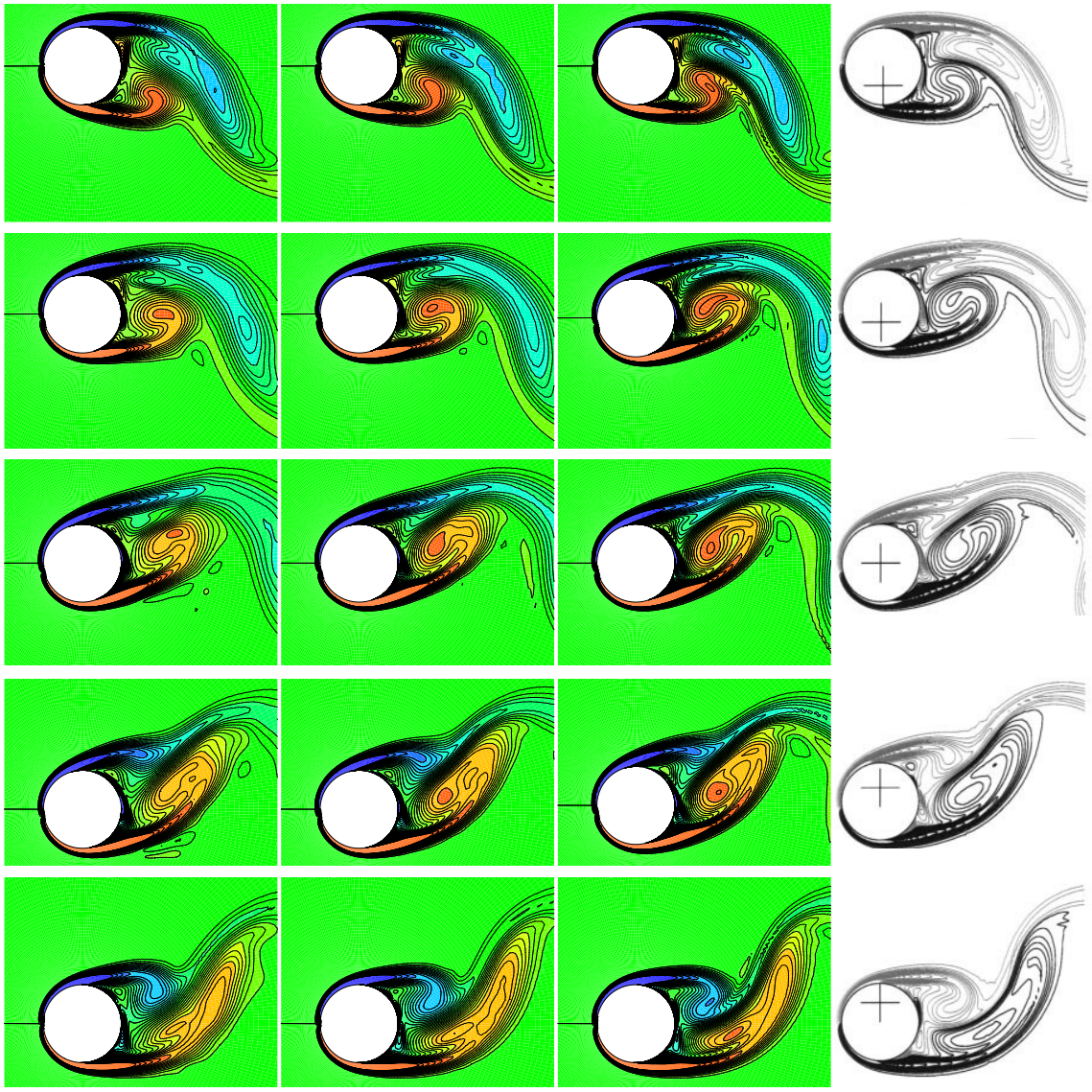


Figure 5.45: Instantaneous vortex contours over half a vibration cycle, Left: HDHB7+TSV, Middle Left: HDHB11+TSV, Middle Right: Time-accurate, Right: Blackburn and Henderson. (reproduced with permission). $Re = 500$, $Ma = 0.1$.

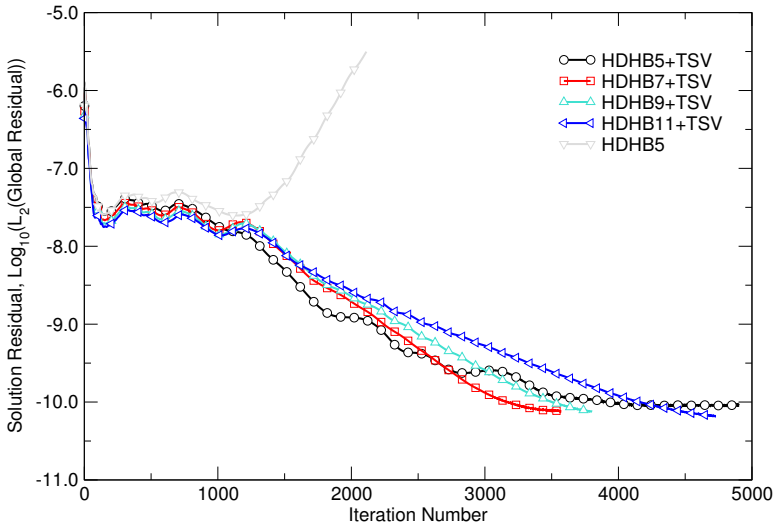


Figure 5.46: Convergence history for HDHB solver with different number of harmonics.

Table 5.4: Comparison of HDHB computational time.

Method	Computational Time (mins)
HDHB5	206
HDHB7	306
HDHB9	416
HDHB11	537
Time-accurate	843

5.2.3 Effect of Temporal Spectral Viscosity on the Accuracy of Stable Unsteady Solutions

In this section, we revisit the Eleventh Standard Configuration. In the experiments, the blades were forced to undergo a plunging motion (normal to the chord) with a reduced frequency of 0.309 (based on the exit velocity). Here we compute a nonlinear response to a 5% chord plunging motion using the HDHB technique. A "mode convergence" study was performed and five harmonics was found to be adequate in an earlier section.

It must be noted that we have not encountered any instability issues for this test case and the main objective here is to investigate the effect that the spectral viscosity has on the accuracy of the converged stable unsteady solutions. Figure 5.47 shows the mean surface pressure distribution for different temporal viscosity coefficients. As expected, the zeroth harmonic solutions are identical since the temporal viscosity is only applied to the second, third, fourth, and fifth harmonics while treating the first and zeroth harmonics to be "inviscid".

Next, we plot the imaginary part of the first and the second harmonics of unsteady pressure distribution in Figure 5.48. The discrepancy among these solutions is negligible for the viscosity coefficient parameter range $\epsilon_N = \frac{1}{N} \sim \frac{1}{8N}$, demonstrating that the proposed temporal viscosity method retains a high spectral accuracy. Also note that, unlike the Duffing oscillator problem or vortex shedding problem presented earlier, this problem appears to be "less" nonlinear since the higher harmonics (and

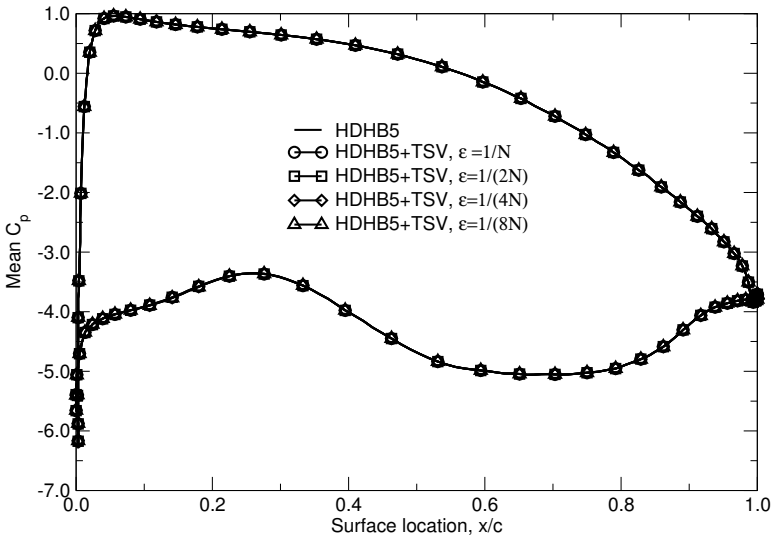


Figure 5.47: Mean pressure coefficient distribution for the Eleventh Standard Configuration, ω^*=0.309, σ=180 deg.

the spectral viscosity applied to those harmonics) do not significantly affect the first and the zeroth harmonic solutions.

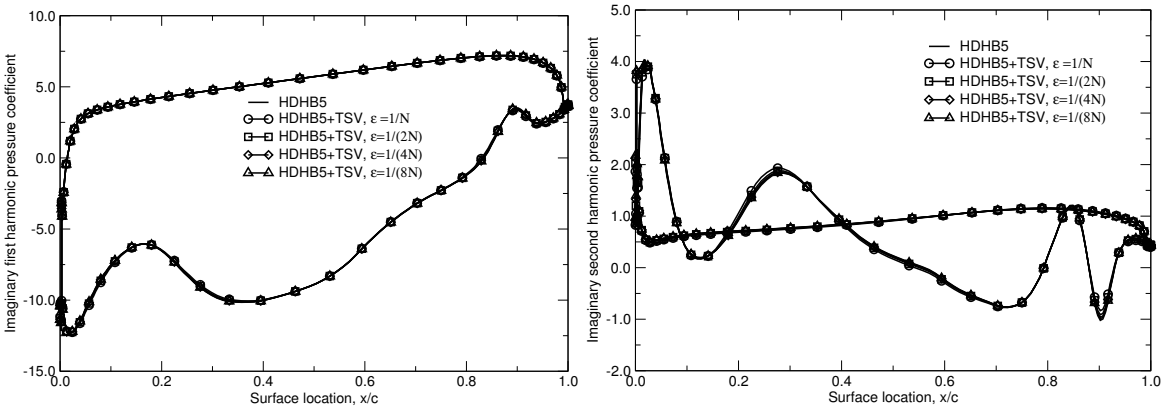


Figure 5.48: Imaginary part of the first harmonic (left) and the second harmonic (right) of surface pressure coefficient for the Eleventh Standard Configuration, ω^*=0.309, σ=180 deg.

5.3 Aerodynamic Shape Optimization

In this section, solutions for aerodynamic shape optimization are presented. First, a quasi-one-dimensional steady case is presented. Then, the methodology is generalized to two-dimensional steady and unsteady cases.

5.3.1 Inverse Design for a Steady Quasi-One-Dimensional Nozzle

To validate the optimization framework, an inverse design of quasi-one-dimensional inviscid compressible flow through a convergent-divergent nozzle with a shock is investigated in this section. The governing equation and its numerical solution are well-documented in Anderson's book[116]. The governing equations are discretised by the finite difference method using MacCormack's time-marching scheme[117] with a second-order artificial viscosity to damp oscillations around shocks. The cross section area of the target nozzle shape is defined as

$$A = 1 + 2.2(x - 1.5)^2, 0 \leq x \leq 3,$$

and is shown as the black line in Figure 5.49. The inlet/exit pressure ratio is, $P_e/P_o = 0.6784$. The target pressure distribution for the target nozzle is plotted in Figure 5.50 as the black line, which is in good agreement with Anderson's solution.

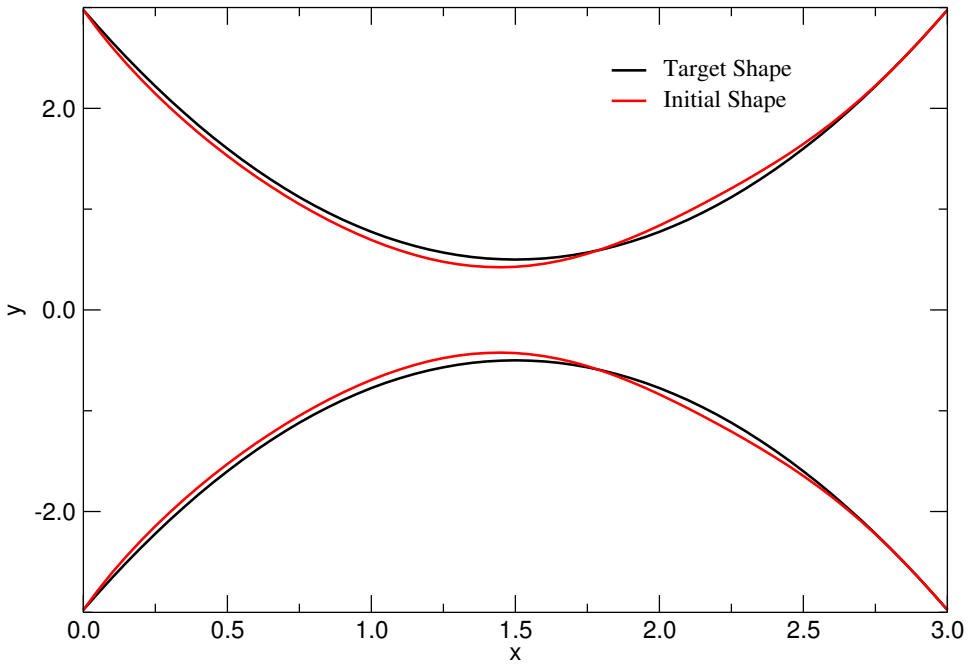


Figure 5.49: Initial and target nozzle shape.

After validating the simple CFD code, we proceed to the adjoint optimization solver. Rather than choosing the cross section area, we chose the Hicks-Henne bump function[88] as the design variable because the cross section area could potentially introduce non-smooth area variations during the optimization. The Hicks-Henne bump functions are infinitely differentiable, the smoothness of the shape is easily guaranteed. The bump function is defined as

$$b_i(x) = a \sin^s \left(\pi x^{\frac{log_{10}5}{log_{10}t_i}} \right),$$

where a determines the maximum bump height, t_i determines the location of the maximum bump and s determines the bump width. Figure 5.51 shows a series of

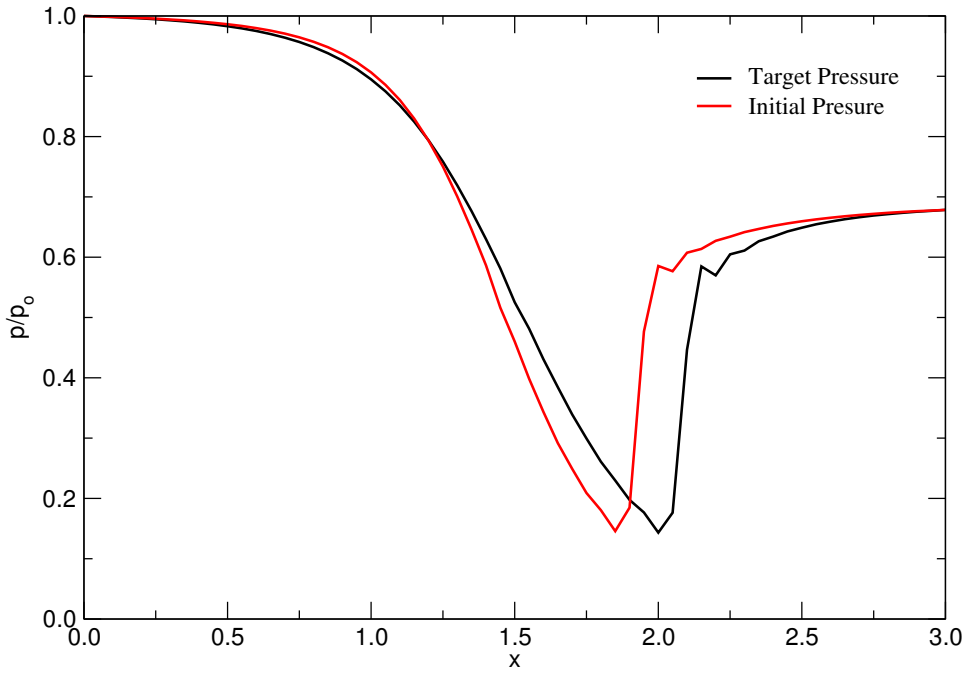


Figure 5.50: Initial and target nozzle pressure distribution.

Hicks-Henne functions. In this work, we have chosen a total of nine Hicks-Henne functions with t_i equally spaced within $0 \leq x \leq 1$. The bump function amplitude a is picked as the design variable. The main disadvantage of using the Hicks-Henne functions for inverse design is that they may not form a complete design space and they are not orthogonal. Therefore, the function itself is used to perturb the target shape so that the target shape is obtainable. The perturbation function is chosen as

$$P(x) = -0.15\sin^4\left(\pi x^{\frac{log_{10}5}{log_{10}0.1}}\right) - 0.2\sin^4\left(\pi x^{\frac{log_{10}5}{log_{10}0.5}}\right) + 0.25\sin^4\left(\pi x^{\frac{log_{10}5}{log_{10}0.7}}\right).$$

The initial shape and the initial solution for the pressure distribution are plotted as a red line in Figure 5.49 and Figure 5.50, respectively. The objective function is defined

as

$$I = \frac{1}{2}\int_s (p - p_{target})^2 \, \mathrm{d}s. \tag{5.12}$$

Both L-BFGS and gradient descent methods are employed to optimize the shape. Shown in Figure 5.52 is the optimization convergence history. After one hundred design cycles, the residual of the L-BFGS method drops eight orders of magnitude, while only three orders of magnitude decrease is achieved by the gradient descent method. The target shape and the pressure distribution, as shown in Figure 5.53 and Figure 5.54, are recovered by the L-BFGS method more efficiently.

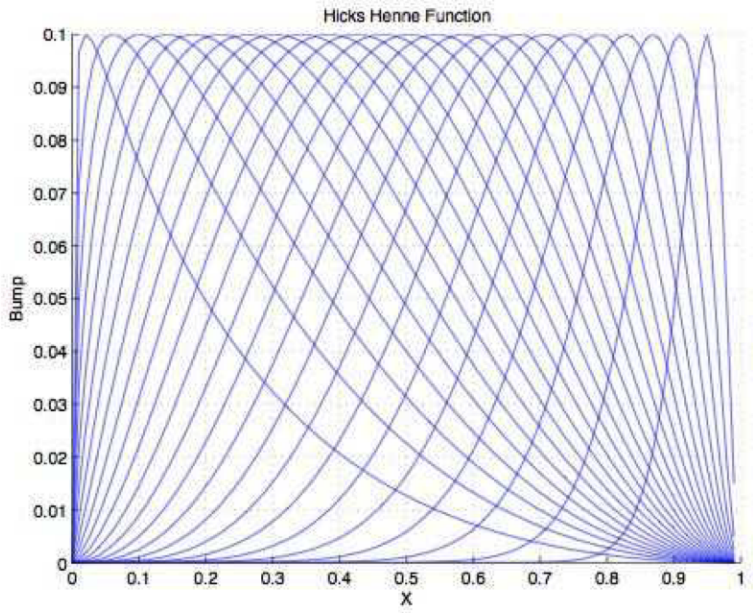


Figure 5.51: A series of Hicks-Henne function.

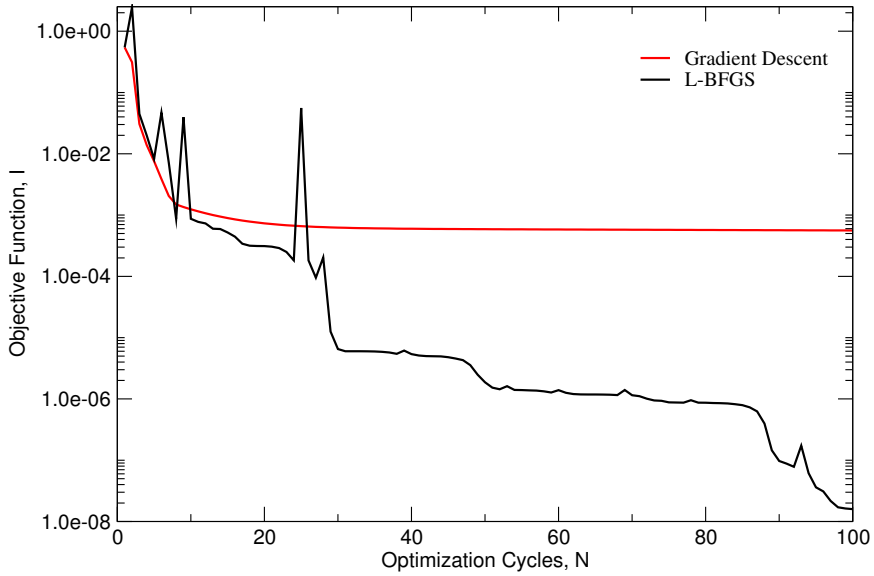


Figure 5.52: Convergence history for inverse design of nozzle.

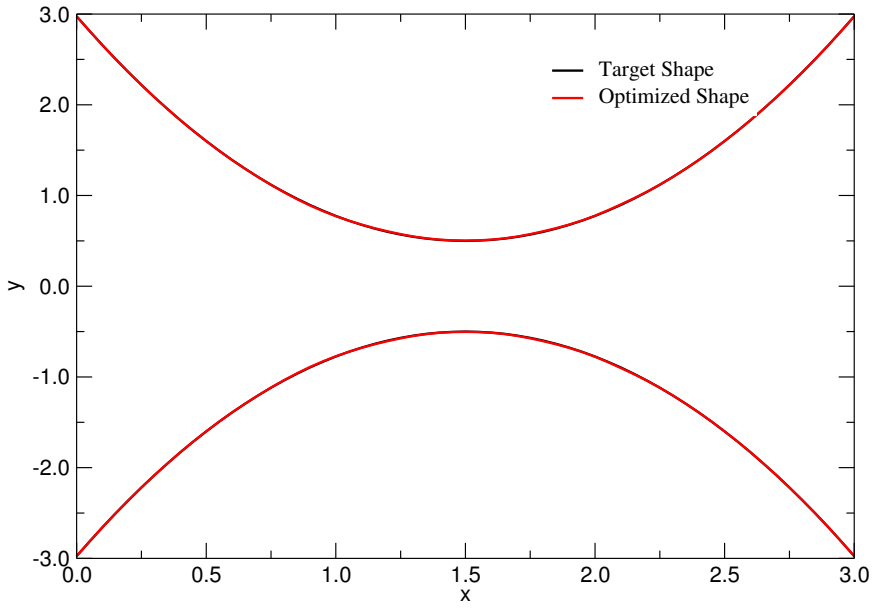


Figure 5.53: Optimized and target nozzle shape.

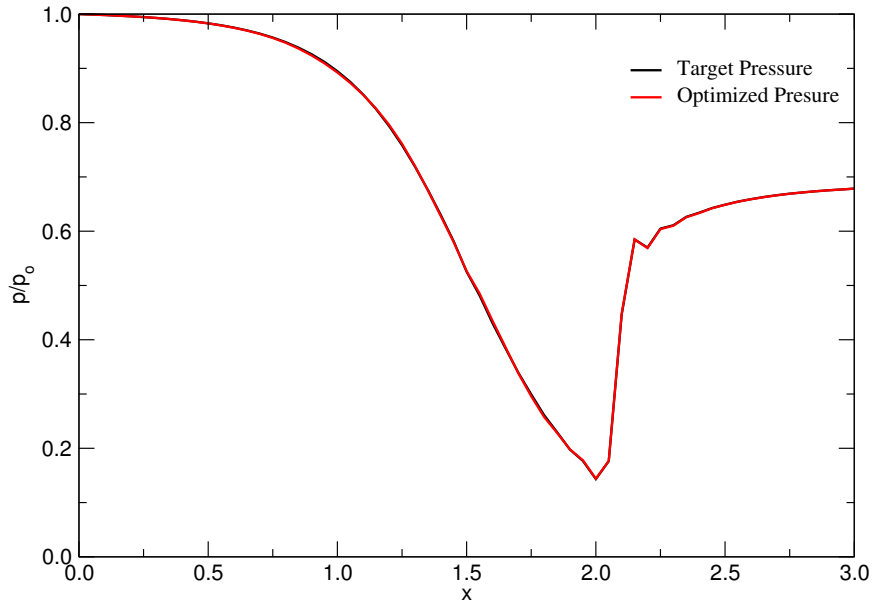


Figure 5.54: Optimized and target nozzle pressure distribution.

5.3.2 Inverse Design for Steady Tenth Standard Configuration

With the confidence of the successful quasi-one-dimensional inverse design case, the research focus is turned to inverse design problems of a two-dimensional turbomachinery cascade. The motivation is to reach the target Tenth Standard Configuration geometry by minimizing the blade surface pressure distribution difference between the initial and target cascades. First, we consider one of the cases also studied by Wu et al.[118]. The pressure distribution of the transonic flow condition is chosen as the target pressure. The initial shape is a deformed Tenth Standard Configuration, superposed by of a sine wave with amplitude of 1% chord length on both pressure and suction sides. To show the geometry clearly, the cascade chord line is aligned with the x axis in Figure 5.55. A series of twenty-four Hicks-Henne functions are equally spaced along the axial chord direction for both pressure and suction sides. Before the adjoint solver is incorporated into an optimization solver, the sensitivities are verified by a finite difference approach. In this work, the second-order central difference method is employed. Therefore forty-eight flow field computations have to be performed to evaluate the derivatives. Thus, the computational cost of the finite difference method is prohibitive compared to the adjoint method. Shown in Figure 5.56 is the convergence history for the inverse design of Tenth Standard Configuration. Using the L-BFGS algorithm, it can be seen that the cost function reaches its limitation at

the 20th optimization cycle. The optimized pressure distribution, as well as initial and target solutions (at the 25th optimization cycle), are plotted in Figure 5.57.

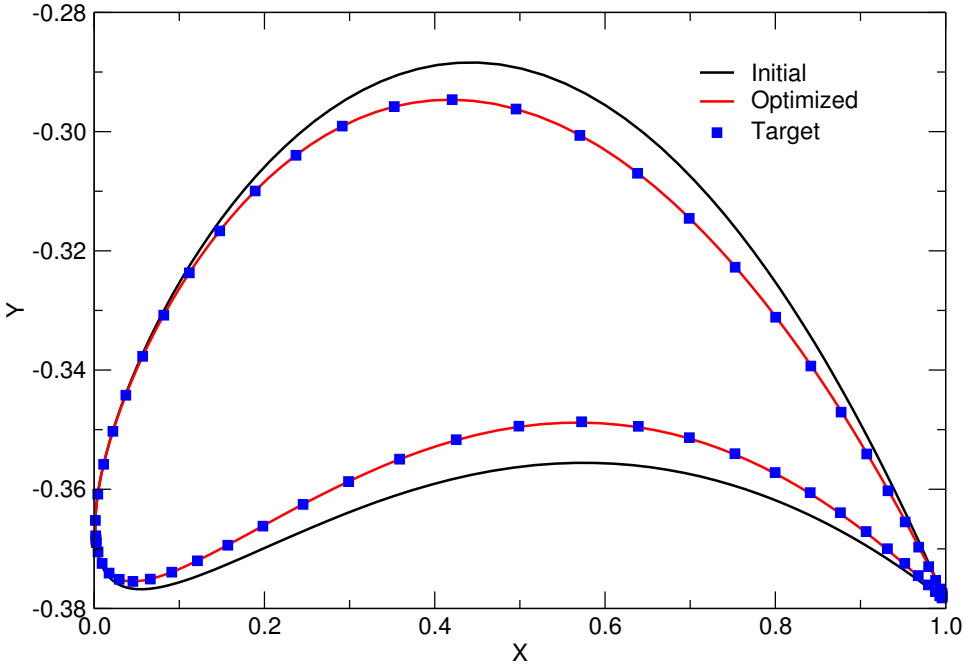


Figure 5.55: Comparison of the blade shapes for the Tenth Standard Configuration.

Despite the fact that the target geometry is obtained by the forty-eight Hicks-Henne functions, the stall of the cost function residual indicates that the design variables do not form a complete design space for this case. Next, we construct the initial geometry using Hicks-Henne function perturbations. The solutions are plotted in Figure 5.58. Although the initial shape deviates further from the target shape, the cost function drops at least five orders of magnitude after 30 design cycles. However,

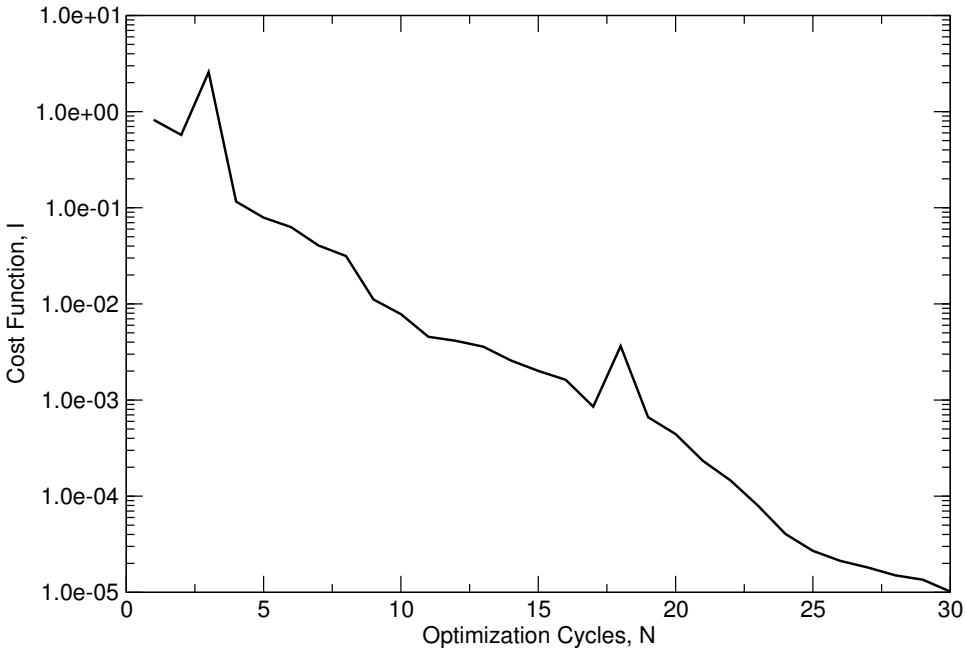


Figure 5.56: Convergence history for inverse design of the Ten Standard Configuration.

it is difficult to form a complete design space for an arbitrary initial airfoil using the Hicks-Henne functions.

Having shown the drawbacks of the use of Hicks-Henne functions for inverse design problems, mesh points as design variables are going to be investigated alternatively. In contrast to the Hicks-Henne approach, theoretically, the mesh point method can provide a complete space of design. However, it requires additional smoothing techniques to ensure the continuity of the blade geometry. Jameson and his colleagues[119–121] have applied the Sobolev inner product to smooth the gradients implicitly before applying them to a steepest descent optimization solver. In the literature, the smoothed gradients have not been applied to quasi-Newton methods.

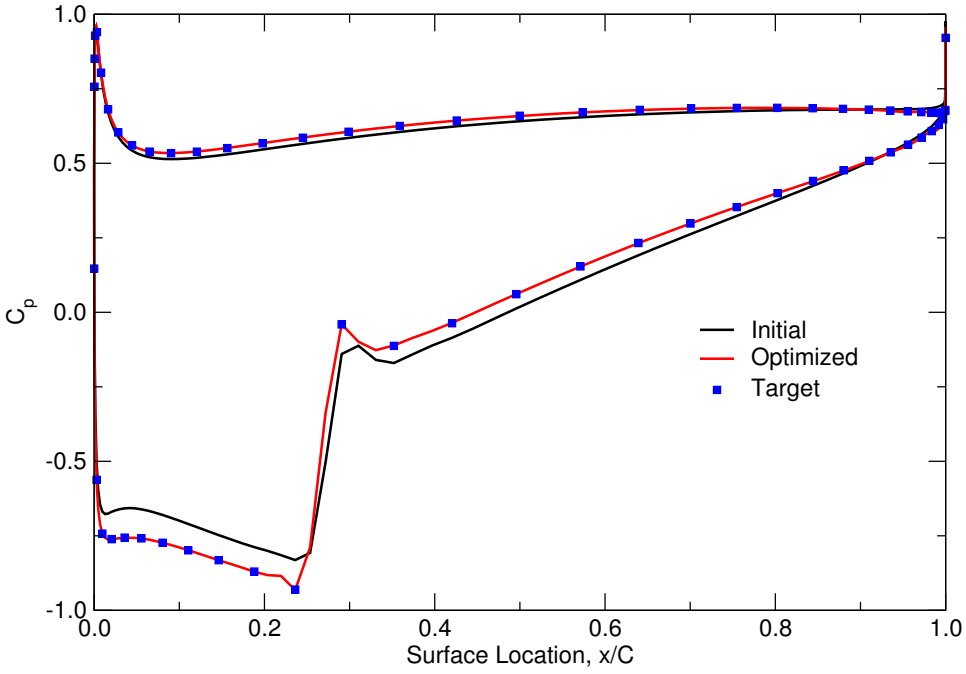
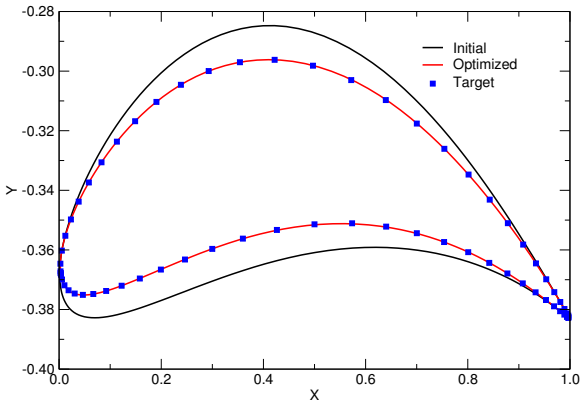
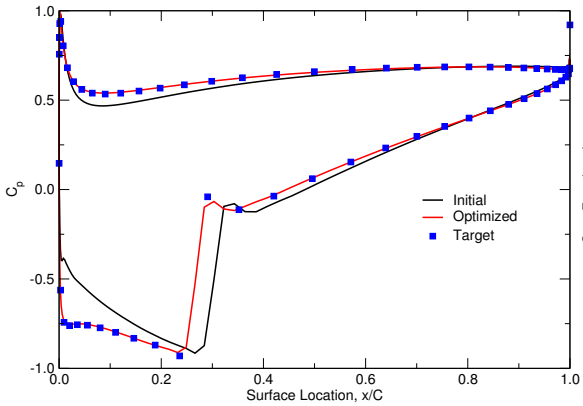


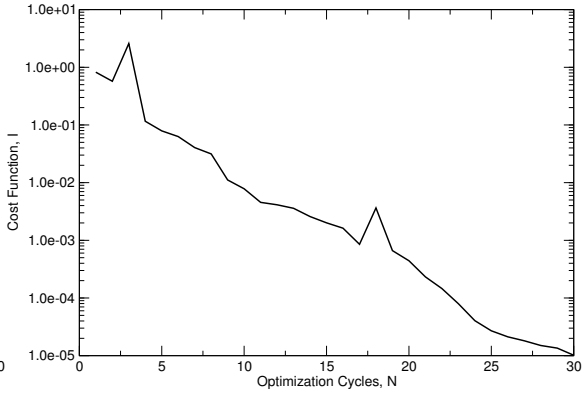
Figure 5.57: Comparison between the optimized and the target geometry and pressure.



(a) Blade Shape



(b) Pressure Distirbution



(c) Convergence history of the cost function

Figure 5.58: Inverse design for the Tenth Standard Configuration, Case 2.

Because of the inaccuracy of the smoothed gradients, we also experienced difficulty in generalizing the method for the L-BFGS algorithm.

A new smoothing procedure is proposed in the dissertation as follows. Rather than directly perturbing each mesh point at the blade surface by the design variables, Y, they are first smoothed by a technique similar to the implicit residual smoothing,

$$\bar{Y} - \frac{\partial}{\partial \xi} \epsilon \frac{\partial}{\partial \xi} \bar{Y} = Y, \tag{5.13}$$

where ϵ is the smoothing parameter. Then the smoothed design variables, $\bar{Y}$, are used to perturb each mesh point at the blade surface. The new approach guarantees the smoothness of the blade geometry and avoids the gradient smoothing as well. To validate this method, the NACA2408 airfoil is chosen as the initial geometry and the surface pressure distribution of the Tenth Standard Configuration at the subsonic flow condition is chosen as the target pressure. For this specific flow condition, the CFD solver fails to converge for a symmetric airfoil, such as a NACA0012 airfoil. After a few trial and errors, it is found that a chamber line airfoil such as a NACA2408 airfoil could obtain a converged CFD solution. The initial computational grid for the NACA2408 airfoil is plotted in Figure 5.59. It consists of 193 design variables for each grid node on the blade surface. The comparison of the sensitivities (i.e. gradients of the objective function with respect to the design variables) at the first optimization step for the NACA2408 airfoil geometry, is plotted in Figure 5.60 and Figure 5.61 for the proposed smoothing method (with $\epsilon = 100$) and unsmoothed method. It is clearly seen that this method produces smooth sensitivities. Having computed changes in the design variable, Y, from the L-BFGS algorithm, the y coordinate of each mesh point of the NACA2408 airfoil is perturbed by smoothed design variables, $\bar{Y}$. After 50 design cycles, the cost function drops more than three orders of magnitude as shown in Figure 5.62. Comparison of the pressure distribution and the geometry shape at the end of optimization are given in Figure 5.63. Both the blade geometry and the pressure distribution are recovered after 50 design cycles. Compared to the optimization of Wu et al.[118], who used a smoothed steepest descent method, the

present technique appears to have improved convergence rate and accuracy. Next, the Mach number contours and the static pressure contours are plotted in Figure 5.64 and Figure 5.65, respectively, which also show good agreement between the optimized and the target geometries. A shock forms near the pressure side leading edge for the NACA2408 airfoil at the subsonic inflow condition for Tenth Standard Configuration. Finally, the convergence history of the adjoint solver together with the CFD solver is shown in Figure 5.66. As can be seen, the adjoint solver has the same convergence rate as the CFD solver.

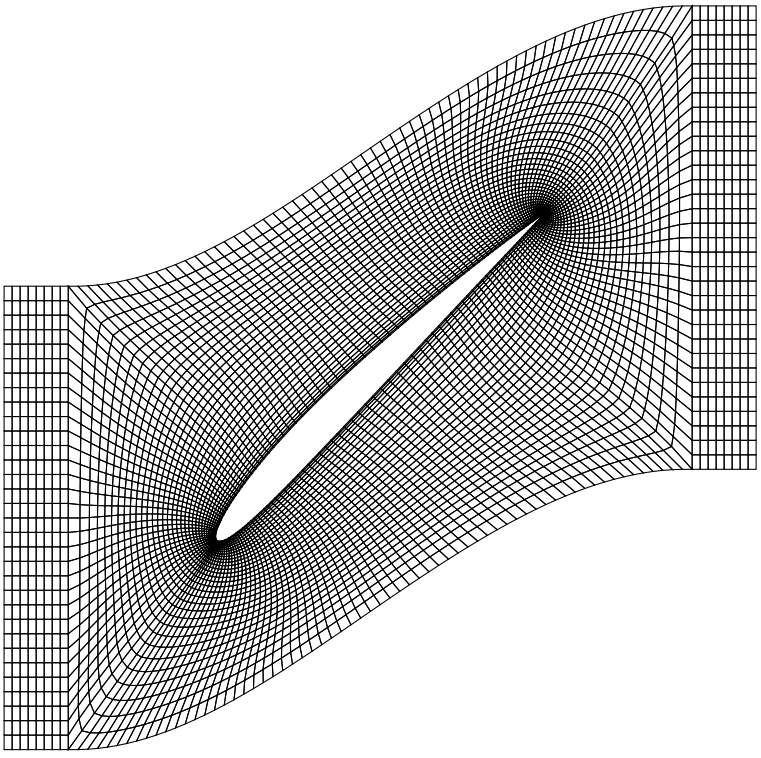


Figure 5.59: Computational grid for the NACA2408 airfoil.

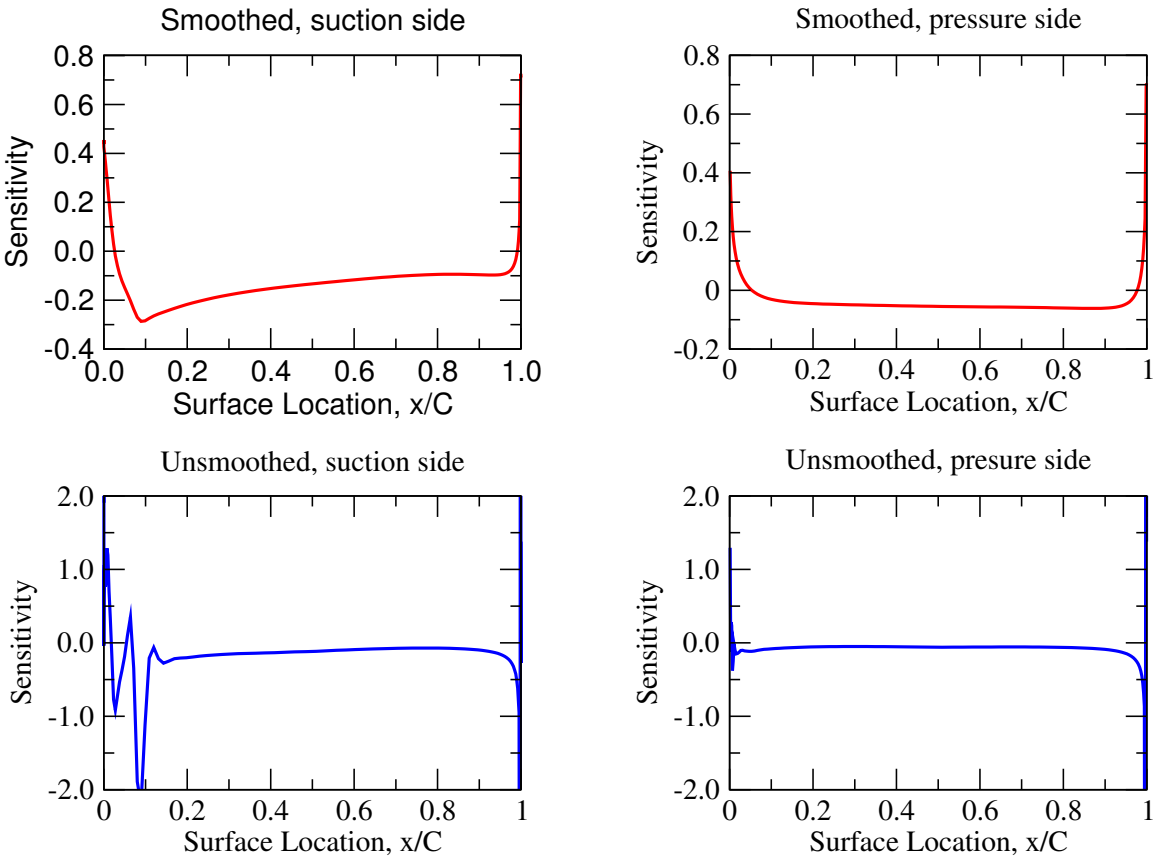
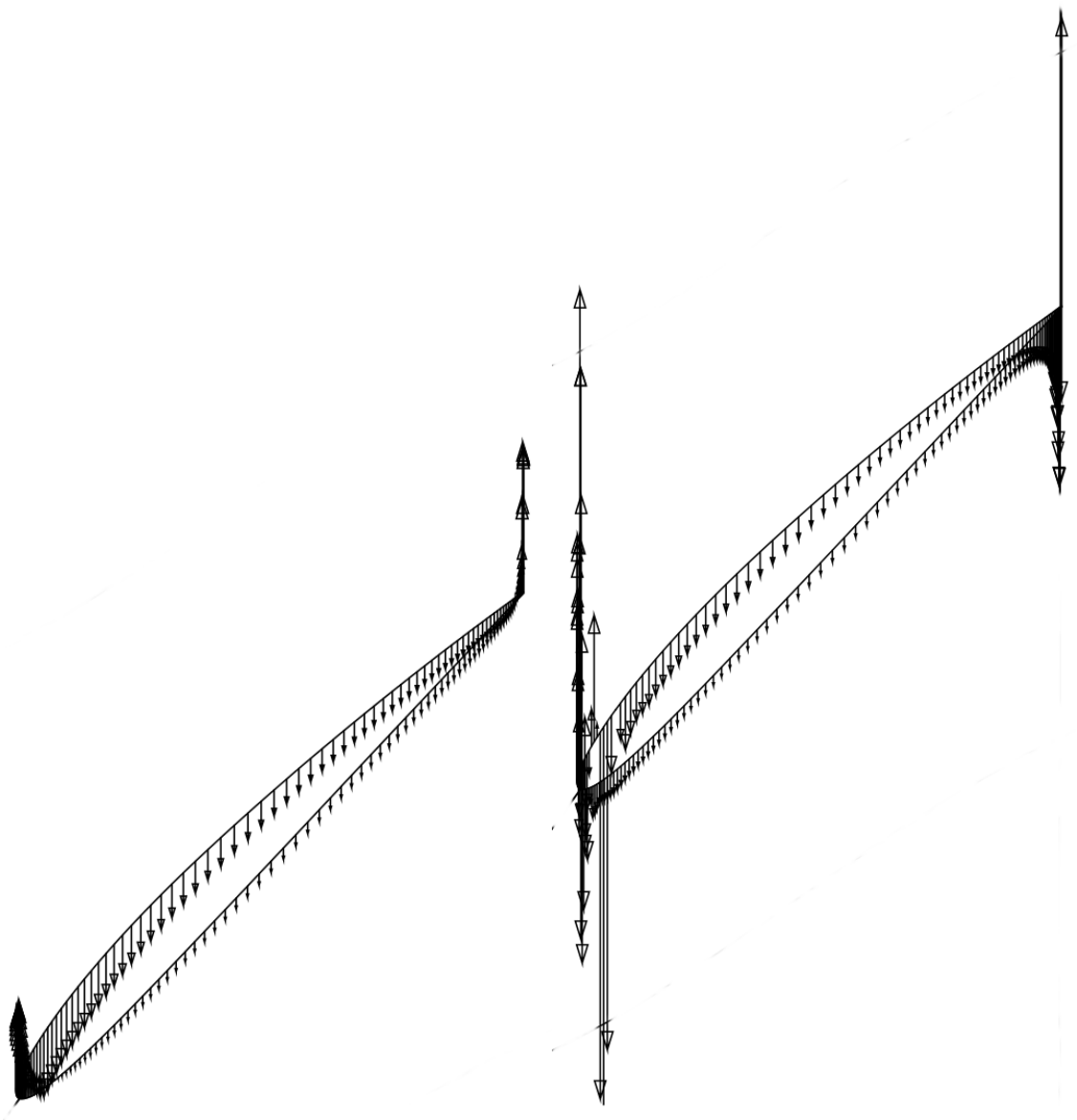


Figure 5.60: Comparison of sensitivities of the new smoothed and unsmoothed method at the first optimization step for the NACA2408 airfoil geometry.



(a) new smoothed method **(b)** unsmoothed method

Figure 5.61: Comparison of sensitivities of the new smoothed and unsmoothed method in vector at the first optimization step for the NACA2408 airfoil geometry

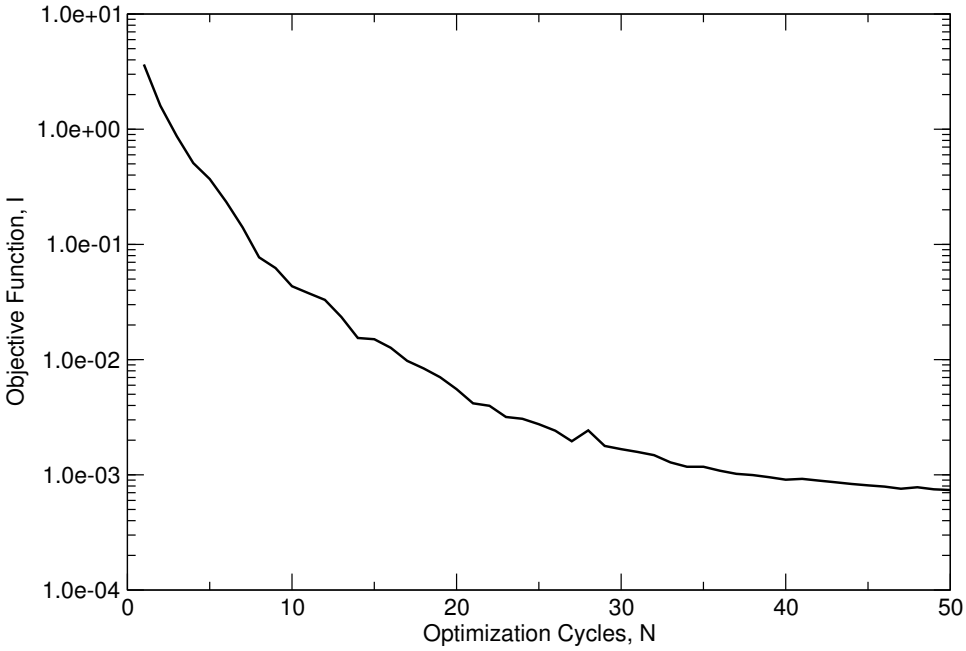
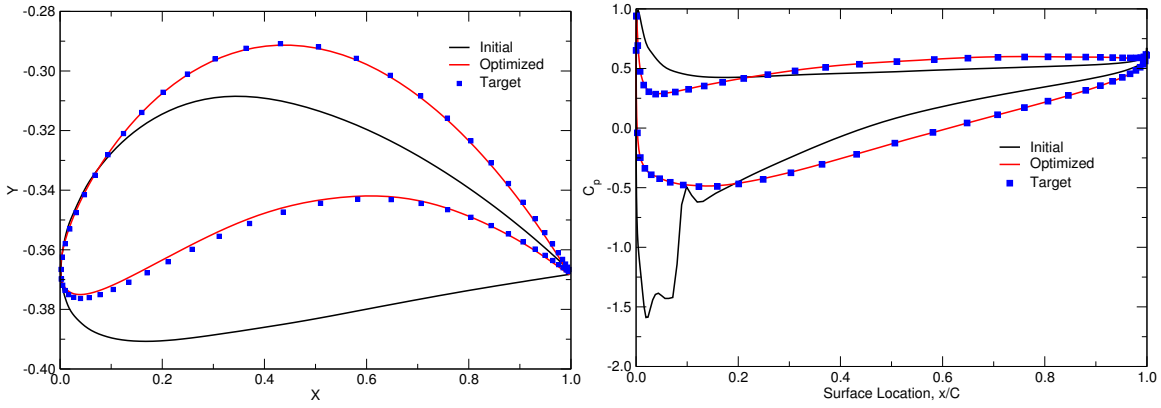
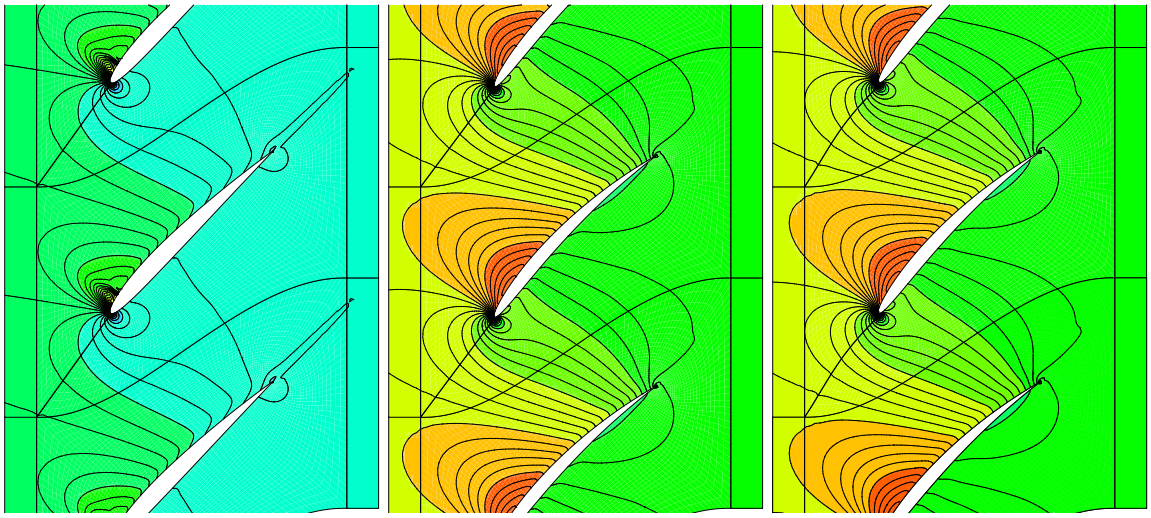


Figure 5.62: Convergence history of for the Tenth Standard Configuration, Case 3.



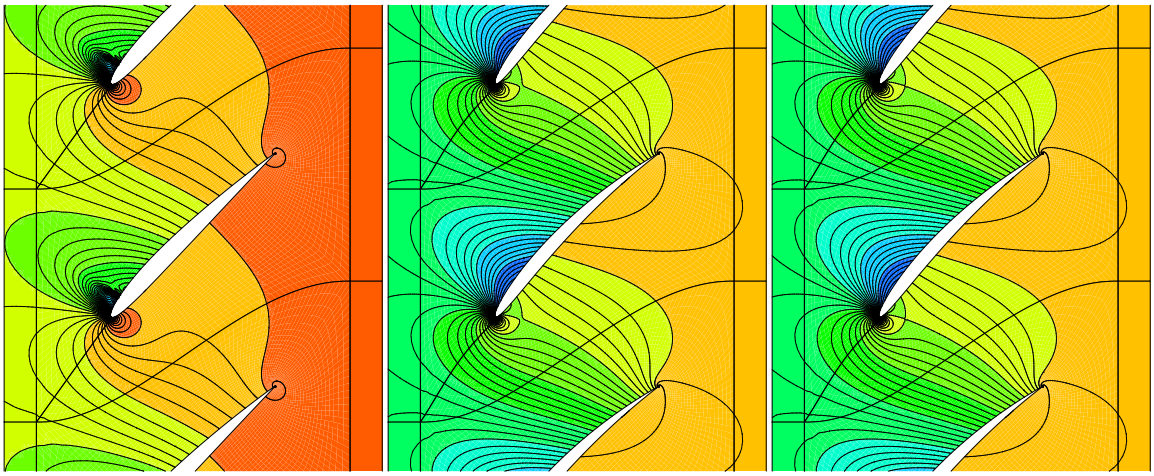
(a) Blade Shape **(b)** Pressure Distirbution

Figure 5.63: Inverse design for the Tenth Standard Configuration, Case 3.



(a) initial **(b)** optimized **(c)** target

Figure 5.64: Mach number contours for inverse design the Tenth Standard Configuration, Case 3.



(a) initial **(b)** optimized **(c)** target

Figure 5.65: Pressure contours for inverse design the Tenth Standard Configuration, Case 3.

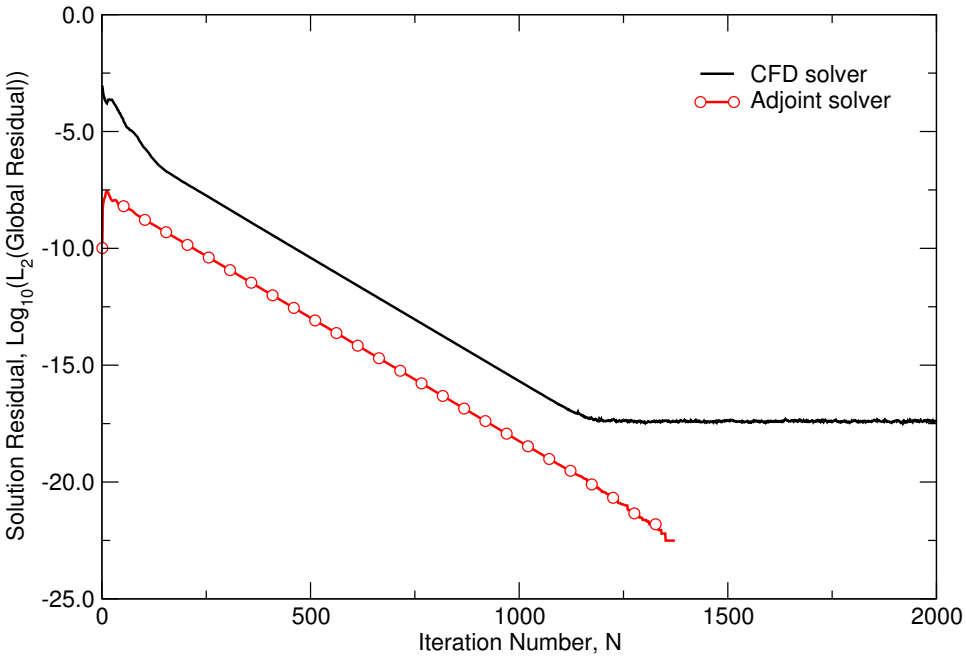


Figure 5.66: Convergence history for the steady adjoint solver and the steady CFD solver.

5.3.3 Optimization for Unsteady Tenth Standard Configuration

Having demonstrated optimization for steady state problems, the discrete adjoint method is applied to the high-dimensional harmonic balance method for unsteady optimization problems. As stated in the introduction, to the author's best knowledge, this is the first study in the literature that investigates unsteady optimization problems using the adjoint method together with the HDHB method.

Three numerical test cases are considered in this section. The first test case is to predict the vibration frequency of the Tenth Standard cascade that drives the system to a neutrally stable state, which results in limit-cycle oscillations (LCO). In Section 5.1.1, the aerodynamic damping for the Tenth Standard Configuration was computed for different IBPAs at the reduced frequency $\omega^* = 0.5$. In general, the aerodynamic damping decreases with a reduction in the reduced frequency. The case with IBPA, $\sigma = 60°$, is considered here. The sensitivity of the aerodynamic damping coefficient with respect to the reduced frequency is determined through an adjoint HDHB solver, and then an optimization solver is used to search for the LCO reduced frequency with the initial reduced frequency, $\omega^* = 0.2$. In this work, the cost function is taken to be the square of the aerodynamic damping coefficient. The convergence history is shown in Figure 5.67. The LCO reduced frequency is found to be $\omega^* = 0.2334$ after six design cycles, with the aerodynamic damping coefficient driven down to -1.4×10^{-7}. Figure 5.68 compares the aerodynamic damping coefficient versus

different IBPAs for $\omega^* = 0.2$ and $\omega^* = 0.5$. As can be seen, for $\omega^* = 0.2334$, the cascade becomes stable for all possible IBPAs whereas for $\omega^* = 0.2$ is unstable for IBPAs values between 40 deg and 90 deg.

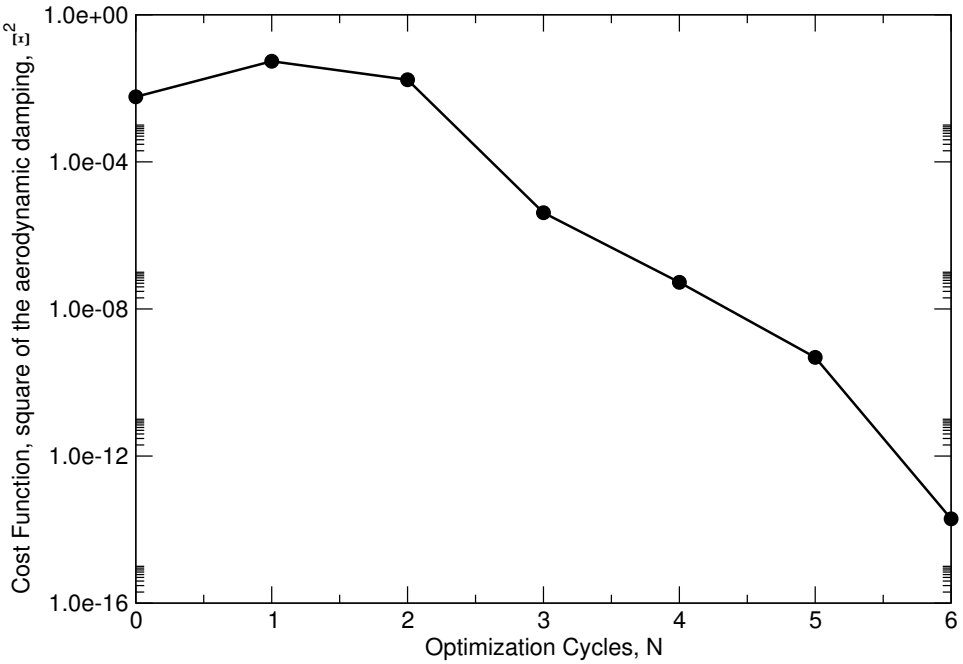


Figure 5.67: Convergence history for LCO reduced frequency of the Ten Standard Configuration.

As the second test case, we perform a shape optimization for this cascade for improved aeroelastics characteristic, that is, improved aerodynamic damping. The pitch amplitude is chosen to be very small so that the unsteady flow is essentially linear, for which one harmonic is sufficient. Numerical computation of interblade phase angle sweep (shown in Figure 5.69) with the reduced frequency $\omega^* = 0.20$ reveals that this configuration has a negative aerodynamic damping between IBPA,

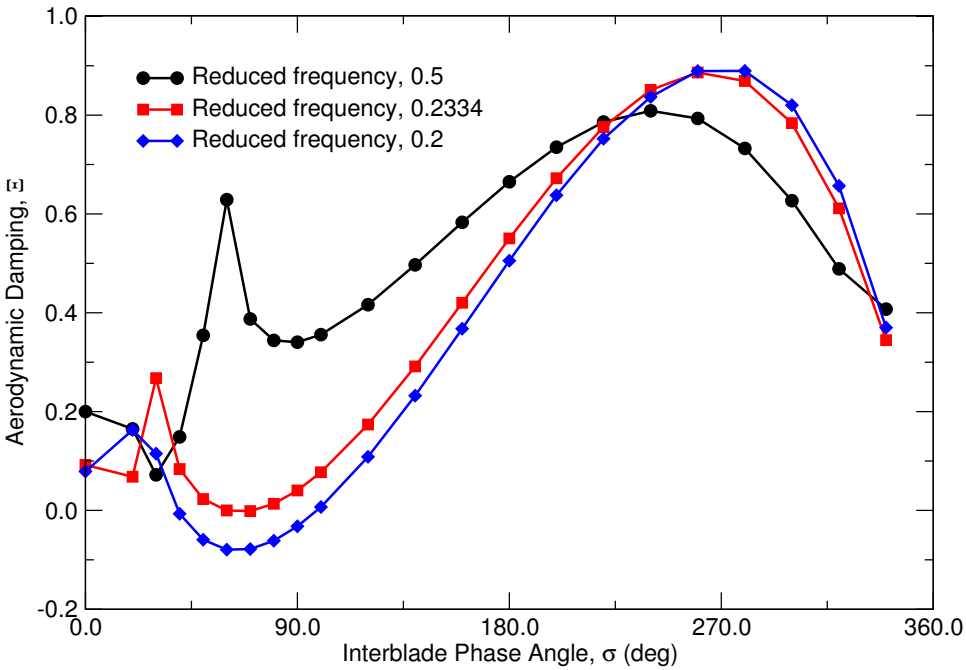


Figure 5.68: Comparison aerodynamic damping versus IBPA for the Ten Standard Configuration, 1 harmonic.

$\sigma = 40° \sim \sigma = 90°$. The motivation is to optimize the cascade shape so that the aerodynamic damping becomes positive at $\sigma = 60°$. Twenty Hicks-Henne functions are equally spanned along the axial chord direction for both the pressure and the suction side as design variables. The sensitivities of the cost function, for instance, the negative of the aerodynamics damping, with respect to the the design variables are computed via an adjoint HDHB solver, and then blade shape is optimized according to the bound-constrained L-BFGS algorithm[122], as one would like to impose some constraints on the cascade geometry. For instance, it is imposed $-0.025 \leqslant a_i \leqslant 0.25$ in this work so as to keep the thickness of the configuration positive. Furthermore, in order to simplify the analysis, the mode shape of the blade is assumed to be constant

during the optimization process. As shown in the Figure 5.70, the aerodynamic damping coefficient increases from an initial value value of -0.0614 to 0.0081. The optimized cascade becomes stable at this flow condition. The comparison between the initial shape and optimized shape (after 10 design cycles) is plotted in Figure 5.71. Another interblade phase angle sweep, shown in Figure 5.69, for the optimized shape shows that the new cascade becomes stable for all IBPAs. In addition, the Mach number contours and static pressure contours for IBPA, $\sigma = 60°$, of the initial and optimized shape are plotted in Figure 5.72 and Figure 5.73, respectively. The computations are performed with a single passage and multi-passage solutions are plotted for clarity. After the shape optimization, the flow field becomes transonic and a shock forms on the suction side. Because of the small vibration amplitude, the difference between each passage cannot be distinguished from the contours. On the other hand, the first harmonic of unsteady Mach number, Figure 5.74, and the first harmonic of the unsteady pressure, Figure 5.75, clearly show the variation between each blade passage. The imaginary unsteady pressure coefficient distribution is plotted in Figure 5.76. Finally, the convergence history of the adjoint solver together with the CFD solver is shown in Figure 5.77. The unsteady adjoint solver has the same convergence rate as the unsteady CFD solver.

Compared to the time-linearised method, the harmonic balance method can model nonlinear unsteady flows accurately. The above shape optimization procedure is repeated for a large pitch angle 0.05 rad ($\approx 2.8°$) with three harmonics retained in the solver. The solutions are given in Figure 5.78. Multiple passage Mach number

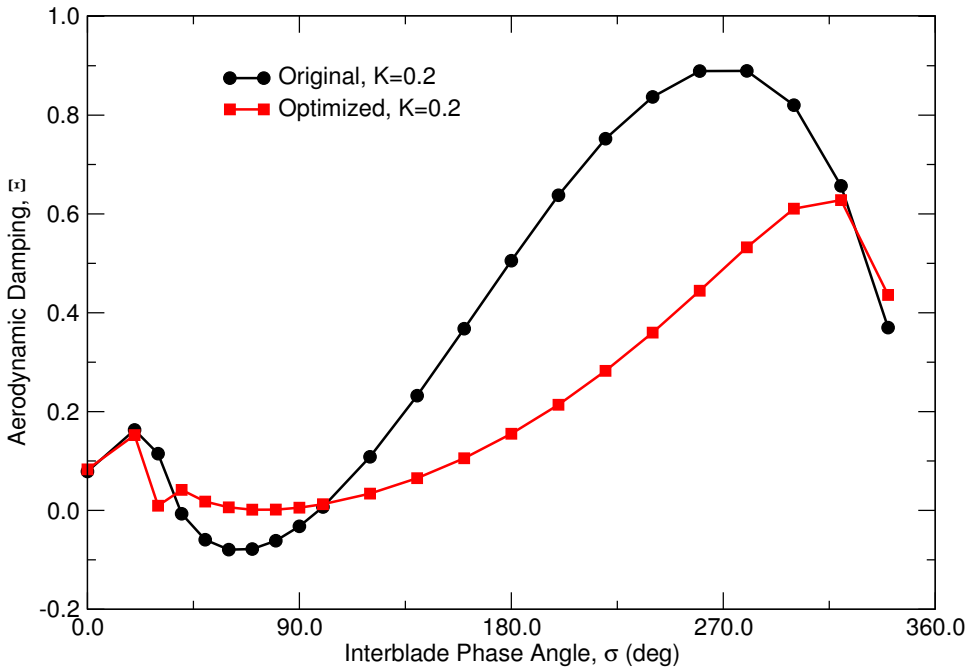


Figure 5.69: Comparison of aerodynamic damping coefficient versus IBPA σ, ω^*=0.2, 1 harmonic.

contours and static pressure contours for IBPA, $\sigma = 60°$, for the initial shape and the optimized one are plotted in Figure 5.79 and Figure 5.80, respectively. One can clearly see the unsteady interaction between each blade passage around leading and trailing edges.

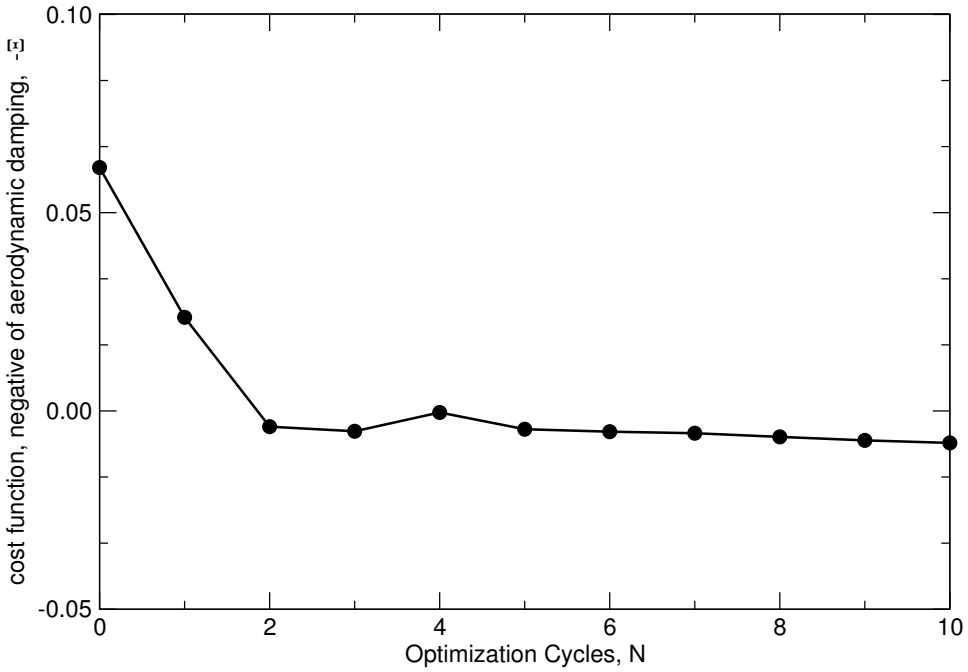


Figure 5.70: Convergence history of unsteady shape optimization for the Tenth Standard Configuration.

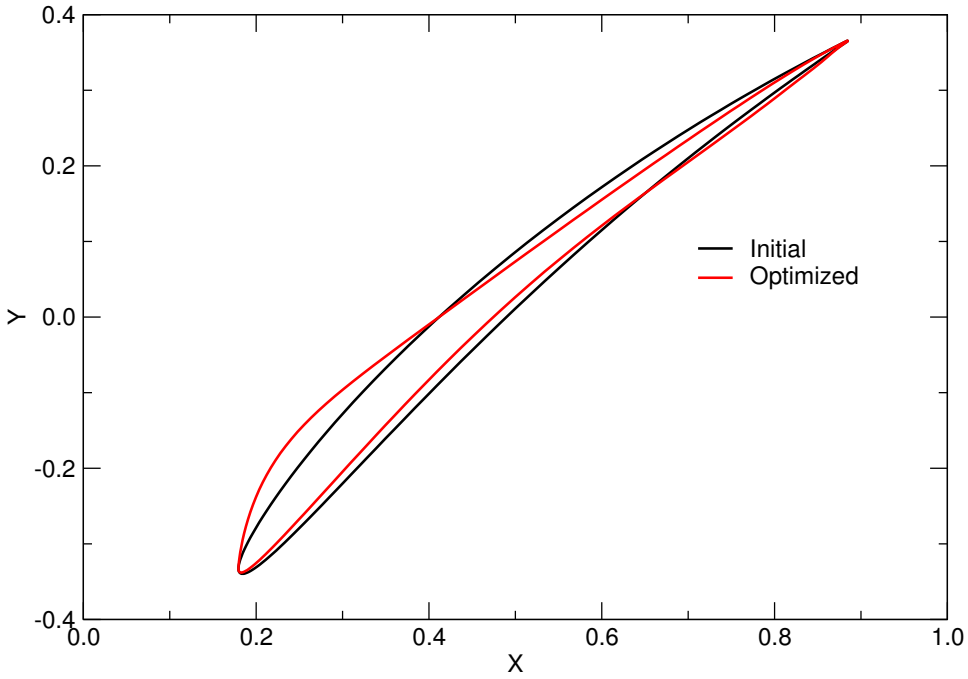
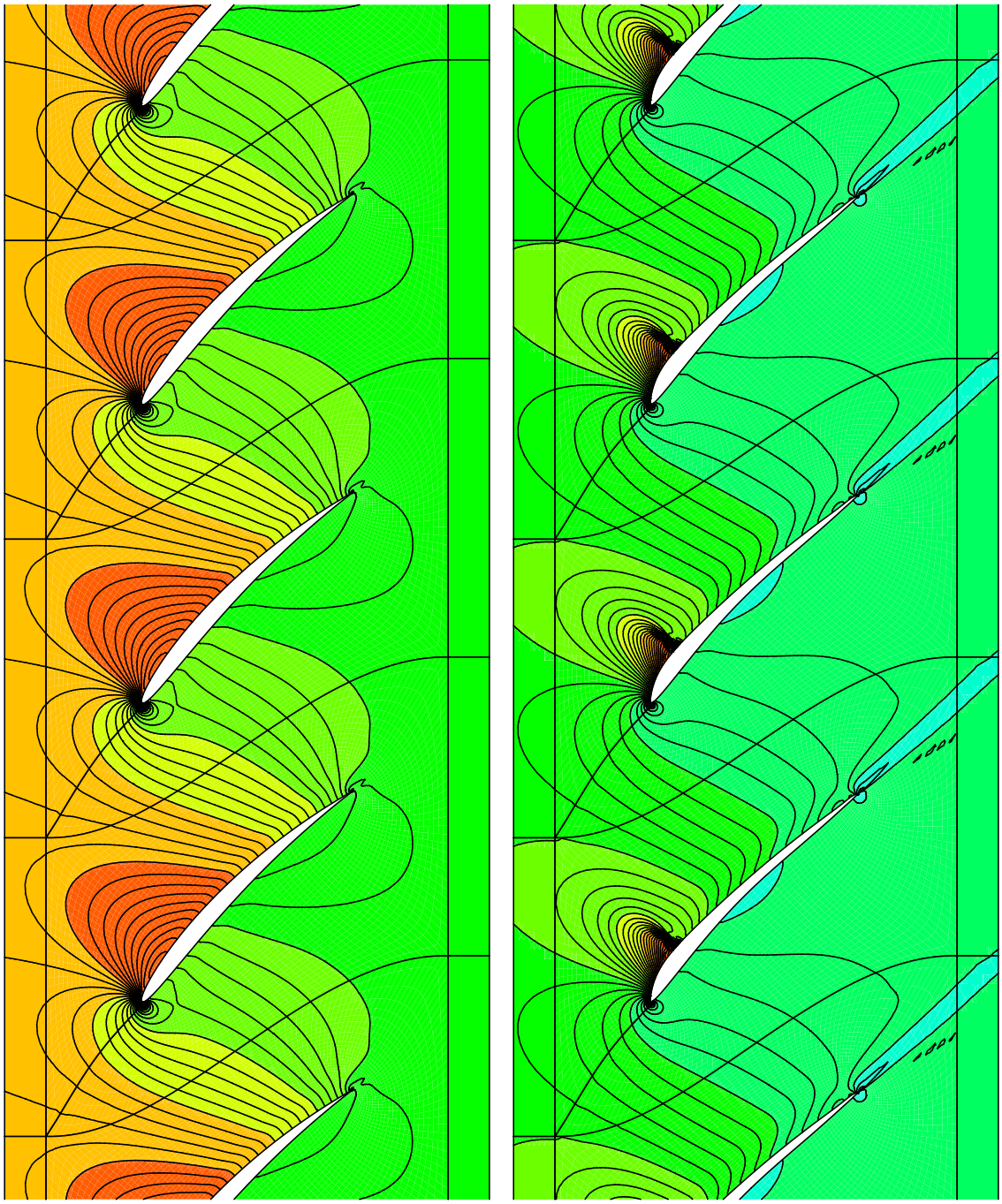
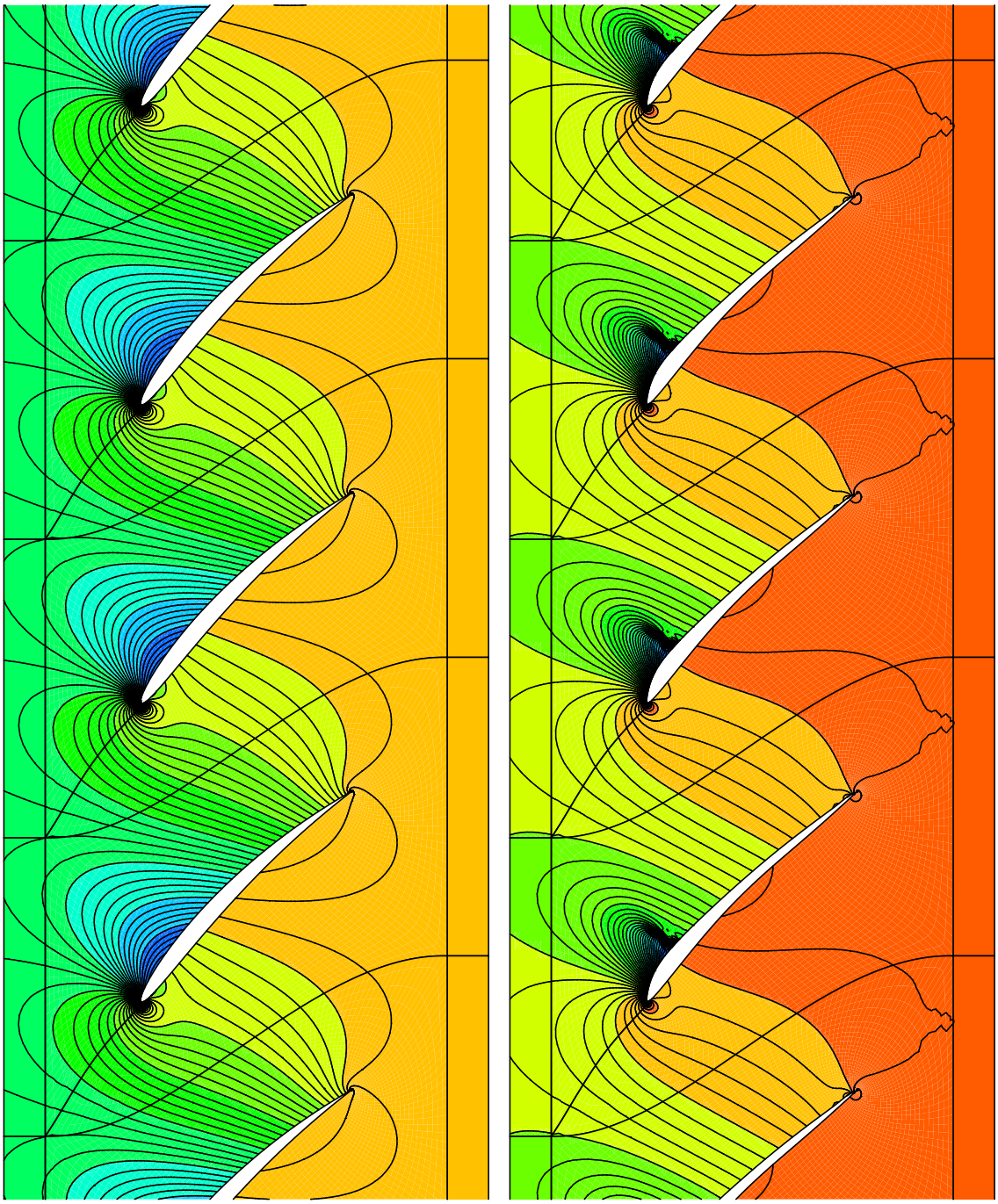


Figure 5.71: Comparison of original Tenth Standard Configuration and optimized configuration geometry.



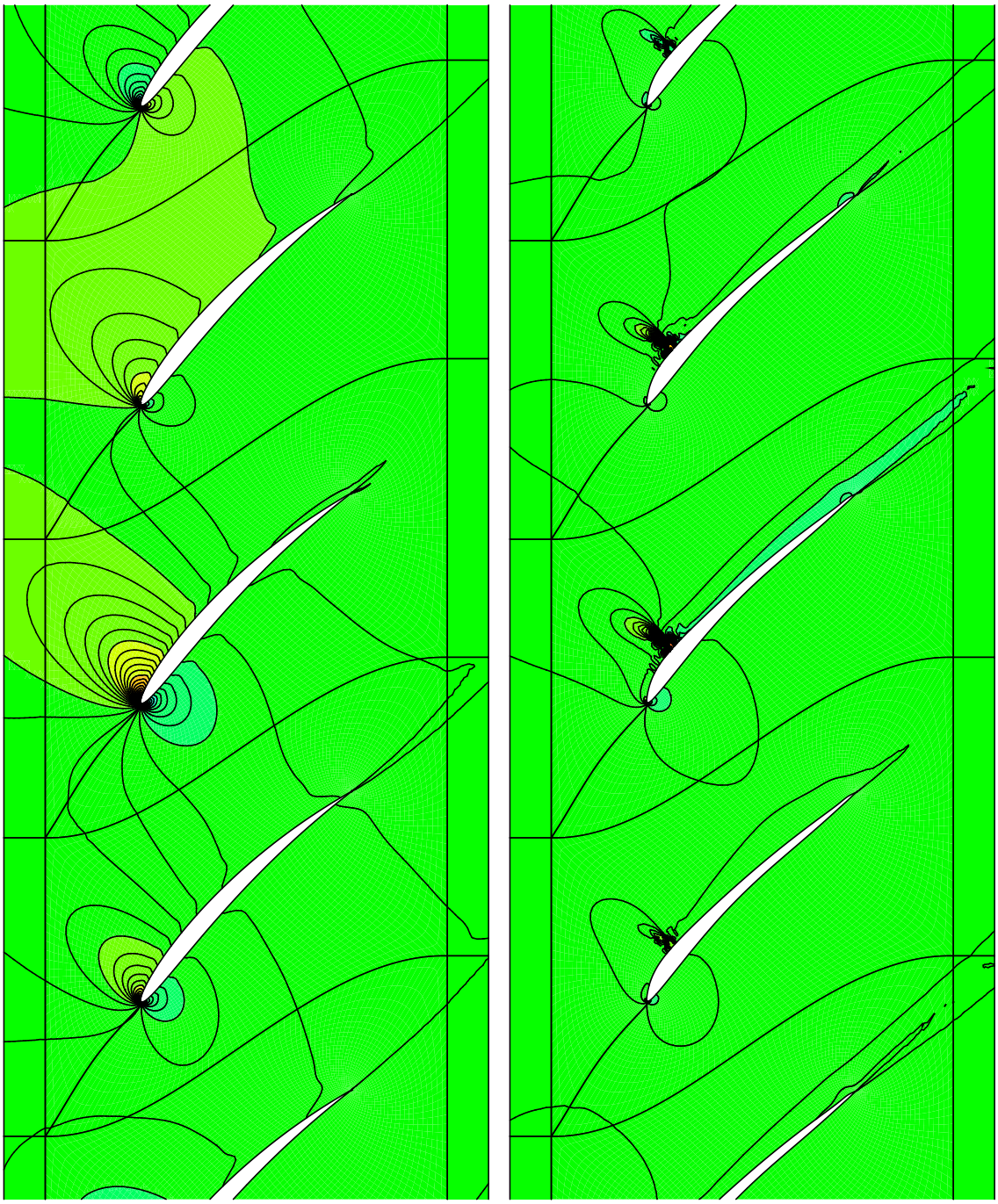
(a) original **(b)** optimized

Figure 5.72: Comparison of the instantaneous Mach number contours, ω^*=0.2, σ=60 deg, 1 harmonic.



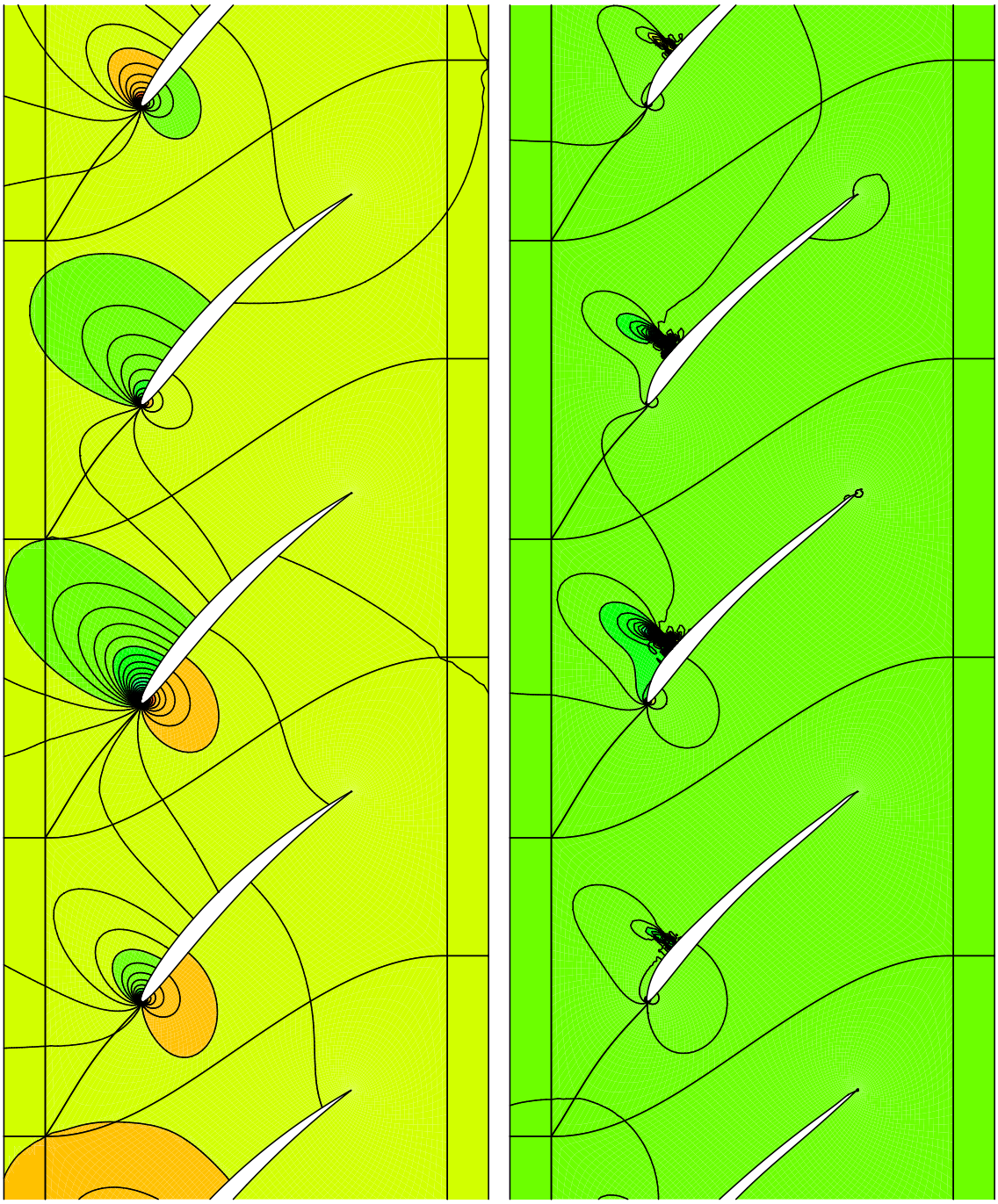
(a) original **(b)** optimized

Figure 5.73: Comparison of the instantaneous static pressure contours, ω^*=0.2, σ=60 deg, 1 harmonic.



(a) original **(b)** optimized

Figure 5.74: Comparison of the unsteady Mach number contours, ω^*=0.2, σ=60 deg, 1 harmonic.



(a) original **(b)** optimized

Figure 5.75: Comparison of the unsteady pressure contours, ω^*=0.2, σ=60 deg, 1 harmonic.

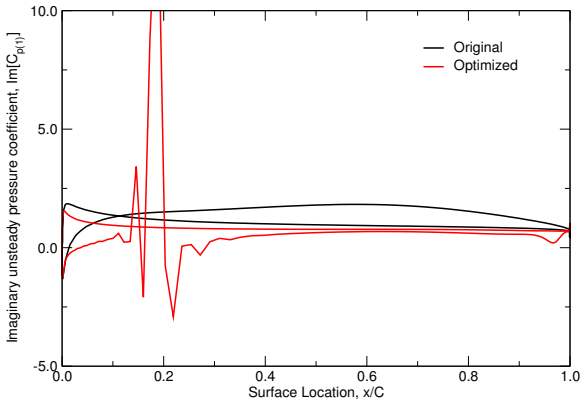


Figure 5.76: Comparison of imaginary unsteady pressure coefficient distribution, ω^*=0.2, σ=60 deg, 1 harmonic.

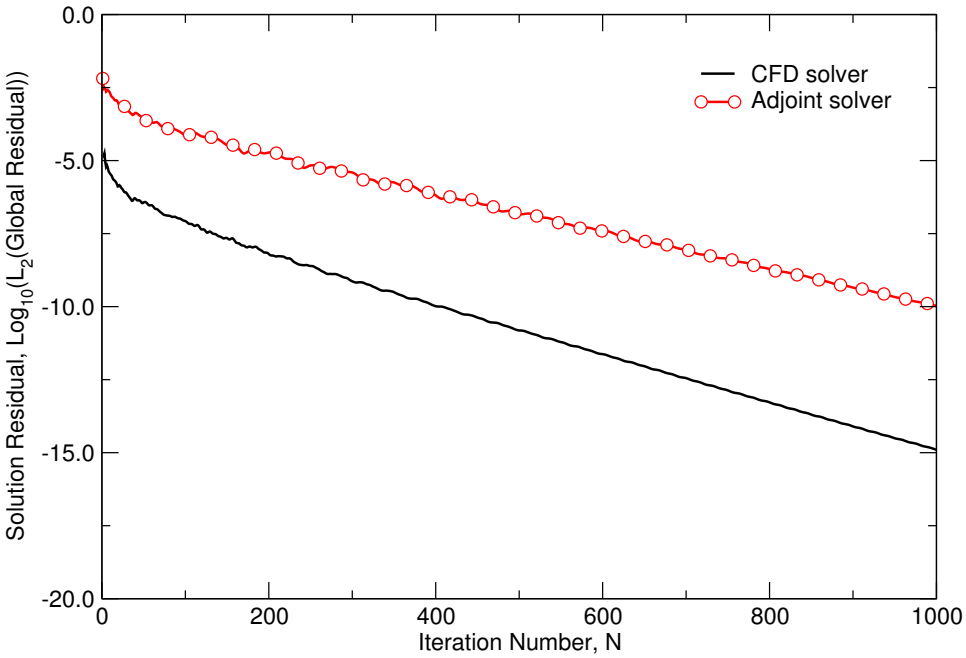
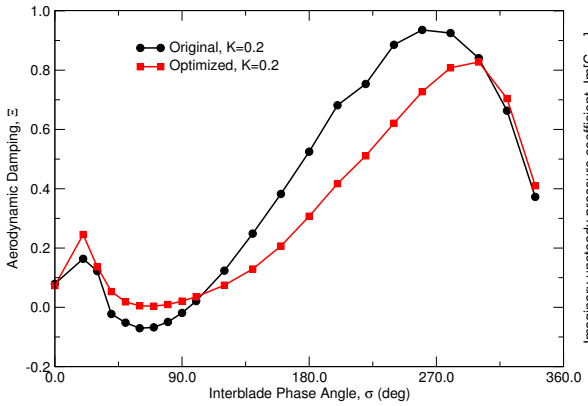
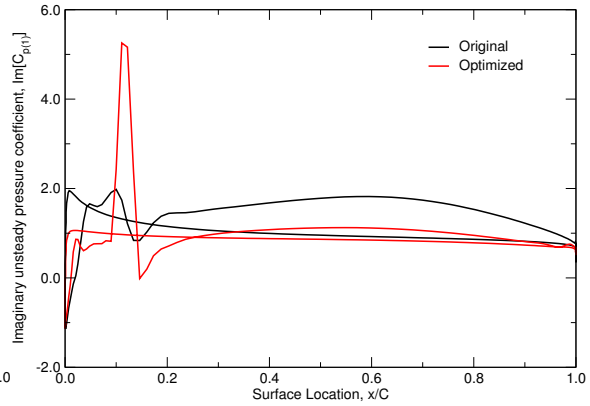


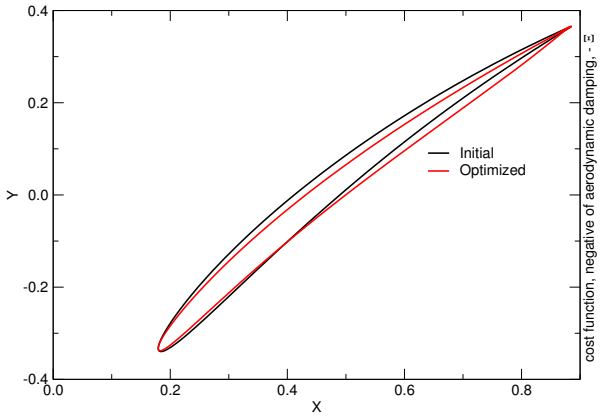
Figure 5.77: Convergence history for the adjoint solver and unsteady CFD solver, 1 harmonic.



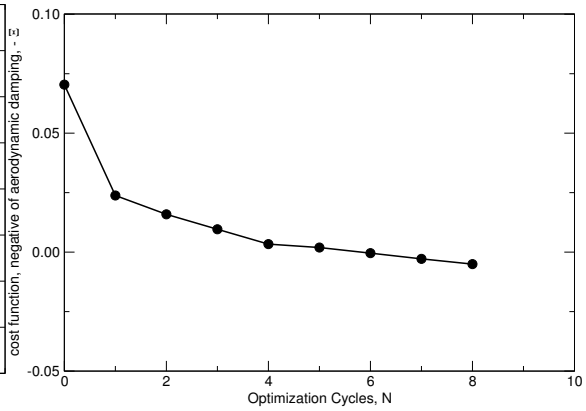
(a) aerodynamic damping versus IBPA



(b) imaginary unsteady pressure coefficient distribution

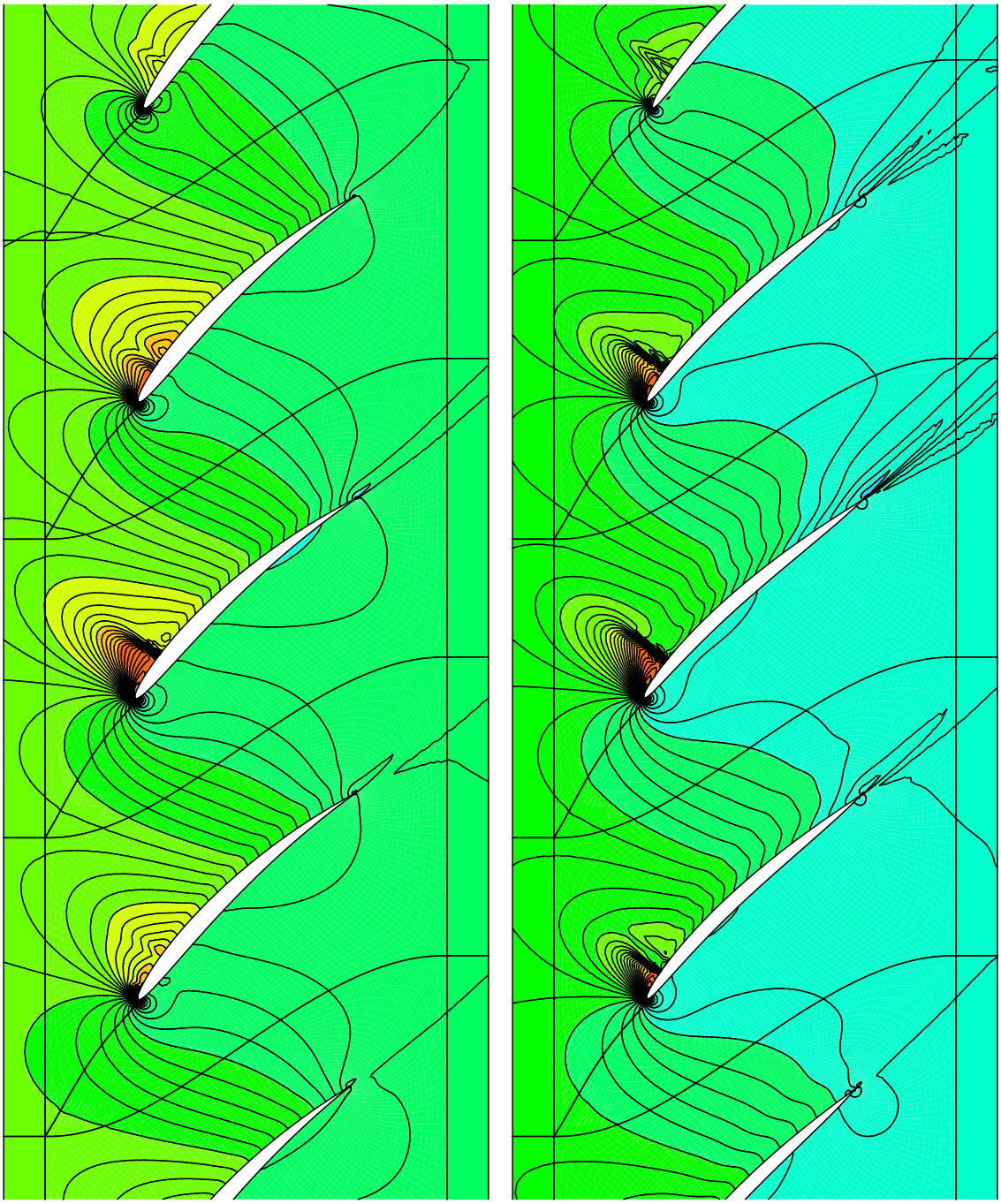


(c) comparison of the shape



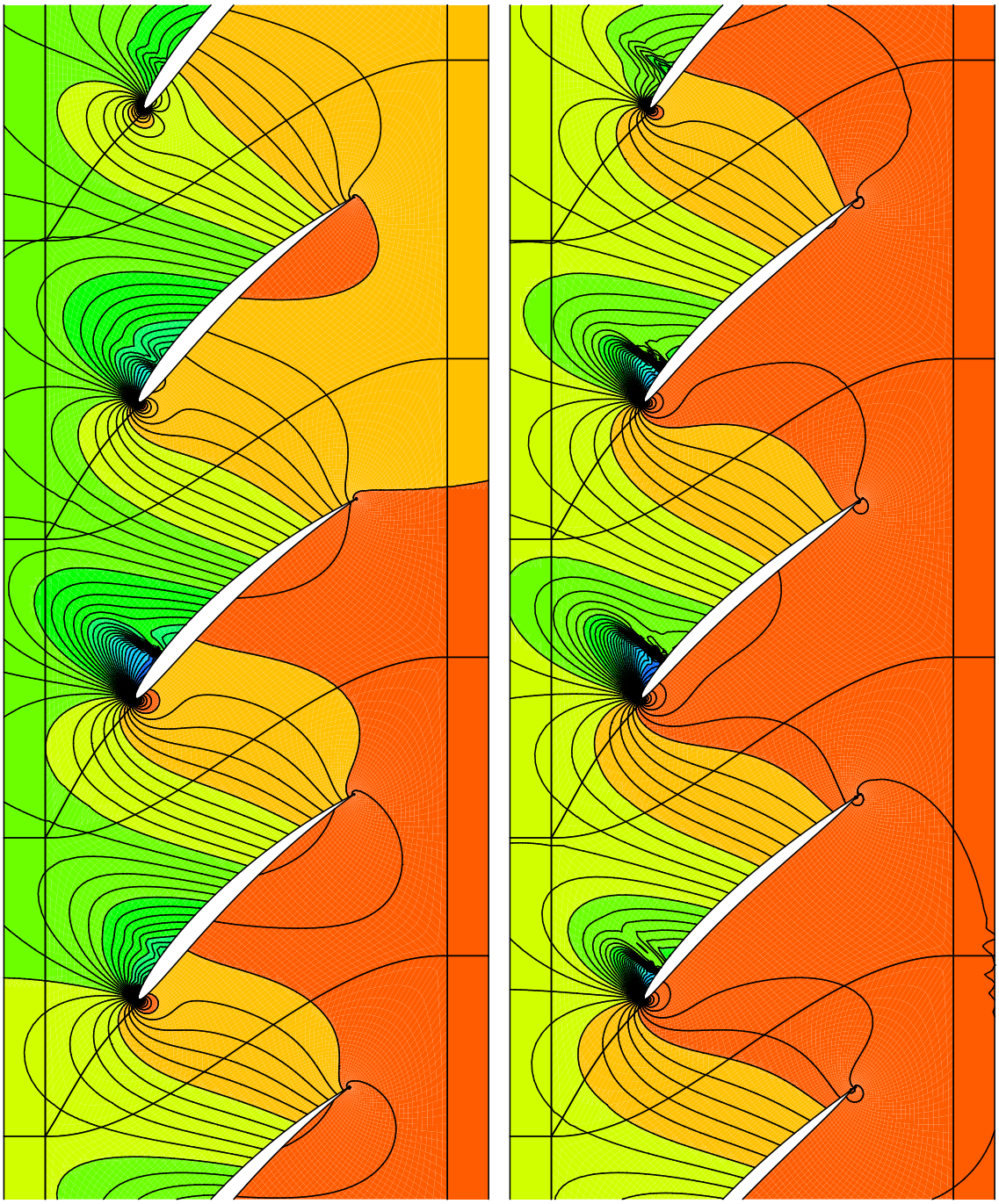
(d) convergence history

Figure 5.78: Solutions for nonlinear unsteady flow of the Tenth Standard Configuration, ω^*=0.2, σ=60 deg, 3 harmonics.



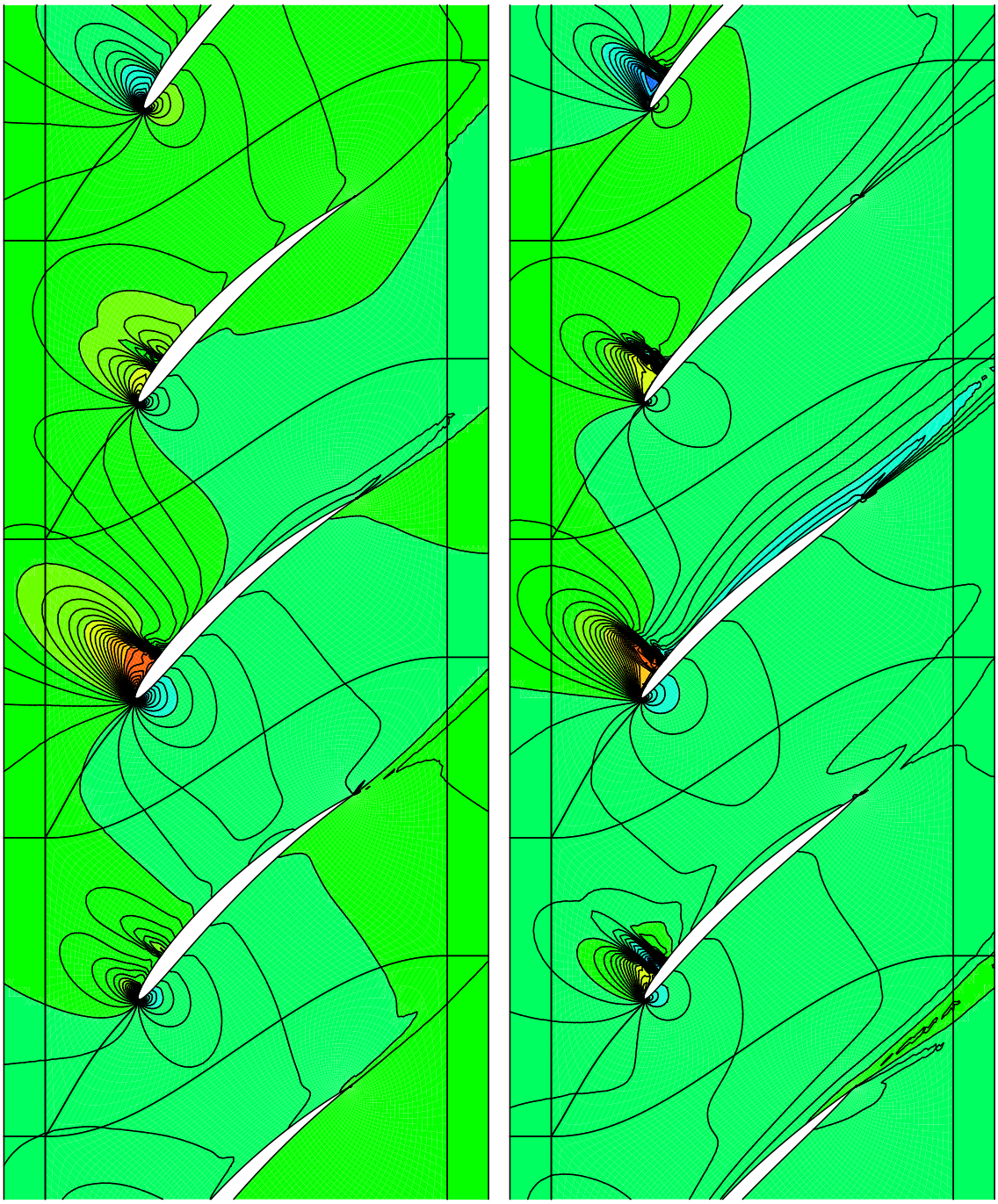
(a) original **(b)** optimized

Figure 5.79: Comparison of the instantaneous Mach number contours, ω^*=0.2, σ=60 deg, 3 harmonics.



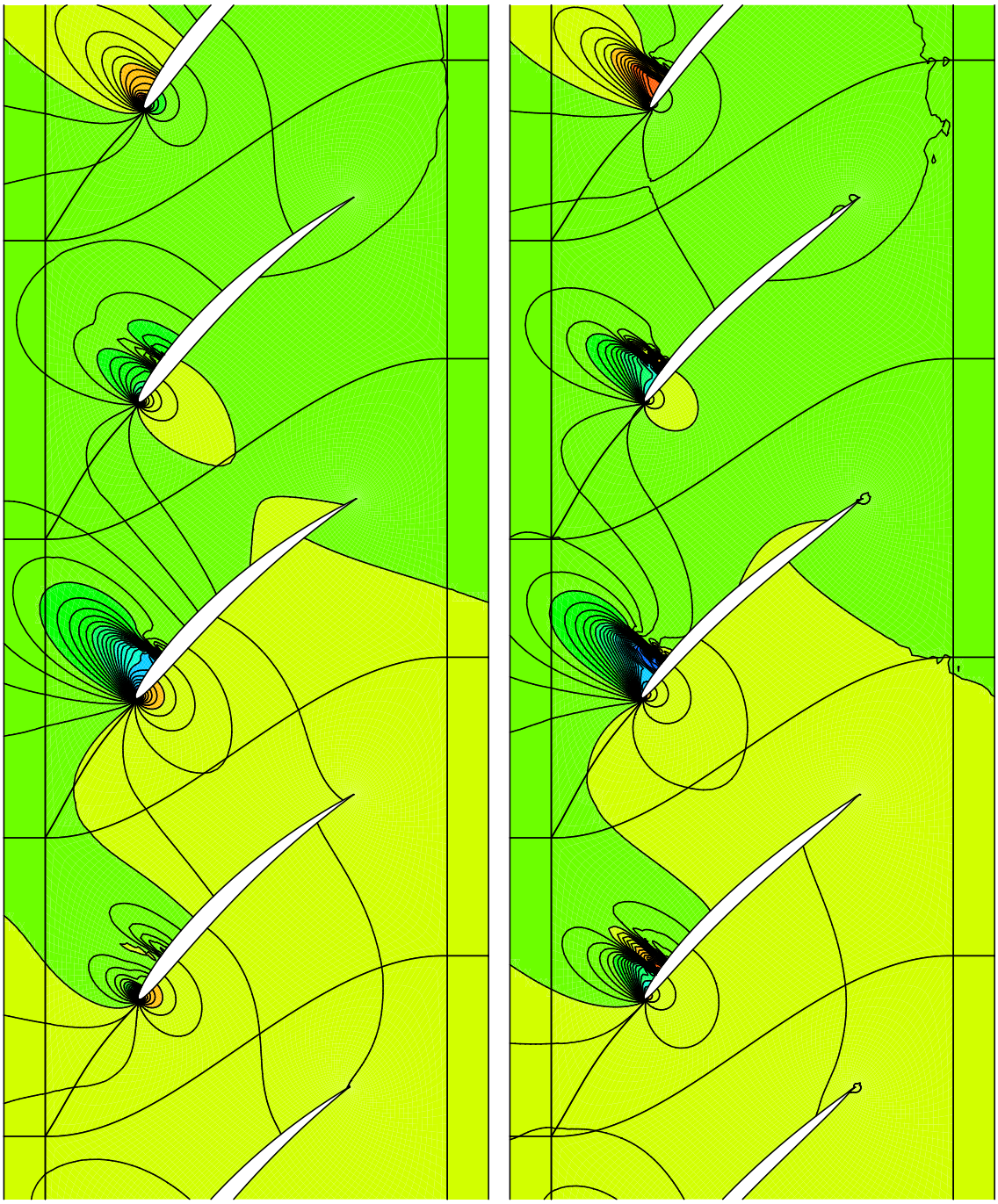
(a) original **(b)** optimized

Figure 5.80: Comparison of the instantaneous static pressure contours, ω^*=0.2, σ=60 deg, 3 harmonics.



(a) original **(b)** optimized

Figure 5.81: Comparison of the unsteady Mach number contours, ω^*=0.2, σ=60 deg, 3 harmonics.



(a) original **(b)** optimized

Figure 5.82: Comparison of the unsteady pressure contours, ω^*=0.2, σ=60 deg, 3 harmonics.

Chapter 6

Conclusions and Future Work

The primary motivation for this dissertation was to provide an efficient and high-fidelity tool for turbomachinery design. A high-dimensional harmonic balance CFD code was developed to solve three-dimensional compressible Reynolds-averaged Navier-Stokes equations together with Spalart-Allmaras turbulence model equation[69] for turbomachincery aeroelastic analysis. In spite of its wide applications, stability issues were occasionally reported in the literature. A temporal spectral viscosity method was developed in the dissertation to stabilize HDHB solvers. The accuracy of the proposed method was demonstrated by a Duffing oscillator case and a vortex shedding over an oscillating cylinder case. Another research focus was to develop an adjoint harmonic balance solver for unsteady turbomachinery shape optimization. A new mesh point smoothing procedure is proposed for two-dimensional inverse design case. In the end, the aerodynamic damping of the Tenth Standard Configuration was improved through unsteady adjoint shape optimization.

In the future, the methodology will be generalized to three-dimensional cases. It is also of great interest to investigate the adjoint Reynolds-averaged Navier-Stokes equations coupled with turbulent equations. Furthermore, it is assumed in this dissertation that the mode shape of a cascade is constant. Therefore, it is suggested to investigate a coupled computational fluid dynamics with computational solid dynamics adjoint method. Other geometric parameterization methods for 3D cascade are worthy of further investigation as well.

Bibliography

[1] Giles, M., "Numerical Methods for Unsteady Turbomachinery Flow," *VKI Numerical Methods for Flows in Turbomachinery*, Vol. 2, 1989.

[2] Jameson, A., "Time Dependent Calculation Using Multigrid, with Applications to Unsteady FLows Past Airfoils and Wings," AIAA Paper 1991-1596, 1991.

[3] Jameson, A. and Baker, T. J., "Solution of the Euler Equations for Complex Configurations," AIAA Paper 1983-1929, 1983.

[4] Jameson, A., "A Vertex Based Multigrid Algorithm for Three Dimensional Compressible Flow Calculations," Numerical methods for compressible flows-finite difference, element and volume techniques, 1986.

[5] He, L. and Denton, J. D., "Three-Dimensional Time-Marching Inviscid and Viscous Solutions for Unsteady Flows Around Vibrating Blades," *Journal of Turbomachinery*, Vol. 116, No. 3, July 1994, pp. 469–476.

[6] McBean, I., Hourigan, K., Thompson, M., and Liu, F., "Prediction of Flutter of Turbine Blades in a Transonic Annular Cascade," *Journal of Fluids Engineering*, Vol. 127, 2005, pp. 1053–1058.

[7] Cinnella, P., Palma, P. D., Pascazio, G., and Napolitano, M., "A Numerical Method for Turbomachinery Aeroelasticity," *Journal of Turbomachinery*, Vol. 126, 2004, pp. 310–316.

[8] Hall, K. C. and Crawley, E. F., "Calculation of Unsteady Flows in Turbomachinery Using the Linearized Euler Equations," *AIAA Journal*, Vol. 27, No. 6, June 1989, pp. 777–787.

[9] Clark, W. S. and Hall, K. C., "A Time-Linearized Navier-Stokes Analysis of Stall Flutter," *Journal of Turbomachinery*, Vol. 122, 2000, pp. 467–476.

[10] Hall, K. C., Thomas, J. P., and Clark, W. S., "Computation of Unsteady Nonlinear Flows in Cascades Using a Harmonic Balance Technique," *AIAA Journal*, Vol. 40, No. 5, May 2002, pp. 879–886.

[11] McMullen, M. and Jameson, A., "Application of a Non-Linear Frequency Domain Solver to the Euler and Navier-Stokes Equations," AIAA Paper 2002-0120, 2002.

[12] McMullen, M. and Jameson, A., "The Computational Efficiency of Non-Linear Frequency Domain Methods," *Journal of Computational Physics*, Vol. 212, 2006, pp. 637–661.

[13] Ekici, K., Hall, K. C., and Dowell, E. H., "Computationally Fast Harmonic Balance Methods for Unsteady Aerodynamic Predictions of Helicopter Rotors," *Journal of Computational Physics*, Vol. 227, No. 12, 2008, pp. 6206–6225.

[14] Huang, H. and Ekici, K., "A Harmonic Balance Method for the Analysis of Unsteady Flows in Cascades," AIAA Paper 2011-5752, 2011.

[15] Gopinath, A. K. and Jameson, A., "Application of the Time Spectral Method to Periodic Unsteady Vortex Shedding," AIAA Paper 2006-0449, 2006.

[16] Spiker, M. A., Thomas, J. P., Hall, K. C., Kielb, R. E., and Dowell, E. H., "Modeling Cylinder Flow Vortex Shedding with Enforced Motion Using a Harmonic Balance Approach," AIAA Paper 2006-1965, 2006.

[17] Ekici, K. and Huang, H., "An Assessment of Frequency-Domain and Time-Domain Techniques for Turbomachinery Aeromechanics," AIAA Paper 2012-3126, 2012.

[18] Gopinath, A. K., Beran, P. S., and Jameson, A., "Comparative Analysis of Computational Methods for Limit-Cycle Oscillations," AIAA Paper 2006-2076, 2006.

[19] Ekici, K. and Hall, K. C., "Harmonic Balance Analysis of Limit Cycle Oscillation in Turbomachinery," *AIAA Journal*, Vol. 49, No. 7, 2011, pp. 1478–1487.

[20] Maple, R. C., King, P. I., Orkwis, P. D., and Wolff, J. M., "Adaptive Harmonic Balance Method for Nonlinear Time-Periodic flows," *Journal of Computational Physics*, Vol. 193, No. 2, 2004, pp. 620–641.

[21] Mosahebi, A. and Nadarajah, S., "An Implicit Adaptive Non-Linear Frequency Domain Method (pNLFD) for Viscous Periodic Steady State Flows on Deformable Grids," AIAA Paper 2011-0775, 2011.

[22] Mosahebi, A. and Nadarajah, S., "Adaptive Non-Linear Frequency Domain Method for Viscous Flows," *Journal of Computers and Fluids*, Vol. 75, 2013, pp. 140–154.

[23] van der Weide, E., Gopinath, A. K., and Jameson, A., "Turbomachinery Applications with the Time Spectral Method," AIAA Paper 2005-4905, 2005.

[24] Custer, C. H., *A Nonlinear Harmonic Balance Solver for an Implicit CFD Code: OVERFLOW 2*, Ph.D. thesis, Duke University, 2009.

[25] Campobasso, M. S. and Baba-Ahmadi, M. H., "Analysis to Unsteady Flows past Horizontal Axis Wind Turbine Airfoils Based on Harmonic Balance Compressible Navier-Stokes Equations with Low-Speed Preconditioning," Proceedings of Gas Turbine Technical Congress and Exposition ASME Turbo Expo 2011 GT2011-45303, 2011.

[26] Melson, N. D., Sanetrik, M. D., and Atkins, H. L., "Time-accurate Navier-Stokes Calculations with Multigrid Acceleration," Proceedings of the sixth copper mountain conference on multigrid methods, 1993.

[27] Sicot, F., Puigt, G., and Montagnac, M., "Block-Jacobi Implicit Algorithms for the Time Spectral Method," *AIAA Journal*, Vol. 46, No. 12, 2008, pp. 3080–3089.

[28] Woodgate, M. and Badcock, K., "Implicit Harmonic Balance Solver for Transonic Flow with Forced Motions," *AIAA Journal*, Vol. 47, No. 4, 2009, pp. 893–901.

[29] Su, X. and Yuan, X., "Implicit Solution of Time Spectral Method for Periodic Unsteady Flows," *International Journal for Numerical Methods in Fluids*, Vol. 63, 2010, pp. 860–876.

[30] Gottlieb, D. and Hesthaven, J. S., "Spectral Methods for Hyperbolic Problems," *Journal of Computational and Applied Mathematics*, Vol. 128, 2001, pp. 83–131.

[31] Gopinath, A., van der Weide, E., Alonso, J. J., Jameson, A., Ekici, K., and Hall, K. C., "Three-Dimensional Unsteady Multi-Stage Turbomachinery Simulations Using the Harmonic Balance Technique," AIAA Paper 2007-0892, 2007.

[32] Liu, L., Thomas, J. P., Dowell, E. H., Attar, P., and Hall, K. C. ., "A Comparison of Classical and High Dimensional Harmonic Balance Approaches for a Duffing Oscillator," *Journal of Computational Physics*, Vol. 215, 2006, pp. 298–320.

[33] LaBryer, A. and Attar, P., "High Dimensional Harmonic Balance Dealiasing Techniques for a Duffing Oscillator," *Journal of Sound and Vibration*, Vol. 324, 2009, pp. 1016–1038.

[34] Maday, Y. and Tadmor, E., "Analysis of the Spectral Vanishing Viscosity Method for Periodic Conservation Laws," *SIAM Journal on Numerical Analysis*, Vol. 26, 1989, pp. 854–870.

[35] Gelb, A. and Tadmor, E., "Enhanced Spectral Viscosity Approximations for Conservation Laws," *Applied Numerical Mathematics*, Vol. 33, 2000, pp. 3–21.

[36] Nocedal, J. and Wright, S. J., *Numerical Optimization, second edition*, Springer-Verlag, 2006.

[37] Davidon, W., "Variable Metric Method for Minimization," *SIAM Journal on Optimization*, Vol. 1, No. 1, 1991, pp. 1–17.

[38] Hicks, R. M., Murman, E. M., and Vanderplaats, G. N., "An Assessment of Airfoil Design by Numerical Optimization," Tech. Rep. NASA TMX-3092, Ames Research Center, Moffett Field, California, 1974.

[39] Pironneau, O., "On Optimium Design in Fluid Mechanics," *Journal of Fluid Mechanics*, Vol. 64, 1974, pp. 97–110.

[40] Jameson, A., "Aerodynamic Design via Control Theory," *Journal of Scientific Computing*, Vol. 3, 1988, pp. 233–260.

[41] Nadarajah, S. and Jameson, A., "A Comparison of the Continuous and Discrete Adjoint Approach to Automatic Aerodynamic Optimization," AIAA paper 2000-0667, 2000.

[42] Kim, S., Alonso, J. J., and Jameson, A., "Design Optimization of High-Lift Configurations Using a Viscous Continuous Adjoint Method," AIAA Paper 2002-0844, 2002.

[43] Leoviriyakit, K. and Jameson, A., "Aerodynamic Shape Optimization of Wings Including Planform Variations," AIAA Paper 2003-0210, 2003.

[44] Jameson, A., "A Perspective on Computational Algorithms for Aerodynamic Analysis and Design," *Progress in Aerospace Sciences*, Vol. 37, 2001, pp. 197–243.

[45] Luo, J., Xiong, J., Liu, F., and McBean, I., "Three-Dimensional Aerodynamic Design Optimization of a Turbine Blade by Using an Adjoint Method," *Journal of Turbomachinery*, Vol. 133, 2011.

[46] Elliott, J. and Peraire, J., "Practical 3D Aerodynamic Design and Optimization Using Unstructured Meshes," *AIAA Journal*, Vol. 35, 1997, pp. 1479–1485.

[47] Nielsen, E. J. and Anderson, W. K., "Aerodynamic Design Optimization on Unstructured Meshes Using the Navier-Stokes Equations," *AIAA Journal*, Vol. 37, 1999, pp. 957–964.

[48] Anderson, W. K. and Bonhaus, D. L., "Aerodynamic Design on Unstructured Grids for Turbulent Flows," *AIAA Journal*, Vol. 37, 1999, pp. 185–191.

[49] Mohammadi, B. and Pironneau, O., "Mesh Adaption and Automatic Differentiation in a CAD-Free Framework for Optimal Shape Design," *International Journal for Numerical Methods in Fluids*, Vol. 30, 1999, pp. 127–136.

[50] Giles, M. B. and Pierce, N. A., "An Introducion to the Adjoint Approach to Design," *Flow, Turbulence, and Combustion*, Vol. 65, 2000, pp. 393–415.

[51] Giles, M. B., Duta, M. C., Muller, J.-D., and Pierce, N. A., "Algorithm Developements for Discrete Adjoint Methods," *AIAA Journal*, Vol. 41, 2003, pp. 198–205.

[52] Giles, M. B., Ghate, D., and Duta, M. C., "Using Automatic Differentiation for Adjoint CFD Code Development," Sarod workshop, 2005.

[53] Duta, M. C., Shahpar, S., and Giles, M. B., "Turbomachinery Design Optimization Using Automatic Differentiated Adjoint Code," Proceedings of GT2007 ASME Turbo Expo 2007: Power for Land, Sea and Air GT2007-28329, 2007.

[54] Mader, C. A., Martins, J. R. R. A., Alonso, J. J., and van der Weide, E., "ADjoint: An Approach for the Rapid Development of Discrete Adjoint Solvers," *AIAA Journal*, Vol. 46, April 2008, pp. 863–873.

[55] Saad, Y. and Schultz, M. H., "GMRES: a Generalized Minimal Residual Algorithm for Solving Nonsymmetric Linear Systems," *SIAM J. Sci. Stat. Comput.*, Vol. 7, No. 3, July 1986, pp. 856–869.

[56] Balay, S., Brown, J., , Buschelman, K., Eijkhout, V., Gropp, W. D., Kaushik, D., Knepley, M. G., McInnes, L. C., Smith, B. F., and Zhang, H., "PETSc Users Manual," Tech. Rep. ANL-95/11 - Revision 3.3, Argonne National Laboratory, 2012.

[57] Mader, C. A. and Martins, J. R. R. A., "Optimal Flying Wings: a Numerical Optimization Study," AIAA paper 2012-1758, 2012.

[58] Lyu, Z. and Martins, J. R. R. A., "Aerodynamic Shape Optimization of a Blended-Wing-Body Aircraft," AIAA paper 2013-0283, Grapevine, TX, 2013.

[59] Wang, L., Mavriplis, D. J., and Anderson, K. W., "Unsteady Discrete Adjoint Formulation for High-Order Discontinuous Galerkin Discretizations in Time-Dependent Flow Problems," AIAA paper 2010-0367, 2010.

[60] Mavriplis, D. J., "Solution of the Unsteady Discrete Adjoint for Three-Dimensional Problems on Dynamically Deforming Unstructured Meshes," AIAA paper 2008-0727, 2008.

[61] Wang, Q., *Uncertainty Quantification for Unsteady Fluid Flow Using Adjoint-Based Approaches*, Ph.D. thesis, Stanford University, 2009.

[62] Beran, P. S., Stanford, B., and Kurdi, M., "Sensitivity Analysis for Optimization of Dynamic Systems with Reduced Order Modeling," AIAA paper 2010-1503, 2010.

[63] Nadarajah, S., McMullen, M., and Jameson, A., "Optimal Control of Unsteady Flows Using Time Accurate and Non-Linear Frequency Domain Methods," AIAA paper 2003-3875, 2003.

[64] Thomas, J. P., Hall, K. C., and Dowell, E. H., "Discrete Adjoint Approach for Modeling Unsteady Aerodynamic Design Sensitivities," *AIAA Journal*, Vol. 43, 2005, pp. 1931–1936.

[65] Choi, S., Potsdam, M., Lee, K., Iaccarino, G., and Alonso, J., "Helicopter Rotor Design Using a Time-Spectral and Adjoint-Based Method," AIAA paper 2008-5810, 2008.

[66] Mader, C. A. and Martins, J. R. R. A., "Derivatives for Time-Spectral Computational Fluid Dynamics Using an Automatic Differentiation Adjoint," *AIAA Journal*, Vol. 50, 2012, pp. 2809–2819.

[67] Hascoët, L. and Pascual, V., "TAPENADE 2.1 User's Guide," Technical Report 0300, INRIA, 2004.

[68] Clark, W. S., *Investigation of Unsteady Viscous Flows In Turbomachinery Using A Linearized Navier-Stokes Analysis*, Ph.D. thesis, Duke University, 1998.

[69] Spalart, P. R. and Allmaras, S. R., "One-Equation Turbulence Model for Aerodynamic Flows," AIAA Paper 92-0439, 1992.

[70] Martinelli, L., Jameson, A., and Grasso, F., "A Multigrid Method for the Navier-Stokes Equations," AIAA Paper 1986-0208, 1986.

[71] Jameson, A., Schmidt, W., and Turkel, E., "Numerical Solution of the Euler Equations by Finite Volume Methods Using Runge-Kutta Time-Stepping Schemes," AIAA Paper 1981-1259, 1981.

[72] Martinelli, L. and Jameson, A., "Validation of a Multigrid Method for the Reynolds Averaged Equations," AIAA Paper 1988-0414, 1988.

[73] Radespiel, R., Rossow, C., and Swanson, R. C., "Efficient Cell-Vertex Multigrid Scheme for the Three-Dimensional Navier-Stokes Equations," *AIAA Journal*, Vol. 2, No. 8, 1990, pp. 1464–1472.

[74] Swanson, R. C. and Turkel, E., "Multistage Schemes with Multigrid for Euler and Navier-Stokes Equations," NASA Techical Paper 1997-3631, 1997.

[75] Saxer, A. P. and Giles, M. B., "Quasi-Three-Dimensional Nonreflecting Boundary Conditions for Euler Equations Calculations," *Journal of Propulsion and Power*, Vol. 9, No. 2, March 1993, pp. 263–271.

[76] Hall, K.C.and Lorence, C. and W.S., C., "Nonreflecting Boundary Conditions for Linearized Unsteady Aerodynamic Calculations," AIAA Paper 1993-088, 1993.

[77] Kielb, R., Hall, K., Spiker, M., Thomas, J., Pratt Jr, E., and Jeffries, R., "Non-Synchronous Vibration of Turbomachinery Airfoils," Tech. rep., DTIC Document, 2006.

[78] Gentilli, N., *Efficient Solution of Unsteady Nonlinear Flows Using a Multiple Zone Harmonic Balance Technique*, Master's thesis, Duke University, 2010.

[79] Hall, K. C., Ekici, K., Thomas, J. P., and Dowell, E. H., "Harmonic Balance Methods Applied to Computational Fluid Dynamics Problems," *International Journal of Computational Fluid Dynamics*, Vol. 27, 2013, pp. 52–67.

[80] Tadmor, E., "Convergence of Spectral Methods for Nonlinear Conservation Laws," *SIAM Journal on Numerical Analysis*, Vol. 26, No. 1, 1989, pp. 30–44.

[81] Tadmor, E., "Super Viscosity and Spectral Approximations of Nonlinear Conservation Laws," Proceedings of the 1993 conference on numerical methods for fluid dynamics, clarendon press, 1993.

[82] Hou, T. Y. and Li, R., "Computing Nearly Singular Solutions Using Pseudo-Spectral Methods," *Journal of Computational Physics*, Vol. 226, 2007, pp. 379–397.

[83] Xu, C. and Pasquetti, R., "Stabilized Spectral Element Computations of High Reynolds Number Incompressible Flows," *Journal of Computational Physics*, Vol. 196, 2004, pp. 680–704.

[84] Fornberg, B., "On a Fourier Method for the Integration of Hyperbolic Equations," *SIAM Journal on Numerical Analysis*, Vol. 12, No. 4, 1975, pp. 509–528.

[85] Robert, A. J., "The Integration of a Low Order Spectral Form of the Primitive Meteorological Equations (Spherical Harmonics Integration of Low Order Spectral Form of Primitive Meteorological Equations)," *Meteorological Society of Japan, Journal*, Vol. 44, 1966, pp. 237–245.

[86] Asselin, R., "Frequency Filter for Time Integrations," *Monthly Weather Review*, Vol. 100, No. 6, 1972, pp. 487–490.

[87] Giering, R., *Tangent Linear and Adjoint Model Compiler, Users Manual*, Center for Global Change Sciences, Department of Earth, Atmospheric, and Planetary Science, MIT, Cambridge, MA, December 1997, Unpublished.

[88] Hicks, R. and Henne, P., "Wing Design by Numerical Optimization," *Journal of Aircraft*, Vol. 15, No. 7, 1978.

[89] Liu, D. and Nocedal, J., "On the Limited Memory BFGS Method for Large Scale Optimization," *Mathematical Programming*, Vol. 45, No. 1, 1989, pp. 503–528.

[90] Wolfe, P., "Convergence Conditions for Ascent Methods," *Siam Review*, Vol. 11, No. 2, 1969, pp. 226–235.

[91] Wolfe, P., "Convergence Conditions for Ascent Methods. II: Some Corrections," *SIAM review*, Vol. 13, No. 2, 1971, pp. 185–188.

[92] Jameson, A. and Reuther, J., "Control Theory Based Airfoil Design Using Euler Equation," Proceedings of aiaa/usaf/nasa/issmo symposium on multidisciplinary analysis and optimization, 1994.

[93] Golub, G. H. and Van Loan, C. F., *Matrix Computations, fourth edition*, JHU Press, 2012.

[94] Fransson, T. H. and verdon, J. M., "Update Report on Standard Configuration for Unsteady Flow Through Vibrating Axial-Flow Turbomachine-Cascades," Report, royal institute of technology, stockholm, sweden, 1991.

[95] Petrie-Repar, P., "Development of an Efficient and Robust Linearised Navier-Stokes Flow Solver," *Unsteady Aerodynamics, Aeroacoustics and Aeroelasticity of Turbomachines,Vol VI,*, 2006, pp. 437–448.

[96] Fransson, T. H., Jocker, M., and A. Boelcs, P., "Viscous and Inviscid Linear/Nonlinear Calculation Versus Quasi Three-Dimensional Experimental Data for a New Aeroelastic Turbine Standard Configuration," *Journal of Turbomachinery*, Vol. 121, 1999, pp. 717–725.

[97] Sbardella, L. and Imregun, M., "Linearized Unsteady Viscous Turbomachinery Flow Using Hybrid Grids," *Journal of Turbomachinery*, Vol. 123, 2001, pp. 568–582.

[98] Campobasso, M. S. and Giles, M. B., "Effects of Flow Instablities on the Linear Analysis of Turbomachinery Aeroelasticity," *Journal of Propulsion and Power*, Vol. 19, 2003, pp. 250–259.

[99] Williamson, C., "Defining a Universal and Continuous Strouhal Reynolds Number Relationship for the Laminar Vortex Shedding of a Circular Cylinder," *Physics of Fluids*, Vol. 31, 1988, pp. 2742–2744.

[100] Strazisar, A. J., Wood, J., Hathaway, M. D., and Suder, K. L., "Laser Anemometer Measurements in a Transonic Axial-Flow Fan Rotor," NASA Technical Report 2879, 1989.

[101] Doi, H., *Fluid/Structure Coupled Aeroelastic Computations for Transonic Flows in Turbomachinery*, Ph.D. thesis, Stanford University, 2002.

[102] Zheng, Y. and Yang, H., "Coupled Fluid-Structure Flutter Analysis of a Transonic Fan," *Chinese Journal of Aeronautics*, Vol. 24, No. 3, 2011, pp. 258–264.

[103] Sadeghi, M. and Liu, F., "Coupled Fluid-Structure Simulation for Turbomachinery Blade Rows," AIAA Paper 2005-0018, 2005.

[104] Ekici, K., Voytovych, D., and Hall, K., "Time-Linearized Navier-Stokes Analysis of Flutter in Multistage Turbomachines," AIAA Paper 2005-0836, 2005.

[105] Petrie-Repar, P. J., McGhee, A., and Jacobs, P. A., "Three-Dimensional Viscous Flutter Analysis of Standard Configuration 10," ASME Turbo Expo 2007: Power for Land, Sea and Air GT2007-27800, 2007.

[106] Yang, H. and He, L., "Experimental Investigation of Linear Compressor Cascade with 3-D Blade Oscillation," *AIAA Journal of Propulsion and Power*, Vol. 20, No. 1, 2004, pp. 180–188.

[107] Ott, P., "Information for 3D Computations of the STCF4 Test Cases," Ecole Polytechnique Federale De Lausanine Report LTT-02-04, 2002.

[108] Cinnella, P., Cappiello, E., and Palma, P. D., "A Numerical Method for 3D Turbomachinery Aeroelasticity," ASME Turbo Expo GT2004-54060, 2004.

[109] Fransson, T. H. and Verdon, J. M., "Standard Configurations Fourth Standard Configuration (Cambered Turbine Cascade in Transonic Flow)," http://www.energy.kth.se/proj/projects/MarkusJoecker/STCF/STCF1to10/stcf4.asp.

[110] Duffing, G., *Erzwungene Schwingungen bei veränderlicher Eigenfrequenz und ihre technische Bedeutung*, No. 41-42, R, Vieweg & Sohn, 1918.

[111] Sieverding, C. H. and Heinemann, H., "The Influence of Boundary Layer State on Vortex Shedding from Flate Plates and Turbine Cascades," *Journal of Turbomachinery*, Vol. 112, 1990, pp. 181–187.

[112] Bassi, F., Crivellini, A., Rebay, S., and Savini, M., "Discontinuous Galerkin Solution of the Reynolds-Averaged Navier-Stokes and $k-\omega$ Turbulence Model Equations," *Computers and Fluids*, Vol. 34, 2005, pp. 507–540.

[113] Spiker, M. A., *Development of an Efficient Design Method For Non-Synchronous Vibrations*, Ph.D. thesis, Duke University, 2008.

[114] Blackburn, H. and Henderson, R., "A Study of Two-Dimensional Flow Past an Oscillating Cylinder," *Journal of Fluid Mechanics*, Vol. 385, No. 1, 1999, pp. 255–286.

[115] Pedro, G., Suleman, A., and Djilali, N., "A Numerical Study of the Propulsive Efficiency of a Flapping Hydrofoil," *International Journal for Numerical Methods in Fluids*, Vol. 42, No. 5, 2003, pp. 493–526.

[116] Anderson, J. D., *Computational Fluid Dynamics, the Basics with Applications*, McGraw Hill, 1995.

[117] MacCormack, R. W., "The Effect of Viscosity in Hypervelocity Impact Cratering," AIAA paper 1969-354, 1969.

[118] Wu, H.-Y., Yang, S., Liu, F., and Tsai, H.-M., "Comparison of Three Geometric Representations of Airfoils for Aerodynamic Optimization," AIAA Paper 2003-4095, 2003.

[119] Jameson, A., "Aerodynamic Shape Optimization Using the Adjoint Method," *Lectures at the Von Karman Institute, Brussels*, 2003.

[120] Castonguay, P. and Nadarajah, S. K., "Effect of Shape Parameterization on Aerodynamic Shape Optimization," AIAA Paper 2007-0059, 2007.

[121] Yang, S., Wu, H.-Y., Liu, F., and Tsai, H.-M., "Aerodynamic Design of Cascades by Using an Adjoint Equation Method," AIAA Paper 2003-1068, 2003.

[122] Zhu, C., Byrd, R. H., Lu, P., and Nocedal, J., "Algorithm 778: L-BFGS-B: Fortran Subroutines for Large-Scale Bound-Constrained Optimization," *ACM Trans. Math. Softw.*, Vol. 23, No. 4, pp. 550–560.

Vita

Huang Huang was born in Tongcheng, China. He graduated June 2006 with a Bachelor of Science degree from the Aerospace Science and Engineering department of Beihang University. He obtained a master of science degree of fluid mechanics from Beihang University as well. In 2008, he began his PhD studies in the department of Mechanical, Aerospace and Biomedical Engineering of the University of Tennessee, Knoxville, where he was advised by Dr. Kivanc Ekici. His research interests include: unsteady turbomachinery aerodynamics, aeroelastics, adjoint method and optimization.